

## Chapter 8

## Radiation and Climate

### 8.1 Introduction

Climate is usually defined as the average state of the atmosphere observed as weather in terms of the mean and its statistical deviations that measure the variability over a period of time. Thus, we may speak of the climate of a season, a year, or longer periods. We frequently use the terms climatological temperature, precipitation, and other atmospheric parameters (e.g., data averaged over a 30-year period) to represent the mean atmospheric state. Changes in climate involve interactions of the atmosphere with other parts of the climate system, including the oceans, ice, snow, and land, associated with natural variability and/or anthropogenic perturbations.

Natural variability includes changes in the solar constant associated with sunspot activities (Section 2.3), changes in the solar insolation distribution caused by the earth's orbit around the sun (Section 2.2), and changes in atmospheric composition due to volcanic eruptions (Section 8.4.4). These are referred to as *external forcings*, which may also occur as a result of human activities, such as increases in greenhouse gases (Sections 4.1 and 8.4) and anthropogenic aerosols (Section 8.6.3).

An understanding of the earth's climate and climate change must begin with a comprehensive understanding of the radiation emitted from the sun and the absorption of solar energy by the atmosphere and the surface, as well as of the emission of thermal infrared energy from the earth-atmosphere system, as presented in Chapters 2, 3, and 4, respectively. In Chapters 5 and 6, we detailed the scattering and absorption processes involving molecules, aerosols, and cloud particles. The atmospheric and surface data required for global weather and climate studies must be primarily gathered from satellites by means of remote sensing, the principles of which were discussed in Chapter 7.

Radiation equilibrium at the top of the atmosphere represents the fundamental mode of the climate system. The incoming solar energy that is absorbed by the earth-atmosphere system must be balanced by an equal amount of emitted thermal infrared energy so as to achieve climate equilibrium. Otherwise, the equilibrium temperature of the earth planet, the brightness as viewed from space, would undergo a continuous change until the energy balance was restored. In Section 4.1, we showed that the equilibrium temperature of the earth-atmosphere system, based on the Stefan-Boltzmann law, is given by  $T_e = [S(1 - \bar{\tau})/4\sigma]^{1/4}$ , where  $S$  is the solar

constant, representing the energy available from the sun, and  $\bar{r}$  is the global albedo, representing the internal reflecting power of the earth–atmosphere system. For the present climate condition,  $T_e$  is about 255 K. As a result of the greenhouse effect of the earth’s atmosphere and its convective nature, the present surface temperature is about 288 K. Thus, the surface temperature is 33 K warmer than the equilibrium temperature.

Global radiation budgets have been observed from space since the beginning of the meteorological satellite era. In Section 8.2, we present a description of the manner in which the radiation budget is derived. The climate system is also affected by the internal heating and cooling of the atmosphere, as well as by the surface radiative budget, which are subsequently discussed.

The physical understanding of climate processes and the prediction of future climate and climate change require numerical models that encompass all relevant climate system components, including the atmosphere, the oceans, land, ice, and snow, as well as their interactions and feedbacks. It is essential that the numerical models for climate studies be based upon well-established physical principles since we do not have future data to check and verify these models, which must be built solely on our knowledge of the present historical climate conditions. In what follows, we first present the role of radiation in two simplified climate models. One-dimensional radiative–convective climate models have been widely employed in the past to explain vertical temperature perturbations due to external radiative forcings such as the increase in greenhouse gases and the indirect role of clouds. The foundation of these models and some significant perturbation studies are presented in Sections 8.3 and 8.4. In Section 8.5, we present one-dimensional energy-balance models, which include surface temperature variation in the latitude and which have been used primarily to evaluate the effect of solar constant and solar insolation variations on climate, particularly in regard to the question of the advance and retreat of polar ice in the geological time scale.

To quantify the response of the climate system to changes in external forcings and to perfect the prediction of future climate and climate change, we must rely on global climate models that account for all of the essential interactions and feedbacks among the climate system components. Models and their components are based on the physical laws represented by mathematical equations that govern atmospheric and oceanic dynamics and physics. In Section 8.6, we first provide some introductory notes concerning the general circulation model, particularly in reference to the transfer of radiation in the earth–atmosphere system. We then discuss cloud radiative forcing induced by the representation of cloud cover and cloud microphysics in typical global climate models within the context of greenhouse warming. Subsequently, we present examples of the direct climate radiative forcings induced by anthropogenic aerosols and contrails. Finally, we point out that radiation and cloud interactions and feedbacks are relevant and important processes in the numerical simulation of interannual and decadal time-scale variability, and present an example associated with the El Niño–Southern Oscillation simulated from a global climate model that couples the atmosphere and the oceans.

## 8.2 Radiation Budget of the Earth–Atmosphere System

### 8.2.1 Observational Considerations

The earth radiation budget (ERB) at the top of the atmosphere (TOA) has been derived from satellite observations since the beginning of the meteorological satellite era. The first-generation ERB instruments included black and white hemispheric sensors using thermistor detectors to measure the sensor temperature on board the first U.S. meteorological satellite, Explorer 6, launched February 17, 1959 (Suomi, 1958). This first generation also included a five-channel scanning radiometer on board the TIROS satellite series. Each of the channels had a narrow instantaneous field of view, and the measurements were radiances (per solid angle) rather than flux densities.

In the second generation of satellite missions during the 1960s and 1970s, polar, sun-synchronous orbits provided the opportunity for daily global coverage of the earth. In addition, the duration of spacecraft measurements was extended to several years. Flat, nonscanning radiometers were installed on several research and Environmental Science Service Administration operational satellites and, later, medium and wide field-of-view radiometers were also deployed on the NOAA satellites. Medium- and high-resolution infrared radiometers were used on Nimbus satellites for the detection of shortwave (solar) and longwave (IR) radiation. Nimbus 2 and 3 contained five-channel medium-resolution scanning radiometers and provided the first observations of the ERB for the entire globe. The aperture of the radiometers was about  $2.5^\circ$ , resulting in a spatial resolution of about 50 km near nadir and about 110 km at an angle of  $40^\circ$ . Spectral band passes for these radiometers were  $0.3\text{--}4\text{ }\mu\text{m}$  for shortwave and  $5\text{--}50\text{ }\mu\text{m}$  for longwave. The computation of outgoing flux densities from measured radiances required conversion of measured filtered radiances to radiances covering the entire solar and thermal IR spectra, integration over all angles of measurements using bidirectional models, and estimation of the average flux density over a 24-hour period. NOAA polar-orbiting satellites performed scanning measurements in the visible and IR window regions. The transformation of these narrow spectral interval data to broadband estimates of flux densities required several assumptions and models. The narrowband scanning radiometers had a spatial resolution of about 4 km at nadir. Valuable data sets have been constructed from the narrowband measurements of ERB components.

The third generation of satellite observational systems led to the development of ERB instruments that measured direct solar irradiance, reflected shortwave radiation, and emitted longwave radiation. The Nimbus 6 and 7 satellites contained wide field-of-view and scanning radiometers that provided valuable observations of the ERB. The scanning measurements observed the directional and bidirectional reflecting and emitting properties of the earth–atmosphere system over both time and space and were important in developing directional models for the conversion of radiances to flux densities. The longest record of solar constant measurements was made available by Nimbus 7 observations.

The sun-synchronous, polar-orbiting satellites observed each location at about the same local time. As a consequence, the observations were insufficient to provide a more detailed quantitative estimate of the temporal and spatial sampling errors. Studies of the ERB using data from the geostationary satellites were especially useful because they provided a regular sample of the atmospheric diurnal cycle. This enabled a wide range of spatial and temporal radiation variations to be investigated. Observations from GOES and METEOSAT satellites have been used in numerous studies of the ERB. Radiometers on board geostationary satellites were confined to narrow bands and had spatial resolutions that varied from about 0.5 to 10 km at nadir. The processing of observed data from geosynchronous altitudes required assumptions similar to those used to interpret the measurements from NOAA polar-orbiting satellites.

In order to provide comprehensive data sets for studying the diurnal and annual cycles of the ERB, as well as the role of clouds in the ERB, the fourth generation of satellite observation systems, referred to as the Earth Radiation Budget Experiment (ERBE), was launched in the 1980s. The experiment consisted of scanning and non-scanning radiometers on three satellites. The NASA Earth Radiation Budget Satellite (ERBS) performed a  $57^\circ$  inclination orbital precession around the earth once every 2 months. The other two satellites were NOAA 9 and NOAA 10 operational meteorological satellites.

#### 8.2.1.1 BLACK AND WHITE SENSORS BASED ON RADIATIVE EQUILIBRIUM

For historical reasons, we shall first discuss the use of a matched pair of spherical black and white sensors, the so-called Wisconsin sensors originally designed by Suomi (1958), which used thermistor detectors to measure the sensor temperature. In a short time after exposure to various radiative components involving the direct solar flux, shortwave flux reflected by the earth and atmosphere, and longwave flux emitted by the earth and atmosphere, each sensor achieves a radiative equilibrium. The absorptivity of the black sensor,  $A_b$ , was assumed to be the same for both shortwave and longwave radiation. However, the absorptivity of the white sensor for shortwave and longwave radiation was assumed to be different, denoted by  $A_w^s$  and  $A_w^l$ , respectively.

Let the temperatures measured by the black and white sensors be  $T_b$  and  $T_w$ , respectively. On the basis of the Stefan–Boltzmann and Kirchhoff laws (Section 1.2), radiative equilibrium equations for both sensors may be expressed by

$$4\pi a^2 A_b \sigma T_b^4 = \pi a^2 A_b (F_\odot + F'_s + F'_{ir}), \quad (8.2.1)$$

and

$$4\pi a^2 A_w^l \sigma T_w^4 = \pi a^2 [A_w^s (F_\odot + F'_s) + A_w^l F'_{ir}]. \quad (8.2.2)$$

These two equations show that the emitted energy per unit time is equal to the absorbed energy per unit time, where  $4\pi a^2$  and  $\pi a^2$  represent the emission and absorption areas, respectively, of the two spherical sensors, each with radius  $a$ . The flux densities of

the reflected shortwave and longwave radiation for spherical sensors are defined by

$$F'_s = \int_0^\Omega I_s d\Omega, \quad F'_{ir} = \int_0^\Omega I_{ir} d\Omega, \quad (8.2.3)$$

where  $\Omega$  is the solid angle by which the sensor sees the earth,  $I_s$  and  $I_{ir}$  are the radiant intensities reflected and emitted from the earth, respectively, and  $F_\odot$  denotes the direct solar irradiance.

Upon solving the sum of the shortwave flux densities and the longwave flux density, we obtain

$$F_\odot + F'_s = [4\sigma A_w^l / (A_w^l - A_w^s)] (T_b^4 - T_w^4), \quad (8.2.4)$$

and

$$F'_{ir} = [4\sigma / (A_w^l - A_w^s)] (A_w^l T_b^4 - A_w^s T_w^4). \quad (8.2.5)$$

The direct solar irradiance,  $F_\odot$ , can be evaluated from the solar constant, which is specified prior to the experiment.

In order to derive the reflected solar flux density and the emitted thermal infrared flux density in terms of the measured values expressed in Eq. (8.2.3), the following evaluation procedures are required. According to the definition of the flux density and the isotropic radiation assumption discussed in Section 1.1, the reflected solar flux density is given by

$$F_s = \int_0^{2\pi} \int_0^{\pi/2} I_s(\theta, \phi) \cos \theta \sin \theta d\theta d\phi = \pi I_s, \quad (8.2.6a)$$

where  $\theta$  and  $\phi$  are the zenith and azimuthal angles, respectively. Thus, the planetary albedo,  $r$ , can be expressed by

$$r = \pi I_s / (F_\odot \cos \theta_0), \quad (8.2.6b)$$

where the denominator represents the solar flux density available at TOA normal to the plane-parallel stratification. On the basis of Eqs. (8.2.3) and (8.2.6b), we have

$$F'_s = \frac{F_\odot}{\pi} \int_0^\Omega r \cos \theta_0 d\Omega. \quad (8.2.7)$$

Assuming  $\cos \theta_0$  does not vary significantly over the viewing area of the satellite, it can be removed from the integral. Moreover, we define the average planetary albedo of the viewing area as follows:

$$\bar{r} = \frac{1}{\Omega} \int_0^\Omega r d\Omega. \quad (8.2.8)$$

It follows that

$$\bar{r} = \pi F'_s / (F_\odot \cos \theta_0 \Omega). \quad (8.2.9)$$

In a similar manner, under the assumption of isotropic radiation, the emitted thermal infrared flux density is given by

$$F_{ir} = \pi I_{ir} = \sigma T_e^4, \quad (8.2.10)$$

where  $T_e$  denotes the equivalent blackbody temperature of the earth–atmosphere system. Upon defining the average equivalent blackbody temperature of the viewing area in the form

$$\overline{T_e^4} = \frac{1}{\Omega} \int_0^\Omega T_e^4 d\Omega, \quad (8.2.11)$$

we obtain

$$\overline{T_e^4} = \pi F'_{ir} / (\sigma \Omega). \quad (8.2.12)$$

The solid angle through which the sensor sees the earth is given by (see Exercise 1.2)

$$\Omega = 2\pi \left[ 1 - \frac{(2a_e h + h^2)^{1/2}}{a_e + h} \right]. \quad (8.2.13)$$

Hence, the average planetary albedo  $\bar{r}$  and equivalent blackbody temperature  $T_e$  can be evaluated from the black and white sensors through  $F'_s$  and  $F'_{ir}$ . The average reflected solar flux density and emitted thermal infrared flux density, respectively, as functions of location and time may now be expressed by

$$\bar{F}_s = \bar{r} F_\odot \cos \theta_0 \quad (8.2.14)$$

and

$$\bar{F}_{ir} = \sigma \overline{T_e^4}. \quad (8.2.15)$$

In the following, we discuss the averaging process with respect to time and space.

### 8.2.1.2 SCANNING RADIOMETER AND ANGULAR MODELS

As discussed previously, the radiometric measurements determined from satellite platforms are radiances. The conversion of radiances (per solid angle) to flux densities is a major undertaking in satellite radiation budget analyses.

The daily average reflected flux density of solar radiation is defined by

$$\begin{aligned} F_s(\varphi, \lambda) &= \int_{\text{day}} F_s[\varphi, \lambda; \theta_0(t)] dt / \Delta t \\ &= \int_{\text{day}} dt \int_0^{2\pi} \int_0^{\pi/2} I_s[\varphi, \lambda; \theta, \phi; \theta_0(t)] \cos \theta \sin \theta d\theta d\phi / \Delta t, \end{aligned} \quad (8.2.16)$$

where  $\varphi$  and  $\lambda$  denote the latitude and longitude, respectively, and  $\Delta t$  is the time interval. For a given location  $(\varphi, \lambda)$ , the broadband scanning radiometer measures the scattered radiance or intensity (energy/area/time/solid angle), which depends on the zenithal and azimuthal angles of the outgoing radiation as well as the position of the sun in terms of the solar zenith angle  $\theta_0$ .

Since the scanning radiometer detects the reflected solar radiance only at a given scan angle, certain empirical adjustments are required in order to evaluate the daily reflected flux. The empirical anisotropic scattering function is defined as

$$X(\theta, \phi; \theta_0) = F_s(\theta_0)/[\pi I_s(\theta, \phi; \theta_0)]. \quad (8.2.17)$$

Prior to satellite experiments, the  $X$  function may be determined based on the radiative transfer theory as well as on aircraft and balloon observations for selected localities. With the assumption that values are independent of the locality, the daily average reflected solar flux can be evaluated by

$$F_s(\varphi, \lambda) = \int_{\text{day}} X[\theta, \phi; \theta_0(t)] \pi I_s[\varphi, \lambda; \theta, \phi; \theta_0(t)] dt / \Delta t. \quad (8.2.18)$$

It follows that the daily planetary albedo can now be defined by

$$r(\varphi, \lambda) = F_s(\varphi, \lambda) / Q(\varphi), \quad (8.2.19)$$

where the daily average solar insolation discussed in Section 2.2.3 is given by

$$Q(\varphi) = \int_{\text{day}} F_{\odot} \cos \theta_0(t) dt / \Delta t. \quad (8.2.20)$$

Similarly, an empirical function for the emitted infrared radiation may be defined. Because the outgoing infrared radiation is independent of both the azimuthal angle and the sun's position, the empirical function may be written in the form

$$X(\theta) = F_{ir} / [\pi I_{ir}(\theta)]. \quad (8.2.21)$$

Again, this function is to be obtained prior to satellite experiments. Thus, the daily average thermal infrared flux density can be evaluated by

$$\begin{aligned} F_{ir}(\varphi, \lambda) &= \int_{\text{day}} F_{ir}(\varphi, \lambda; t) dt / \Delta t \\ &= 2\pi \int_{\text{day}} dt \int_0^{\pi/2} I_{ir}(\varphi, \lambda; \theta; t) \cos \theta \sin \theta d\theta / \Delta t \\ &= \int_{\text{day}} X(\theta) \pi I_{ir}(\varphi, \lambda; \theta; t) dt / \Delta t. \end{aligned} \quad (8.2.22)$$

Note that radiances measured by the scanning radiometer normally are corrected to the nadir angle ( $\theta = 0^\circ$ ).

We may now define the radiation balance equation using Eqs. (8.2.19), (8.2.20), and (8.2.22). For a given locality with latitude  $\varphi$  and longitude  $\lambda$ , the net daily flux density may be expressed by

$$R(\varphi, \lambda) = Q(\varphi)[1 - r(\varphi, \lambda)] - F_{ir}(\varphi, \lambda). \quad (8.2.23)$$

To derive the zonally averaged quantities, we perform the integration over the longitudinal direction to give

$$R(\varphi) = Q(\varphi)[1 - r(\varphi)] - F_{ir}(\varphi), \quad (8.2.24)$$

where the operator

$$R(\varphi) = \int_{\lambda} R(\varphi, \lambda) d\lambda / \Delta\lambda.$$

Moreover, the global value may be evaluated by carrying out the integration over the latitudinal direction as follows:

$$\bar{R} = \bar{Q}(1 - \bar{r}) - \bar{F}_{ir}, \quad (8.2.25)$$

where the operator

$$\bar{X} = \int_{\varphi} \int_{\lambda} X d\lambda d\varphi / (\Delta\lambda \Delta\varphi),$$

and  $X$  can be  $R$ ,  $Q$ , or  $F_{ir}$ . Finally, time averaging can also be carried out to obtain the monthly and annual radiation budget values.

### 8.2.2 Radiation Budget Viewed from Space

The ERB is usually presented in terms of the emitted longwave (or IR) flux,  $F_{ir}$ , referred to as outgoing longwave radiation (OLR); the planetary albedo (or, simply, albedo),  $r$ , defined as the ratio of the reflected solar flux to the incident flux at TOA; and the net radiative flux, defined by

$$F = (1 - r)Q - F_{ir}, \quad (8.2.26)$$

where we have used flux instead of flux density and replaced the notation  $R$  by  $F$ . The first term on the right-hand side of Eq. (8.2.26) represents the absorbed solar flux within the earth–atmosphere system. The globally and annually averaged albedo and OLR have been derived by a number of researchers from various data sources. In the following, we present a number of radiation budget results derived from satellite broadband radiation measurements.

Global distributions of OLR, albedo, and net flux averaged for the mean annual and seasonal conditions have been presented in numerous publications. Shown in Fig. 8.1 are maps of the mean annual condition. The albedos reveal a distinct land–ocean contrast equatorward of 30°N and 30°S, as well as high convective clouds, in particular Asian monsoons, where high albedo and low emission are evident. Poleward of 30°N and 30°S, the radiation budgets are relatively uniform zonally, especially in the Southern Hemisphere. At low latitudes, regions of relative energy gains and losses are evident for a given zone. Distinct variations are shown in the net fluxes in the tropical and subtropical zones where the deserts of Africa and Arabia appear as negative or small positive anomalies. The convective regions near Asia show large positive anomalies. In general, the albedos are negatively correlated with OLR, principally because of the presence of clouds. The exception is over desert regions, where cloud cover is at a minimum and the surface is relatively bright and warm. A net radiative gain is evident throughout almost the entire zone between ~40°N and ~40°S and is flanked by radiation sinks that generally deepen toward the poles. The radiation budgets of the earth and the atmosphere are largely regulated by clouds and temperature fields.



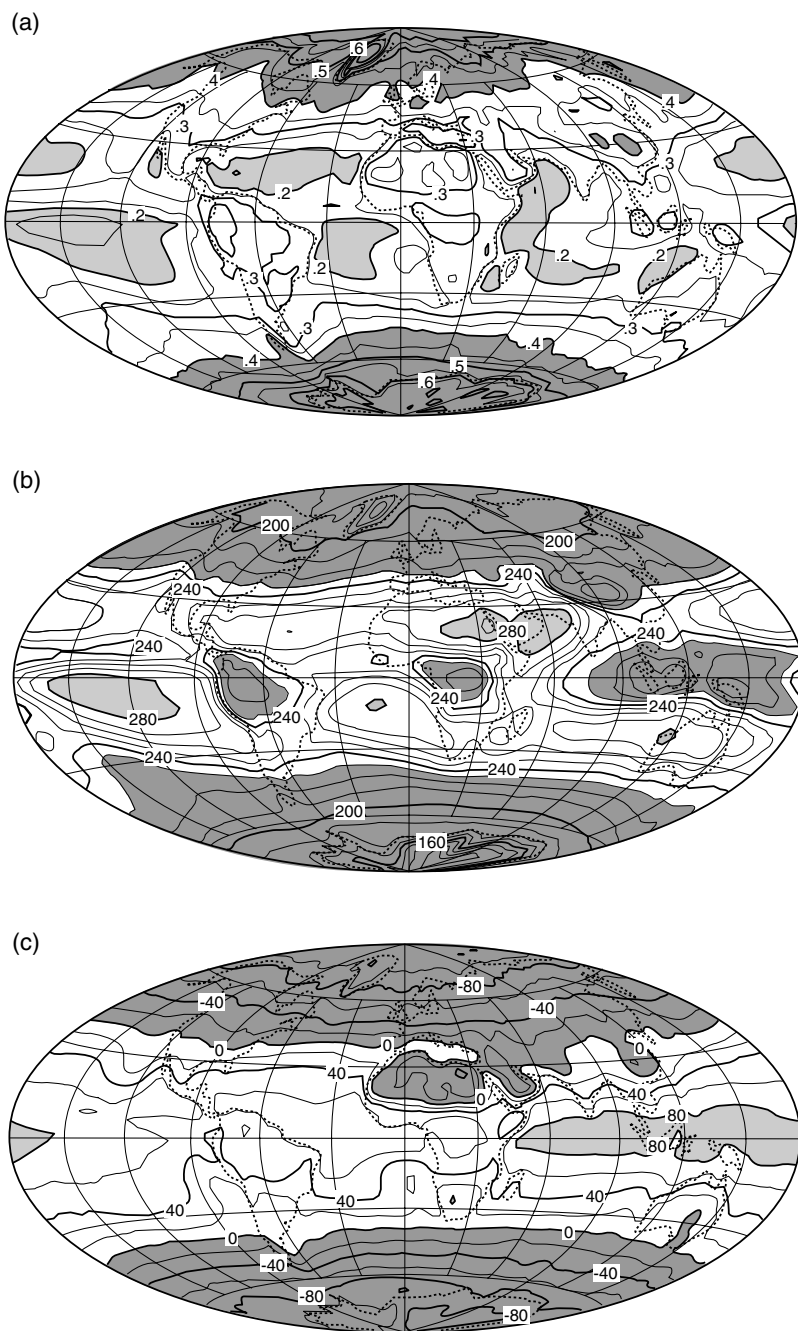


**Figure 8.1** Global maps of (a) mean annual planetary albedo, (b) outgoing longwave radiation ( $\text{W m}^{-2}$ ), and (c) net radiative flux ( $\text{W m}^{-2}$ ), in a Hammer equal-area projection (data taken from Hartmann, 1994). In these diagrams, heavier shaded areas denote albedos larger than 0.4, longwave fluxes smaller than  $230 \text{ W m}^{-2}$ , and negative net radiative fluxes.

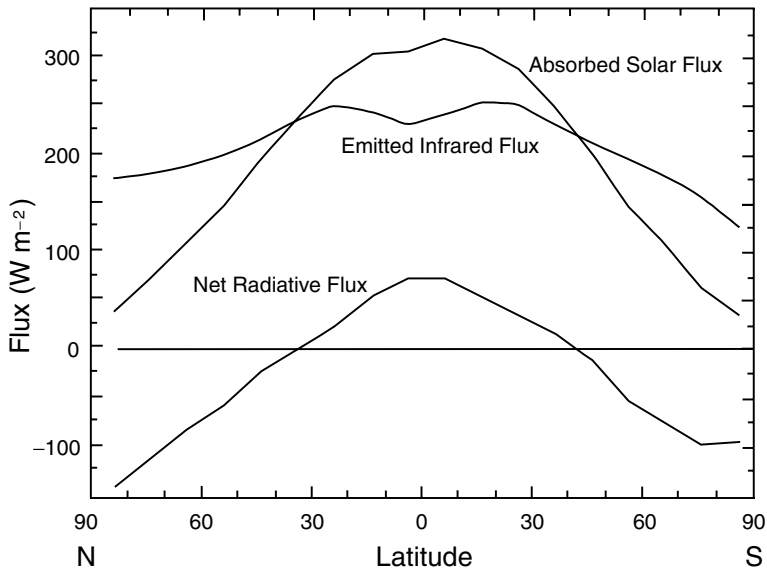


**Figure 8.2** Zonally averaged components of the annual mean absorbed solar flux, emitted thermal infrared flux (or OLR), and net radiative flux at the top of the atmosphere, derived from satellite broadband radiation measurements. These patterns were originally presented by Vonder Haar and Suomi (1971), Stephens *et al.* (1981), and more recently by Hartmann (1994).

In Fig. 8.2 we present the latitudinal distribution of annual solar, thermal infrared, and net radiative fluxes at TOA. The annual net radiative flux pattern is approximately symmetric between the Northern and Southern Hemispheres, with a maximum occurring at the equator. This maximum is a result of a minimum of OLR due to the towering cumulus clouds associated with the intertropical convergence zone and the large amount of solar flux absorbed in the equatorial regions, as shown in the figure. In the polar regions, large negative net fluxes are due to the high albedo of snow and ice. The net radiative flux pattern is also associated in part with the variation of the mean solar zenith angle with latitude. The results clearly show that there are gains of radiative energy in the tropics and subtropical regions but losses in the polar regions, a pattern that is essential to the production of general circulation in the atmosphere.

### 8.2.3 Cloud Radiative Forcing Derived from ERB Data

Clouds regularly occupy at least 50% of the sky on a global scale and are the most important regulators of the ERB. The presence of clouds greatly increases the percentage of solar flux that is reflected back to space. This effect, known as the *solar albedo effect*, reduces the solar flux available to the earth–atmosphere system and results in a cooling of the system. On the other hand, clouds reduce the thermal radiation emitted to space by absorbing the IR flux from the earth’s surface and the atmosphere below the cloud layer, and by emitting thermal radiation at normally colder cloud-top

temperatures. This effect, known as the *IR greenhouse effect*, increases the radiation budget, which, in general, results in a warming of the earth–atmosphere system. Thus, the net radiation available to the earth–atmosphere system, as well as the differential heating of the system, is strongly regulated by clouds in terms of their horizontal extent, vertical position, thermodynamic phase, liquid/ice content, and particle size distribution.

Many attempts have been made to diagnose cloud effects from the ERB data inferred from satellites. In reference to Eq. (8.2.26) and considering the specific effect of cloud cover  $\eta$ , partial differentiation leads to

$$\frac{\partial F}{\partial \eta} = -Q \frac{\partial r}{\partial \eta} - \frac{\partial F_{ir}}{\partial \eta} = \frac{\partial F_s}{\partial \eta} - \frac{\partial F_{ir}}{\partial \eta}. \quad (8.2.27a)$$

Or, we may write

$$\frac{\partial F}{\partial \eta} = \frac{\partial F}{\partial F_{ir}} \frac{\partial F_{ir}}{\partial \eta} = -\frac{\partial F_{ir}}{\partial \eta} \left( Q \frac{\partial r}{\partial F_{ir}} + 1 \right). \quad (8.2.27b)$$

The first and second terms on the right-hand side of these equations represent the effect of cloud cover on absorbed solar and emitted IR fluxes. To estimate these terms the method of regression on the observed data at a given grid point may be used. Since albedo increases with increasing cloud cover,  $\partial r / \partial \eta$  is always positive. In contrast, IR flux decreases with increasing cloud cover so that  $\partial F_{ir} / \partial \eta$  is negative. It follows that if  $\partial F / \partial \eta$  is positive, the IR greenhouse effect is greater than the solar albedo effect, whereas the reverse is true if  $\partial F / \partial \eta$  is negative.

Extracting the effects of clouds from ERB data requires identifying the ERB in clear-sky conditions. Consider a region that is partially covered by clouds. This region consists of an overcast region (cloudy) with a fractional area of coverage of  $\eta$  and a clear-sky region with a fractional area of coverage of  $1 - \eta$ . Let  $F$  be the observed OLR, absorbed solar flux, or net flux over the region. Then, we may write

$$F = (1 - \eta)F^{\text{cl}} + \eta F^{\text{ov}}, \quad (8.2.28a)$$

where  $F^{\text{cl}}$  and  $F^{\text{ov}}$  are the clear-sky and cloud fluxes, respectively. The effects of clouds on  $F$  may be evaluated from

$$C = F^{\text{cl}} - F = \eta(F^{\text{cl}} - F^{\text{ov}}). \quad (8.2.28b)$$

The term  $C$  is referred to as *cloud radiative forcing*. A separation of solar and IR effects from Eq. (8.2.28a) leads to

$$C_{ir} = F_{ir}^{\text{cl}} - F_{ir}, \quad (8.2.29a)$$

$$C_s = Q(r^{\text{cl}} - r), \quad (8.2.29b)$$

where  $F_{ir}^{\text{cl}}$  and  $r^{\text{cl}}$  are clear-sky OLR and albedo, respectively.

Clouds are almost always more reflective than the oceans and land, except in ice and snow conditions. Thus, when clouds are present, more solar flux is reflected back to space than with clear sky. Cloud solar forcing,  $C_s$ , which is the difference between

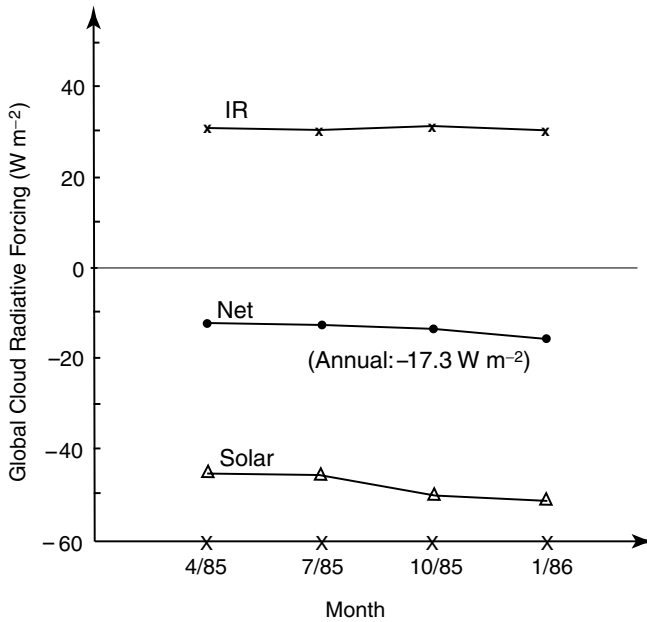


**Figure 8.3** Global cloud radiative forcing in units of  $\text{W m}^{-2}$  as a function of months estimated from Earth Radiation Budget Experiment (ERBE) data (data taken from Harrison *et al.*, 1990).

the clear-sky and cloudy-sky reflected solar fluxes, gives a quantitative estimate of cloud effects on solar radiation. On the other hand, less thermal IR flux is emitted to space from a cloudy region than from clear sky. Cloud IR forcing,  $C_{ir}$ , which is the difference between the clear-sky and cloudy-sky emitted IR fluxes, is a measure of cloud effects on thermal IR radiation.

Estimates of the global distribution of cloud radiative forcing have been obtained from ERBE, which includes three satellites in different orbits: ERBS, NOAA 9, and NOAA 10. Figure 8.3 shows seasonal global cloud radiative forcing values based on data gathered from the scanning radiometers on board ERBS and NOAA 9. The global annual  $C_s$  and  $C_{ir}$  are  $-48$  and  $31 \text{ W m}^{-2}$ , respectively, resulting in net cloud radiative forcing of  $-17 \text{ W m}^{-2}$ . April has the smallest net cloud radiative forcing value, whereas January has the largest. Although the variation of this forcing between hemispheres not shown in this figure is significant during winter and summer months, the seasonal effect of cloud radiative forcing is generally small. On a global scale for all seasons, the albedo effect from clouds is more dominant than the greenhouse effect.

Cloud radiative forcing has significant regional characteristics. For a given region, cancellation of cloud solar and IR forcing, derived from ERB components at TOA, does not imply a negligible role of clouds in the regional climate. The vertical gradients of radiative heating and cooling produced by clouds presented in the next section, which are critical in weather and climate processes, are not accounted for in the preceding discussion of cloud radiative forcing.

### 8.2.4 Radiative Heating/Cooling Rates of the Atmosphere

Vertical profiles of the radiative heating and cooling rates of the atmosphere can, in principle, be determined from space based on spectral radiometric observations, as demonstrated in Section 7.4.6, a subject requiring considerable research and development. At this point, however, climatological radiative heating rates in the atmosphere must be computed from a radiative transfer program based on information about the composition and structure of the earth's atmosphere (Section 3.1). The solar input and surface albedo field are also needed in computing solar heating rates in the atmosphere.

In Sections 3.2 and 4.2, we discussed the absorption of solar and thermal infrared radiation in detail. Absorption of sunlight is chiefly produced by  $\text{H}_2\text{O}$ , covering the entire near-IR region, and  $\text{O}_3$ , covering the UV and visible regions. Absorption contributions also come from  $\text{O}_2$  and other minor gases, including  $\text{CH}_4$ ,  $\text{NO}_2$ ,  $\text{N}_2\text{O}$ ,  $\text{O}_2 \cdot \text{O}_2$ ,  $\text{O}_2 \cdot \text{N}_2$ , and  $\text{CO}_2$ . In the thermal infrared region, absorption by  $\text{H}_2\text{O}$  essentially covers the entire spectrum.  $\text{CO}_2$  and  $\text{O}_3$  exhibit significant absorption in the  $15\ \mu\text{m}$  and  $9.6\ \mu\text{m}$  regions.  $\text{H}_2\text{O}$ ,  $\text{CO}_2$ , and  $\text{O}_3$  are radiatively active gases of primary importance to the earth's atmosphere.  $\text{CH}_4$  and  $\text{N}_2\text{O}$  also show strong absorption bands in the  $7\text{--}8\ \mu\text{m}$  region.

Aerosols both absorb and scatter sunlight. The significance of absorption relative to scattering is determined by the particular aerosol's chemical composition and particle size distribution. Aerosols are usually considered to be important for their influence on solar radiation. Water droplets and ice crystals are relatively transparent in visible light, but absorb near-infrared radiation in the solar spectrum. Clouds have a profound influence on both solar and terrestrial radiation because of their large global coverage. Moreover, there are numerous types of surfaces, which vary significantly in their reflecting properties with respect to incoming solar flux.

In the first edition of this text, comprehensive radiative budget studies reported by Freeman and Liou (1979) were presented. In that study, the discrete-ordinates method for radiative transfer was used in conjunction with the exponential fitting of the band transmittance in carrying out spectral radiative budget calculations. It was pointed out that the radiative transfer method used for global calculations must be an efficient but accurate one in which the spectral dependence of radiation must be covered; the absorption, scattering, and emission of molecules and particulates should be treated adequately; and at the same time, the inhomogeneity of the atmosphere should be properly taken into account. Many simplified radiative transfer methodologies have been developed since the publication of the first edition. In particular, the innovation of the delta four-stream and delta two/four-stream approximations for radiative transfer in inhomogeneous atmospheres (Sections 6.5.3, 6.5.4, and 4.6.3) offers efficient and accurate calculations of atmospheric flux distributions. The development of the correlated  $k$ -distribution method (Section 4.3.2) for sorting absorption lines in inhomogeneous atmospheres allows the effective incorporation of gaseous absorption in multiple scattering calculations. Moreover, novel theories for the calculation of scattering and absorption properties of nonspherical ice crystals have been developed specifically for application to radiative transfer in cirrus clouds.

In what follows, we present meridional cross sections of atmospheric solar, IR, and net radiative heating rates based on the radiative transfer model developed by Fu and Liou (1993), which has been significantly improved by the NASA/Langley group working on the retrieval of radiative fluxes using satellite data (Charlock and Alberta, 1996). In brief, the model employs the delta-four-stream method for radiative transfer in inhomogeneous atmospheres containing Rayleigh molecules, absorbing gases, aerosols, and cloud particles. The solar and IR spectra are divided into a number of intervals according to the location of absorption bands based on which the incorporation of nongray gaseous absorption in multiple scattering atmospheres is accomplished by following the correlated  $k$ -distribution method. The single-scattering properties of spherical aerosols and water droplets and nonspherical ice crystals are determined from the light-scattering theories presented in various sections in Chapter 5.

The bulk of the input data required for global radiation computations are the atmospheric profiles, the geometric and physical properties of clouds, the global fractional cloudiness for each cloud type, the earth's surface albedo, the duration of sunlight, and the zenith angle of the sun. The atmospheric profile includes the vertical profiles of pressure, molecular and aerosol densities, water vapor, ozone, and other trace gases. The atmospheric profiles used in the present radiative budget calculations are based on mean annual atmospheric conditions involving water vapor, ozone, pressure, and temperature profiles.

Clouds are divided into high, middle, and low cloud types. The fractional cloud cover for each cloud type as a function of the latitude follows those provided by the ISCCP project (Section 7.4.5). The atmospheric aerosol model used is a light background concentration providing about 25 km surface visibility (d'Almeida *et al.*, 1991). For scattering calculations, all cloud (except cirrus) and aerosol particles are assumed to be spherical. The high cirrus are considered to be composed exclusively of nonspherical ice crystals randomly oriented in space. The radiative transfer program for clouds is driven by liquid/ice water path and mean effective particle radius/size, which are prescribed for each cloud type based on available observations (Liou, 1992). Within the IR spectrum, all clouds except cirrus are considered to be blackbodies.

The surface albedo of the earth is also an important parameter that determines the amount of the transmitted solar flux reaching the surface and reflecting back into the atmosphere to be absorbed or scattered, or to escape back into space as a component of the earth's global albedo. Values of the zonally averaged surface albedo are taken from data presented in Henderson-Sellers and Wilson (1983). The duration of sunlight and the solar zenith angle are important parameters in determining the radiation balance of the earth–atmosphere system. The solar zenith angle can be computed from the angles associated with the latitude, the declination of the sun, and the hour angle of the sun, as discussed in Section 2.3.1. The annual meridional cross sections of reflected solar and emitted IR fluxes at TOA were first compared to and matched those observed from satellites, as displayed in Fig. 8.2.

The differential solar heating of equatorial and polar regions provides the ultimate energy source for the general circulation of the atmosphere and the oceans and is also responsible for causing the climatic extremes between tropical and polar latitudes.

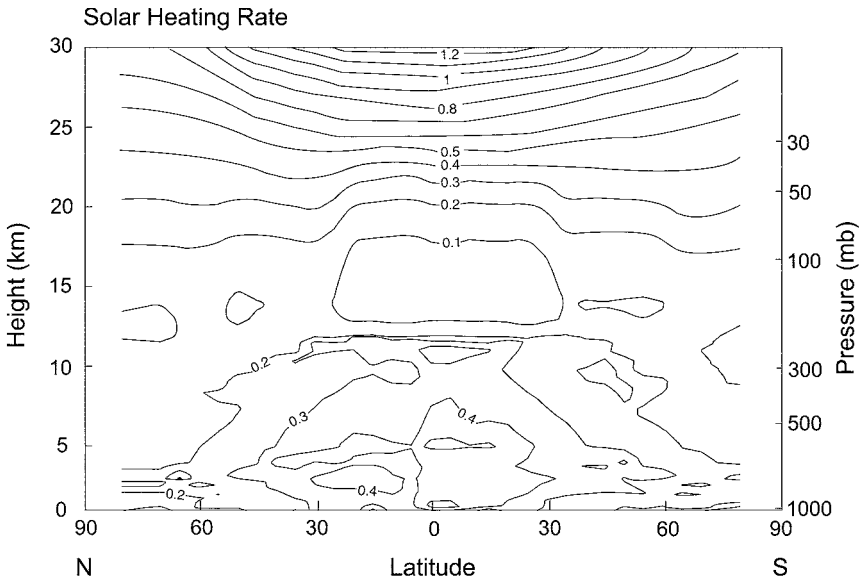


**Figure 8.4** Annual meridional cross sections of the solar heating rate ( $\text{K day}^{-1}$ ) of the atmosphere computed from a radiative transfer program using climatological temperature, cloud, gaseous, and surface albedo data. The input solar flux is  $342 \text{ W m}^{-2}$ . The contour line is  $0.1 \text{ K day}^{-1}$ .

Every portion of the earth in sunlit sky receives energy from the sun and is warmed to a greater or lesser degree. The primary factors that determine the degree of solar warming received by a particular region on average are the cloud cover, the water vapor and ozone contents of the atmosphere, the surface albedo, and the presence of aerosols in greater or lesser concentrations, as well as the latitude, which is related to the range of solar zenith angles experienced by the area.

The annual meridional cross sections of the solar heating rate are illustrated in Fig. 8.4. Maximum solar heating of about  $0.5 \text{ K day}^{-1}$  is observed at an altitude of about 4 to 5 km in the tropical and subtropical regions, using the solar flux of  $342 \text{ W m}^{-2}$  as input (solar constant of  $1366 \text{ W m}^{-2}$ ). Broad, flat minima occur in the upper troposphere and lower stratosphere, followed by increasing solar heating in the stratosphere due exclusively to the presence of ozone. Atmospheric solar heating is primarily produced by the absorption of water vapor in the troposphere and of ozone in the stratosphere.

While the radiation from the sun warms the earth's atmosphere everywhere, the role of terrestrial IR radiation is more complex. In the main, thermal IR radiation serves to cool the atmosphere, radiating away to space an amount of energy equivalent to the solar input, maintaining the radiative balance. Under certain conditions, however, thermal IR radiation adds to the warming of the atmosphere at particular levels and locations.

The annual meridional cross sections of thermal infrared cooling rates are shown in Fig. 8.5. The maximum cooling takes place in the stratosphere, due exclusively

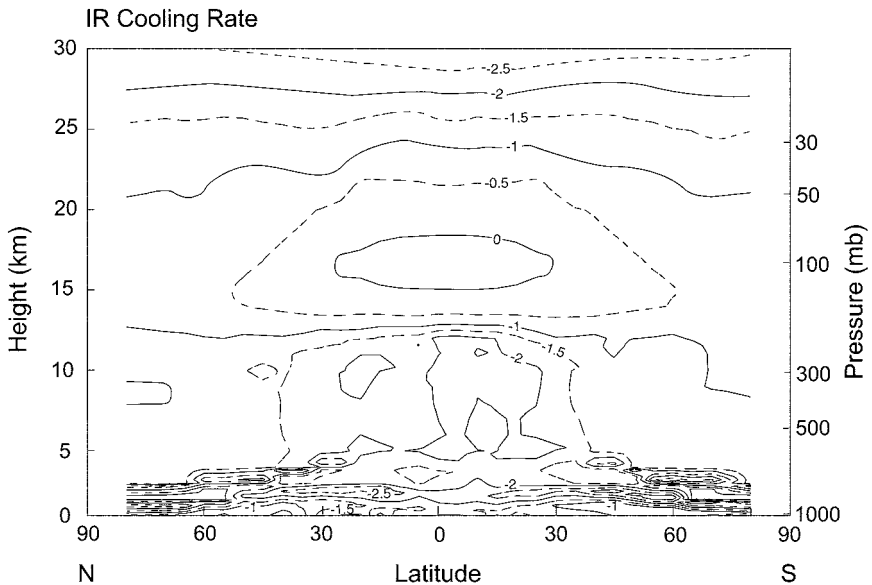


**Figure 8.5** Annual meridional cross sections of the thermal infrared (IR) cooling rate ( $\text{K day}^{-1}$ ) of the atmosphere computed from a radiative transfer program using climatological temperature, cloud, and gaseous data. The contour line is  $0.5 \text{ K day}^{-1}$ .

to carbon dioxide and ozone. Indeed, almost all cooling above the tropopause is produced by these two gases since above about 10 km the water vapor concentration decreases drastically to a negligible amount with respect to radiative transfer. Ozone is also responsible for the region of thermal heating found above the tropopause in tropical and subtropical latitudes. This heating is associated with the increase in ozone concentration with height to about 23 km, resulting in a convergence of flux into the region, where the heating is augmented by a similar region of heating due to carbon dioxide at the tropical tropopause, as well as by the higher temperatures found both above and below the tropopause. The effect of water vapor is to cool the clear atmosphere everywhere since there is an increase of flux with height as the water vapor concentration decreases. A secondary maximum of cooling occurs in tropical latitudes within the troposphere, associated with the large vertical gradients of water vapor and temperature. The effects of clouds, which tend to increase the cooling above their tops and decrease the cooling below their bases, also are evident in this region. Near the surface, large water vapor density and temperature gradients lead to another maximum of cooling in the tropics. This cooling is offset somewhat by the increase in warming below the cloud bases.

The net radiation budget was computed by summing the heating and cooling rates at each latitude and atmospheric layer. The net heating cross sections are presented in Fig. 8.6. Radiative cooling dominates solar heating almost everywhere. In the upper stratosphere, above 25 km, intense cooling due to ozone and carbon dioxide completely overshadows the solar heating by ozone. The high degree of cooling is



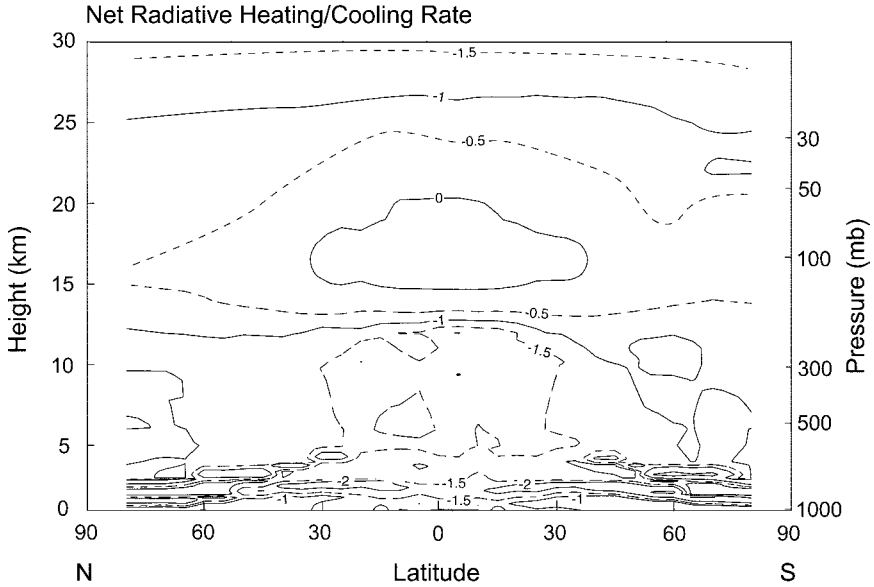


**Figure 8.6** Annual meridional cross sections of the net radiative heating/cooling rate ( $\text{K day}^{-1}$ ) of the atmosphere. The contour line is  $0.5 \text{ K day}^{-1}$ .

due, in part, to the effect of colder cloud tops. At the tropical tropopause, near 18 km, there is a small longwave heating that occurs in the region of minimum solar heating to produce a net heating. Below this region of heating is a region of maximum cooling associated with large vertical gradients of water vapor and temperature. Cooling produced by longwave radiation outweighs solar heating at every latitude, due primarily to water vapor, and thus has a maximum in the tropics. The presence of clouds tends to moderate the cooling in the lower atmosphere by reducing the cooling below their bases and by producing strong solar heating at their tops. The ubiquitous net radiative cooling in the earth's atmosphere is compensated for by other forms of energy in the atmosphere and by the transport of heat from the surface, as discussed in Section 8.5.1.

### 8.2.5 Radiation Budget at the Surface

Based on radiative equilibrium, the net radiative flux at the surface can be expressed by

$$F(0) = F_s^\downarrow(0)(1 - r_s) - [\varepsilon_s \sigma T_s^4 - \varepsilon_s F_{ir}^\downarrow(0)], \quad (8.2.30)$$

where  $F_s^\downarrow(0)$  denotes the solar flux reaching the surface,  $r_s$  is the surface albedo,  $\varepsilon_s$  is the surface emissivity, which in thermodynamic equilibrium is equal to absorptivity,  $T_s$  is the surface temperature, and  $F_{ir}^\downarrow(0)$  denotes the downward thermal infrared flux emitted from the atmosphere to the surface. The first and second terms on the

right-hand side of Eq. (8.2.30) represent the net solar (shortwave) and infrared (longwave) fluxes at the surface, respectively. These fluxes cannot be determined directly from satellites.

The study of the surface radiation budget (SRB) is an important subject related to climate modeling and parameterization. It is an integral part of the energy budget at the surface, which will be discussed further in Section 8.5.1. Reliable SRB values in various temporal and spatial scales are required to evaluate the sensible and latent heat fluxes from the surface to the atmosphere, a critical part of the global hydrological and energy cycles. The SRB distribution over the globe is usually determined from a radiative transfer program using appropriate input cloud data that has been derived from satellites as well as other relevant profile data, including water vapor, ozone, aerosols, etc. Thus, the accuracy of SRB fields is dependent on the input data, particularly that regarding clouds, and on the radiation code employed in the calculations. The importance of the SRB in climate studies has been noted by Pinker *et al.* (1995).

As an example, we present in the following a mean annual net radiative flux distribution at the earth's surface (Fig. 8.7) estimated by Budyko (1986) based on some direct surface observations over land and the ocean. The radiation flux decreases with latitude from values of 160–180 W m<sup>-2</sup> near the equator to values of about 20–40 W m<sup>-2</sup> poleward of 60° latitude. Most of the globe shows that the net surface radiation is downward. That is, the surface gains radiative energy because of the domination of the net downward solar flux. However, over the polar regions in winter, a net radiation loss can exist at the surface when the solar flux tends to be very small or zero. In general, the net radiative fluxes are higher over the oceans than over the continents at the same latitude. The highest values shown are on the order of 180 W m<sup>-2</sup> and occur in the tropical regions over the oceans in agreement with the distribution of the total solar radiation absorbed by the atmosphere and the oceans. Secondary equatorial maxima are found over the continents. The lowest values in the tropics occur over the deserts, because of high values of the surface albedo, low values of cloudiness and humidity, and high surface temperatures.

## 8.3 Radiative and Convective Atmospheres

### 8.3.1 Radiative Equilibrium

#### 8.3.1.1 A GLOBAL MODEL

The simplest climate model for the earth–atmosphere system is to consider the earth and the atmosphere as a whole and to evaluate the global radiative equilibrium temperature from the balance of incoming solar and outgoing thermal infrared fluxes. Let the global albedo be  $\bar{r}$ , the solar constant be  $S$ , and the radius of the earth be  $a_e$ . Over a climatological time period, there should be a balance between the energy absorbed and the energy emitted so that a radiative equilibrium temperature is maintained. Thus we should have

$$\pi a_e^2(1 - \bar{r})S = 4\pi a_e^2\sigma T_e^4, \quad (8.3.1)$$

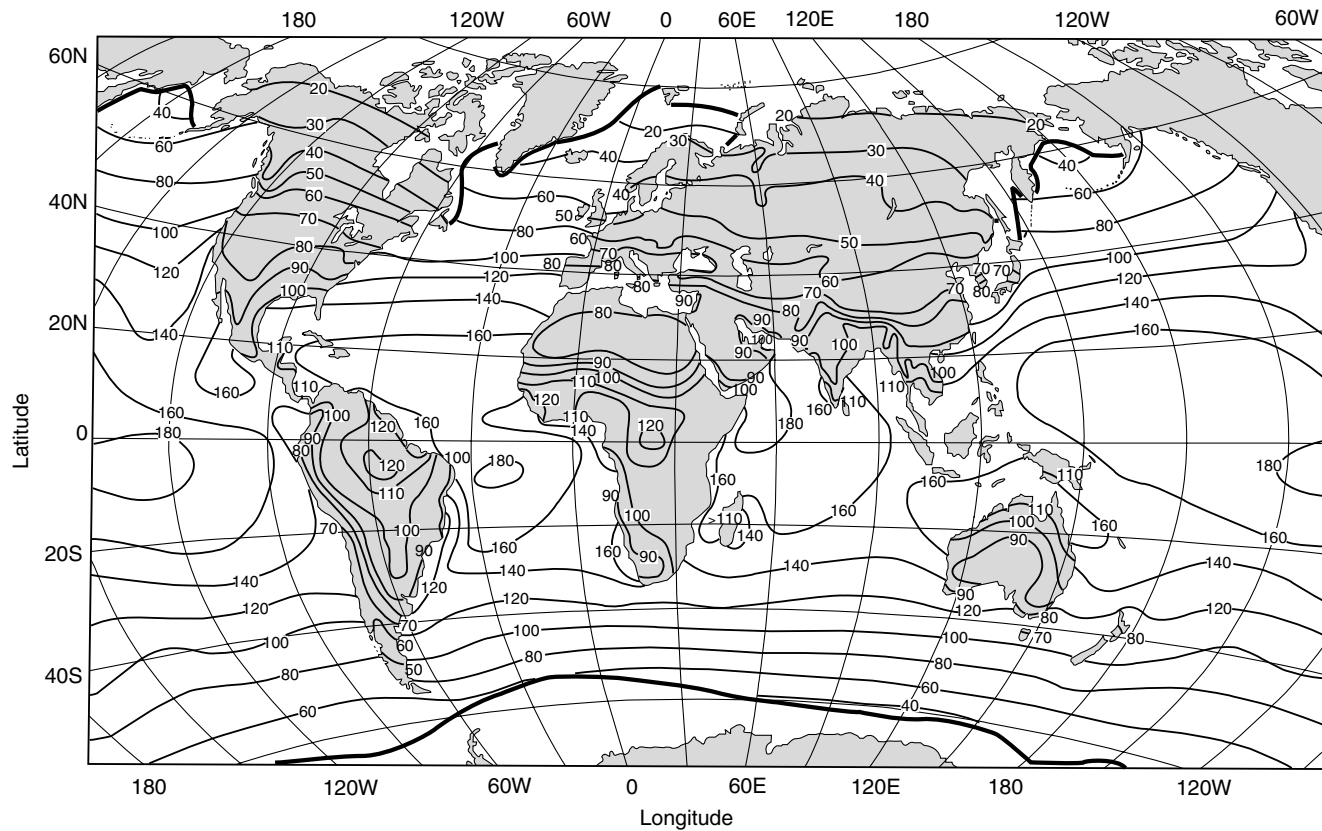


**Figure 8.7** Global distribution of the mean radiation flux ( $\text{W m}^{-2}$ ) at the earth's surface based on a number of direct surface observations over land and the ocean. The mean annual ice boundary is also shown by heavy lines (data taken from Budyko, 1986).

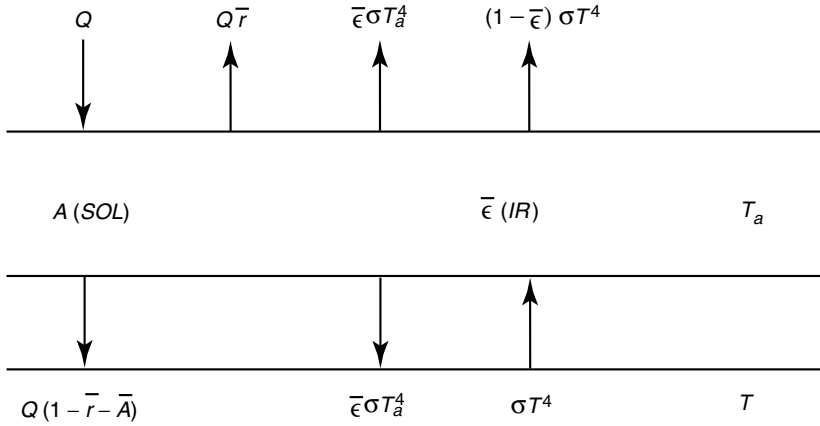


**Figure 8.8** A two-layer radiative equilibrium model involving the surface and the atmosphere with temperatures denoted by  $T$  and  $T_a$ , respectively. The notations  $\bar{A}$  and  $\bar{\epsilon}$  denote the absorptivity and thermal infrared emissivity, respectively, and  $\bar{r}$  is the reflectivity. The solar input is defined by  $Q$ .

where  $\pi a_e^2$  represents the cross sectional area of the earth–atmosphere system that intercepts the incoming solar flux, and the spherical area  $4\pi a_e^2$  denotes emission in all directions. It follows that the equilibrium temperature of the system is

$$T_e = [(1 - \bar{r})S/4\sigma]^{1/4}. \quad (8.3.2)$$

With this simple equation, we may study the effect of changes in the global albedo and/or the solar constant on the equilibrium temperature of the entire system. However, the surface temperature, which is a fundamental parameter in climate studies, cannot be directly related to either the solar constant or the global albedo change. Information about the surface temperature must be related to the transparency and opacity of the atmosphere with respect to solar and thermal infrared radiation, respectively.

To include surface temperature and the radiative properties of the atmosphere in the simplest radiative equilibrium model, we may construct a two-layer model. Let the mean solar absorptivity and the thermal infrared emissivity of the earth's atmosphere be  $\bar{A}$  and  $\bar{\epsilon}$ , respectively, and assume that the earth's surface is a blackbody with a temperature of  $T$ . In reference to Fig. 8.8, the energy balance equations at TOA and the surface may be written in the forms

$$Q(1 - \bar{r}) - \bar{\epsilon}\sigma T_a^4 - (1 - \bar{\epsilon})\sigma T^4 = 0, \quad (8.3.3)$$

$$Q(1 - \bar{r} - \bar{A}) + \bar{\epsilon}\sigma T_a^4 - \sigma T^4 = 0. \quad (8.3.4)$$

Solutions for the surface and atmospheric temperatures are

$$T^4 = Q[2(1 - \bar{r}) - \bar{A}]/[\sigma(2 - \bar{\epsilon})], \quad (8.3.5)$$

$$T_a^4 = Q[\bar{A} + \bar{\epsilon}(1 - \bar{r} - \bar{A})/[\sigma\bar{\epsilon}(2 - \bar{\epsilon})]]. \quad (8.3.6)$$

These equations are highly nonlinear with many coupling terms. Thus, it is difficult to carry out sensitivity analyses concerning the effect of the radiative parameters on temperature values. However, if the absorptivity and emissivity of the atmosphere are assumed to be constants, the effect of solar constant changes on equilibrium surface and atmospheric temperatures may be studied.

### 8.3.1.2 A VERTICAL MODEL

Assuming that the atmosphere is motionless, the local time rate of change of temperature for a given atmospheric layer is associated with the net flux divergence in the form

$$\rho C_p \left( \frac{\partial T}{\partial t} \right)_{\text{RAD}} = -\frac{\partial}{\partial z} (F_s - F_{ir}), \quad (8.3.7)$$

where  $\rho$  is the air density,  $C_p$  is the specific heat at constant pressure, and  $F_s$  and  $F_{ir}$  denote the net solar and thermal infrared fluxes. Under steady-state conditions  $\partial T / \partial t = 0$ . Also, at TOA we require that  $F_s(z_\infty) = F_{ir}(z_\infty)$ ; that is, the absorbed solar flux must be balanced by the thermal IR flux emitted by the surface and the atmosphere. With this boundary condition, an integration from  $z$  to  $z_\infty$  over Eq. (8.3.7) yields

$$F_s(z) = F_{ir}(z). \quad (8.3.8)$$

This equation represents the steady-state global radiative equilibrium condition. The broadband thermal IR flux may be expressed in terms of an integral form as follows (see Section 4.5):

$$\begin{aligned} F_{ir}(z) &= \int_0^{z_\infty} \sigma T^4(z') K(|z - z'|) dz' \\ &= \sigma T_s^4 [1 - \varepsilon^f(z, T)] - \int_0^{z_\infty} \sigma T^4(z') \frac{d\varepsilon^f(|z - z'|, T(z'))}{dz'} dz', \end{aligned} \quad (8.3.9)$$

where  $K$  is a general kernel function associated with the weighting function, and  $\varepsilon^f$  is the broadband flux emissivity.

In a nongray atmosphere the radiative equilibrium temperature is determined by the balance between solar and thermal IR heating rates. The solar and IR heating rate profiles were illustrated in Sections 3.5 and 4.7. Radiative equilibrium calculations require information about the solar zenith angle, the length of the solar day, and the solar constant, as well as atmospheric composition and the earth's surface albedo.

To obtain the vertical temperature profile under radiative equilibrium, we may carry out an iterative and time-marching procedure as follows:

$$T^{(n+1)}(z) = T^{(n)}(z) + \left( \frac{\partial T}{\partial t} \right)_{\text{RAD}}^{(n)} \Delta t, \quad (8.3.10)$$

where  $n$  is the time step of the integration and  $\Delta t$  is the time interval. A numerical differencing scheme and an initial guess of the temperature are needed. Radiative

equilibrium is reached when the temperatures at the  $(n + 1)$  and  $n$  time steps differ by a small preset value. Specifically, radiative equilibrium at the surface and at TOA must be satisfied.

The time-marching method, which involves considerable computational effort, will give the evolution of the temperature as a function of time under the radiative equilibrium condition. However, if one is primarily interested in the temperature profile in the equilibrium state, the simplification given in Eq. (8.3.8) may be used. The solar flux must be balanced by the thermal IR flux. Thus, we write

$$F_s(z) = F_{ir}(z) = \int_0^{z_\infty} \sigma T^4(z') K(|z - z'|) dz'. \quad (8.3.11)$$

The kernel function  $K$  in Eq. (8.3.9) depends largely on atmospheric gaseous profiles, principally those for  $H_2O$ ,  $CO_2$ , and  $O_3$ , as well as on the distribution of cloud fields. As a good approximation, the kernel function may be considered to be independent of temperature. Thus, once the solar net flux profile has been given, the temperature profile may be determined from the following procedure.

The atmosphere can be divided into  $N$  finite vertical layers, so that Eq. (8.3.11) may be expressed in a finite difference form:

$$F_s(z_i) = \sum_{j=1}^N \sigma T^4(z_j) K(|z_i - z_j|) \Delta z_j, \quad i = 1, 2, \dots, N. \quad (8.3.12)$$

In compact matrix form, we have

$$\mathbf{F}_s = \mathbf{K} \cdot \sigma \mathbf{T}^4, \quad (8.3.13)$$

where  $\mathbf{F}_s$  and  $\sigma \mathbf{T}^4$  are  $N$  column vectors and  $\mathbf{K}$  is an  $N \times N$  matrix. Inverting the matrix leads to

$$\sigma \mathbf{T}^4 = \mathbf{K}^{-1} \mathbf{F}_s, \quad (8.3.14)$$

where  $\mathbf{K}^{-1}$  denotes the inverse of the kernel function matrix.

Figure 8.9 shows the atmospheric temperature profiles under radiative equilibrium with and without cloud contributions. Without the contribution of clouds, the surface temperature under radiative equilibrium is  $\sim 340$  K and the temperature in the tropopause is  $\sim 215$  K. In cloudy conditions, the temperature in the troposphere decreases significantly because of the reflection of solar flux by clouds. In particular, a  $\sim 30$  K reduction in surface temperature is seen. The temperature profile for average cloudiness, shown in Fig. 8.9, is obtained by accounting for clear and cloudy areas. It is evident that the radiative equilibrium temperature is much too warm near the surface and too cold in the tropopause. On a mean annual basis, the earth–atmosphere system is in radiative equilibrium at TOA. However, it is clearly not in radiative equilibrium within the atmosphere or at the surface. In terms of the one-dimensional globally averaged condition, the only mechanism that can bring the system into thermodynamic equilibrium is the vertical transport of heat by means of eddies. The convective nature of the earth–atmosphere system is, thus, fundamental to weather and climate processes, as well as to their numerical modeling.

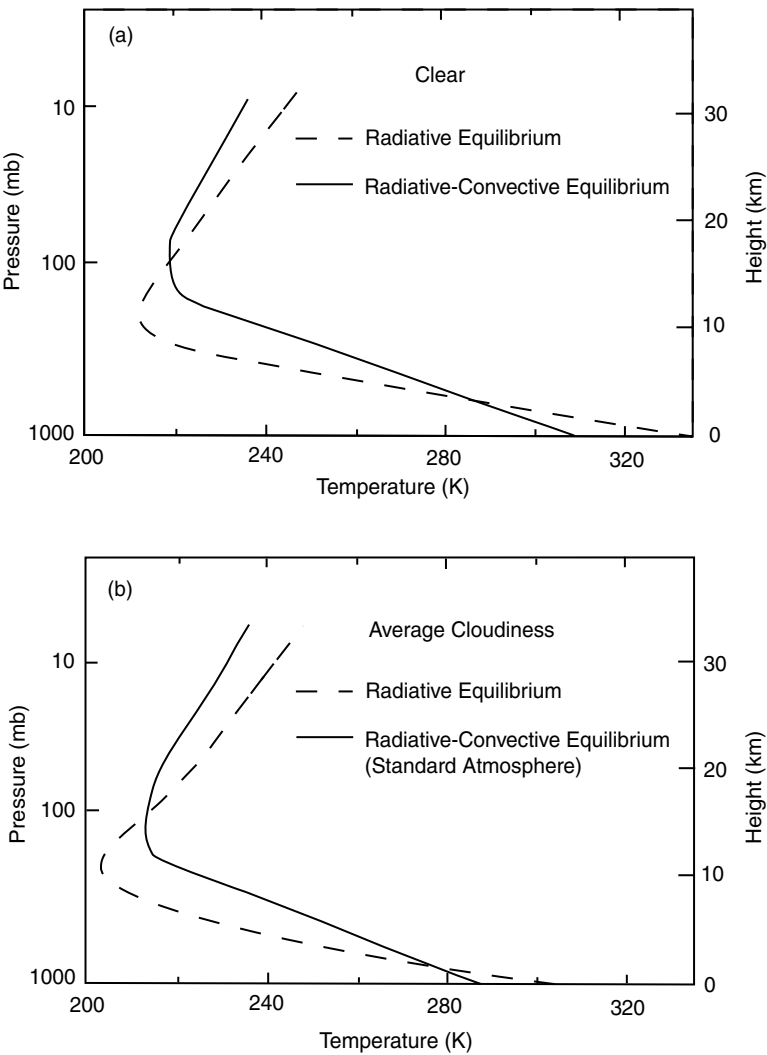


**Figure 8.9** Vertical distributions of radiative and radiative–convective equilibrium temperatures in clear (a) and average cloud (b) conditions, simulated from a one-dimensional radiative–convective climate model.

### 8.3.2 Radiative and Convective Equilibrium

#### 8.3.2.1 HEAT BUDGET OF THE EARTH–ATMOSPHERE SYSTEM

The source of energy that drives the earth’s climate comes from the electromagnetic radiation emitted from the sun. The solar constant, that is, the solar irradiance (or flux) corresponding to the mean distance between the earth and the sun available on a 1 square meter area facing the sun at TOA, is about  $1366 \text{ W m}^{-2}$  (Lean and Rind,

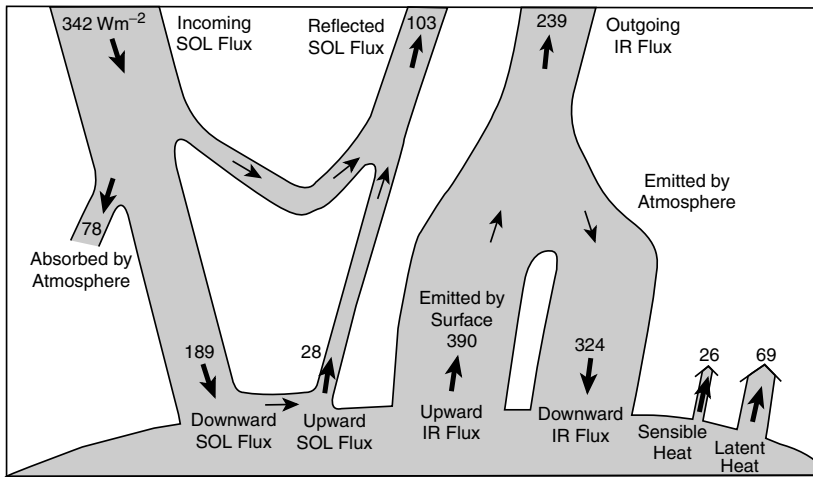


**Figure 8.10** The heat balance of the earth and the atmosphere system. The solar (SOL) constant used is  $1366 \text{ W m}^{-2}$  so that the incoming solar flux for climatological energy balance is  $342 \text{ W m}^{-2}$  (round off the decimal point), while the global albedo is taken to be 30%. The “atmosphere” referred to in the graph contains molecules, aerosols, and clouds. The atmospheric thermal infrared (IR) flux is emitted both upward and downward. The upward IR flux from the surface is computed by using a climatological surface temperature of 288 K. At the top of the atmosphere, the energy is balanced by radiative flux exchange. At the surface, however, upward sensible and latent heat fluxes must be introduced to maintain energy balance. Absorption of the solar flux is obtained from the divergence of net solar fluxes at the top and the surface. The width of the shaded area with an arrow is approximately proportional to the flux value.

1998). The cross-section area at which the earth intercepts the solar flux is  $\pi a_e^2$ , but the area of the spherical earth is  $4\pi a_e^2$ , where  $a_e$  denotes the earth’s radius. Thus, the effective average solar flux incident to a level surface at TOA is one-quarter of the solar constant, i.e.,  $342 \text{ W m}^{-2}$  (round off the decimal point). Moreover, based on satellite radiometric observations and analyses, the best estimate of the global albedo is about 30% (Jacobowitz *et al.*, 1984). This albedo is a result of multiple scattering processes involving molecules, aerosols, clouds, and the underlying surface, as illustrated in Fig. 8.10. Interactions between multiple scattering and absorption processes in the atmosphere and surface reflection determine the amount of solar flux reflected back to space. As a result of this global albedo, about  $239 \text{ W m}^{-2}$  is available on average to warm the atmosphere and the surface.

To maintain global radiative equilibrium at TOA so that an equilibrium temperature can be defined, the earth–atmosphere system itself must radiate the same amount of energy, i.e.,  $239 \text{ W m}^{-2}$ , back to space. Because the equilibrium temperature of the earth–atmosphere system is about 255 K, the emitted thermal radiation is in the infrared portion of the electromagnetic spectrum. The thermal infrared (or longwave) radiation is emitted from the surface as well as the atmosphere, as shown in Fig. 8.10. The  $239 \text{ W m}^{-2}$  outgoing infrared flux is the sum of the emitted surface flux attenuated to TOA plus the emission and absorption contributions within the atmosphere including clouds. The equilibrium temperature of the earth–atmosphere



system of 255 K is much colder than the climatological surface temperature of 288 K, which emits  $390 \text{ W m}^{-2}$  of infrared flux. As pointed out in Section 4.1, based on the standard lapse rate of  $6.5 \text{ K km}^{-1}$ , the effective scale height of the greenhouse effect of the earth's atmosphere is about 5 km.

To determine the remaining surface radiative components involving solar flux, downward infrared flux, and absorbed solar flux within the atmosphere, we use the standard atmospheric temperature and composition profiles, including all the trace gases listed in Table 3.3, and globally averaged cloud and background aerosol information noted above as inputs to a line-by-line radiative transfer model. The solar flux reaching the surface is about  $189 \text{ W m}^{-2}$ , while the reflected solar flux is  $28 \text{ W m}^{-2}$ , based on a globally averaged surface albedo of 15%. It follows that the absorbed solar flux at the surface is  $161 \text{ W m}^{-2}$ . On the other hand, the emitted downward infrared flux from the atmosphere reaching the surface is  $324 \text{ W m}^{-2}$ , leading to a net loss of thermal infrared flux by the earth's surface of  $66 \text{ W m}^{-2}$ . The net radiative energy gain at the surface due to the absorption of solar flux and the emission of thermal infrared flux is about  $95 \text{ W m}^{-2}$ . This gain is countered by the transport of sensible and latent heat fluxes out of the surface in order to maintain an overall heat balance. The absorbed solar flux within the atmosphere is about  $78 \text{ W m}^{-2}$ , which is obtained from the divergence of net solar fluxes at TOA and the surface.

The average annual ratio of sensible to latent heat loss at the surface, the so-called *Bowen ratio*, has a global value of about 0.27. Thus, the latent and sensible heat fluxes are  $69 \text{ W m}^{-2}$  and  $26 \text{ W m}^{-2}$ , respectively. As illustrated in Fig. 8.6, the atmosphere experiences a net radiative cooling that must be balanced by the latent heat of condensation released in precipitation processes and by the convection and conduction of sensible heat from the underlying surface. If there were no latent and sensible heat transfer, the earth's surface would have a temperature much higher than the observed value of 288 K.

#### 8.3.2.2 CONVECTIVE ADJUSTMENT

The incoming solar flux at the top of the atmosphere must be balanced by the reflected solar and emitted infrared fluxes over a climatological time scale, since the only energy exchange with space is by means of radiative processes. At the surface, however, equilibrium must be achieved by the balance between net radiative fluxes and convective fluxes of sensible and latent heat, as explained in the previous subsection. Vertical fluxes of sensible and latent heat are governed by the motions involving various scales. In the molecular boundary layer, about 1 mm adjacent to the surface, the principal mechanisms for the transport of sensible and latent heat fluxes are conduction and diffusion. In the layer immediately above that, and within about a few tens of meters of the surface, defined as the surface layer, sensible and latent heat fluxes are transferred upward by means of eddies. Based on the theory of turbulence, the surface layer is characterized by strong vertical wind shear, with wind speed proportional to the logarithm of height. Above this layer, up to about 1 km, is the mixed layer, where convectively driven thermals assume the primary role of transporting the

vertical sensible and latent heat fluxes. From the mixed layer to the tropopause, the upward transport of sensible and latent heat is governed by deep cumulus convection, as well as by synoptic and planetary-scale circulations. In this region, essentially all conversion of latent to sensible heat takes place via irreversible condensation processes. The preceding scales of vertical motion associated with the transport of sensible and latent heat are generally classified as *convection*.

The simplest way to account for convection in a global model for climate studies is the *convective adjustment scheme* based on the concept of static stability, first introduced by Manabe and Wetherald (1967). To present this scheme, we shall begin with the first law of thermodynamics in the form

$$C_p \frac{dT}{dt} + g \frac{dz}{dt} + L \frac{dq}{dt} = Q_R, \quad (8.3.15a)$$

where  $L$  is the latent heat per unit mass,  $q$  is the specific humidity, and  $Q_R$  represents radiative heat exchange. Consider this law in the context of one-dimensional space. The local rate of temperature change may be expressed in terms of static stability and radiative flux divergence in the form

$$\rho C_p \frac{\partial T}{\partial t} = \rho C_p w (\gamma - \gamma_c) + \rho Q_R, \quad (8.3.15b)$$

where the vertical velocity  $w = dz/dt$ , the atmospheric lapse rate  $\gamma = -\partial T/\partial z$ , and

$$\gamma_c = \gamma_d + \frac{L}{C_p} \frac{dq}{dz}. \quad (8.3.16)$$

The dry adiabatic lapse rate,  $\gamma_d = g/C_p$ , while the last term in Eq. (8.3.16) represents a modification of the dry adiabatic lapse rate due to the saturation specific humidity gradient. Since specific humidity generally decreases with height, it has a negative value. The value of  $\gamma_c$  depends on the atmospheric humidity profile and varies from the tropics to the polar regions.

The local rate of temperature change, as shown in Eq. (8.3.15b), depends on the convective nature of the atmosphere, which is governed by atmospheric stability and the radiative flux exchange in the atmosphere. For the latter, let the radiative flux divergence in the vertical,  $\rho Q_R$ , be denoted by  $-\partial F/\partial z$ . For atmospheric stability, the divergence of the convective flux may be written as

$$-\frac{\partial F_v}{\partial z} = \rho C_p w (\gamma - \gamma_c). \quad (8.3.17)$$

If  $\gamma \leq \gamma_c$ , there will be no transport of convective flux. We may separate convective and radiative contributions to temperature perturbations as follows:

$$\rho C_p \frac{\partial T}{\partial t} = \rho C_p \left[ \left( \frac{\partial T}{\partial t} \right)_{\text{CON}} + \left( \frac{\partial T}{\partial t} \right)_{\text{RAD}} \right] = -\frac{\partial F_v}{\partial z} - \frac{\partial F}{\partial z}. \quad (8.3.18)$$

Since a large portion of solar flux is absorbed at the surface, the air immediately above it is mostly unstable. In a one-dimensional context, the vertical transport of sensible and latent heat fluxes from the surface to the atmosphere is principally due to eddy motion.

In the convective adjustment scheme, the atmosphere is divided into layers that include nonconvection, convection without contact with the surface, and convection in contact with the surface. For a nonconvective layer, there would be no variation in the vertical eddy flux, so that

$$-\frac{\partial F_v}{\partial z} = \rho C_p \left( \frac{\partial T}{\partial t} \right)_{\text{CON}} = 0, \quad (8.3.19)$$

resulting in no adjustment. In a convective layer that is not in contact with the surface, the vertical temperature profile is numerically adjusted by using a critical lapse rate,  $\gamma_c$ , under the condition that the total potential energy is conserved within the layer. That is,

$$\int_{z_b}^{z_t} \rho C_p \left( \frac{\partial T}{\partial t} \right)_{\text{CON}} dz = - \int_{z_b}^{z_t} \frac{\partial F_v}{\partial z} dz = F_v(z_b) - F_v(z_t) = 0, \quad (8.3.20)$$

where  $z_t$  and  $z_b$  denote the top and bottom heights, respectively, of the unstable layer. This implies that convection develops when the atmospheric lapse rate exceeds the critical lapse rate. Convection then transports heat upward until the critical lapse rate is established, resulting in a redistribution of temperature with the total energy conserved. When a convective layer is in contact with the surface, the heat flux from the surface must be considered. Thus,

$$\int_0^{z_t} \rho C_p \left( \frac{\partial T}{\partial t} \right)_{\text{CON}} dz = - \int_0^{z_t} \frac{\partial F_v}{\partial z} dz = F_v(0) - F_v(z_t) = F(0), \quad (8.3.21)$$

where  $F(0)$  is the net radiative flux at the surface.

On the basis of Eqs. (8.3.19)–(8.3.21), an iterative procedure may be constructed for the computation of  $(\partial T / \partial t)$ . This procedure begins at the surface and progressively scans the layers above it until all layers of the supercritical lapse rate have been eliminated. This process is repeated at each time step. Atmospheric temperatures are first constructed based on the balance between the radiative heating and cooling rates. Then the surface temperature is calculated from the balance of the solar and IR net fluxes at the surface. Since solar fluxes heat the surface, there will be net upward fluxes, which are distributed in the layer above the surface according to Eq. (8.3.21). Adjusting the temperature in steps upward and using Eq. (8.3.20) whenever the layer is convectively unstable eliminates all the supercritical lapse rates. For applications to one-dimensional climate models, the critical lapse rate,  $\gamma_c$ , is usually assumed to be  $6.5 \text{ K km}^{-1}$  for the globally averaged condition. This number is based on the fact that the climatological atmospheric temperature profile in the troposphere has a lapse rate close to this value.

Manabe and Wetherald (1967) performed the first sensitivity experiment of the radiative–convective model described above to examine radiative forcings of carbon dioxide and solar input. Figure 8.9b shows the effects of clouds on the vertical

distribution of equilibrium temperature. With average cloudiness, this profile is close to the standard atmospheric profile. Temperatures without the inclusion of clouds are much higher than those with clouds; a difference of as much as 20 K is shown for the surface temperature. The temperature difference decreases with height.

## 8.4 Radiation in One-Dimensional Climate Models

### 8.4.1 Carbon Dioxide Greenhouse Effects

One of the major concerns in climate studies has been the impact on the earth's surface temperature of the steady increase in atmospheric carbon dioxide content produced by the rapid burning of fossil fuels. Since the beginning of the Industrial Revolution more than a century ago, carbon has been removed from the earth in the form of coal, petroleum, and natural gas. In burning processes, carbon dioxide is formed through the oxidation reaction,  $C + O_2 \rightarrow CO_2$ . Of all the  $CO_2$  that has been produced, about half is believed to remain in the atmosphere, while the other half has dissolved in the oceans or been absorbed by the earth's biomass, primarily the forests.

As discussed in Section 3.2.3,  $CO_2$  is virtually transparent to solar radiation. However, it is a strong absorber in the  $15\text{ }\mu\text{m}$  band ( $\sim 12\text{--}18\text{ }\mu\text{m}$ ) of the thermal IR spectrum, as described in Section 4.2.1. The  $15\text{ }\mu\text{m}$  band consists of the  $\nu_2$  fundamental, the combination bands, the hot bands, and the  $P$ ,  $Q$ , and  $R$  branches of the rotational transitions (Fig. 4.2). An increase in atmospheric  $CO_2$  content can cause the additional trapping of the outgoing thermal IR radiation emitted from the surface and lower atmosphere, thereby enhancing the greenhouse effect. Arrhenius (1896) was the first to recognize the potential effect of increased  $CO_2$  concentration on the earth's heat budget and hence, atmospheric temperature. He estimated that an increase in the  $CO_2$  concentration by a factor of 2.5 to 3 would result in a globally averaged temperature increase of  $8\text{--}9^\circ\text{C}$ , an estimate that was not too far from that produced by sophisticated computer models. In the following, we shall first discuss the carbon cycle.

Variations in  $CO_2$  over different geographical areas are relatively small because the variability in the sources and sinks of  $CO_2$  is small at the earth's surface. Atmospheric  $CO_2$  is removed from and released into the atmosphere through a number of natural processes. A considerable amount of  $CO_2$  dissolves annually into the oceans and returns to the atmosphere by a reverse process. A significant component of atmospheric  $CO_2$  consumption appears to be photosynthesis, via the reaction  $CO_2 + H_2O + h\nu \rightleftharpoons CH_2O + O_2$ . The sedimentary layer of the earth's crust, the lithosphere, contains a considerable amount of carbon from which  $CO_2$  is formed through oxidation processes. These  $CO_2$  cycles appear to introduce little change in the total amount of  $CO_2$  in the atmosphere.

Measurements of atmospheric  $CO_2$  have been made at the South Pole since 1957 and at Mauna Loa, Hawaii, since 1958. The mean monthly concentration record from Mauna Loa, displayed in Fig. 8.11a, has been frequently employed to illustrate a steady increase in the atmospheric  $CO_2$  concentration due largely to human

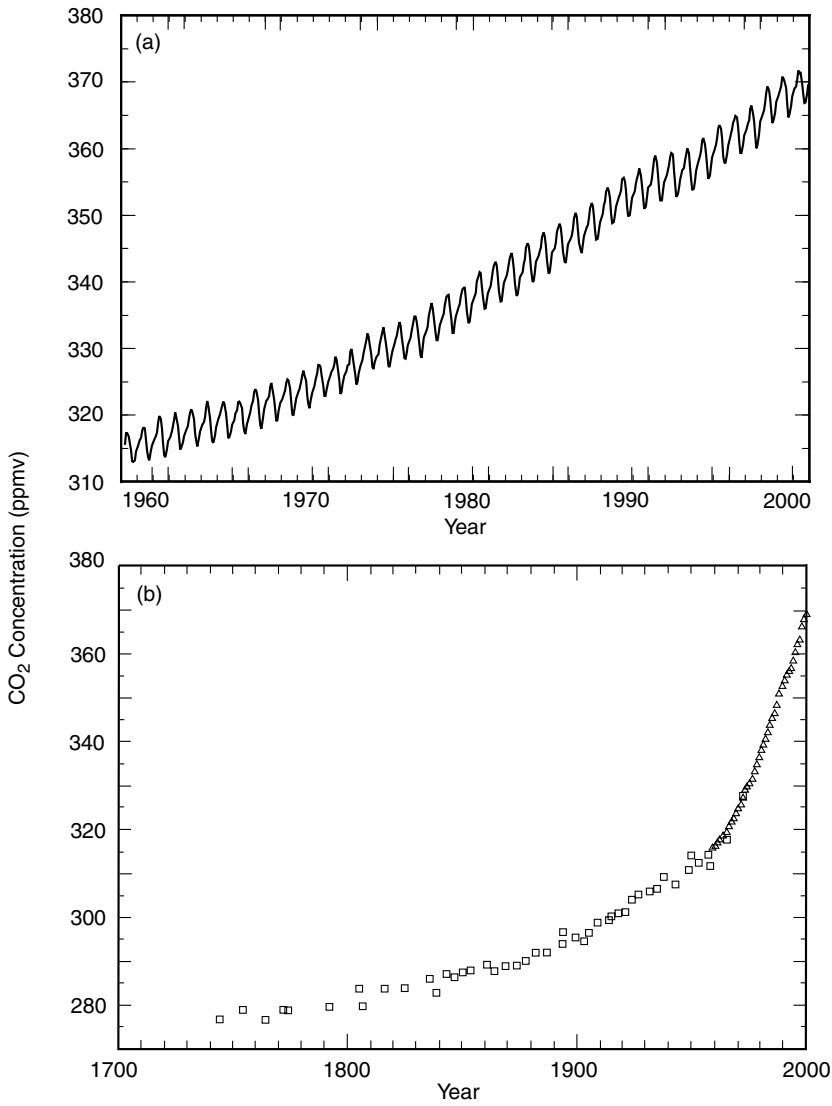


**Figure 8.11** (a) Concentration of atmospheric CO<sub>2</sub> at Mauna Loa Observatory, Hawaii, expressed as a mole fraction in parts per million of dry air for the period 1958–2000 (courtesy of Pieter Tans, Environmental Research Laboratory, National Oceanic and Atmospheric Administration). (b) Atmospheric CO<sub>2</sub> concentration for the past 250 years as indicated by measurements in air trapped in ice core from Antarctica determined by Neftel *et al.* (1985) and extended to the present using the Mauna Loa record displayed in (a).

activities, in particular fossil fuel combustion, as well as land-use conversion. The rate of increase varies from 1958 to the present time, but an average of 0.4% per year is a good estimate. The atmospheric CO<sub>2</sub> concentration records prior to 1957 primarily come from ice-core measurements taken in Antarctica (Fig. 8.11b). Over the past 1000 years, CO<sub>2</sub> concentrations were relatively constant with a value of about 280 parts per million by volume (ppmv) and varied within about  $\pm 10$  ppmv. The significant increase in CO<sub>2</sub> concentration since the onset of industrialization in about 1860 closely follows the increase in CO<sub>2</sub> emissions from fossil fuels.

Evaluation of the carbon budget of the atmosphere–ocean–land system is an ongoing, complex research program because of the many uncertainties in the various carbon processes and their lifetimes, particularly those processes involving the terrestrial biosphere. CO<sub>2</sub> is removed from the atmosphere by numerous processes that operate on different time scales, and is then transferred to a number of reservoirs. The fastest process is its uptake into vegetation and the surface layer of the oceans, which takes place over a few years. Transfer of CO<sub>2</sub> to soils and to the deep ocean operates on the century time scale. It has been estimated that within about 30 years, about 40–60% of the CO<sub>2</sub> currently released to the atmosphere will be removed. The average annual anthropogenic carbon budget has been estimated including emission of CO<sub>2</sub> from fossil fuel combustion and cement production of about 5.5 GtC/yr (1 Gt = 10<sup>12</sup> kg), and the net emissions from changes in land use of about 1.6 GtC/yr. Storage in the atmosphere is about 3.3 GtC/yr, while ocean uptake of CO<sub>2</sub> is about 2.0 GtC/yr. Other reservoirs include uptake by forest regrowth, nitrogen fertilization, CO<sub>2</sub> fertilization and climate effects, which account for about 1.8 GtC/yr. Future rates of CO<sub>2</sub> increase in the atmosphere are uncertain because the rates of release and the rates at which CO<sub>2</sub> will be taken up by the ocean and the land biota are not known with great precision. However, projections of the future increase of CO<sub>2</sub> have been made by carbon cycle and climate models based on scenarios concerning the use of fossil energy sources. For example, most climate modelers employ business-as-usual scenarios for future greenhouse gas amounts.

Extensive numerical experiments using a one-dimensional climate model have been performed to investigate the effects of an increase in CO<sub>2</sub> on temperature, beginning with the pioneering work of Manabe and Wetherald (1967). These equilibrium experiments were generally performed by doubling a fixed CO<sub>2</sub> concentration (e.g., from 300 to 600 ppmv). Various feedbacks involving moisture that are associated with CO<sub>2</sub> doubling have been investigated by Hansen *et al.* (1981) using a one-dimensional model. Based on a fixed relative humidity, a lapse rate of 6.5 K km<sup>-1</sup>, and a prescribed cloud altitude, the equilibrium surface temperature,  $T_s$ , increases. This is because rising temperatures in the atmosphere and at the surface increase the water vapor concentration in the atmosphere, which in turn traps more thermal IR radiation and, to a lesser degree, absorbs more solar radiation. The feedback due to increasing water vapor through higher temperatures is positive. If, however, a moist adiabatic lapse rate is used instead of a fixed lapse rate,  $T_s$  is less sensitive to radiative perturbations as more moisture is added to the atmosphere because of the decreasing lapse rate. Subsequently, the temperature differences between the top of the convective

region and the surface are reduced, and  $\Delta T_s$  decreases. Thus, the feedback due to the use of a moist adiabatic lapse rate is negative. The surface temperature change,  $\Delta T_s$ , is sensitive to the assumption of fixed versus varying cloud altitude. The assumption that clouds move to a higher altitude as temperature increases results in a greater  $\Delta T_s$  than for the case in which cloud altitude is assumed fixed. Clouds that move aloft enhance the trapping of thermal IR emission from the surface by water vapor and exert a positive feedback. However, hypothetical black clouds were used in the early one-dimensional climate models, and thus cloud radiative properties were not properly accounted for.

The exchange of latent and sensible heat and radiative fluxes through the planetary boundary layer provides an important source of ocean–atmospheric interaction and hence plays a significant role in climate perturbations. Through hydrological cycle feedbacks, surface warming due to doubled  $\text{CO}_2$  may be divided into three processes. The first two processes involve direct surface and atmospheric heating due to the greenhouse effect of doubled  $\text{CO}_2$ . The third process is related to the interactions among the ocean surface temperature, the hydrological cycle, and the tropospheric convective adjustment. Surface warming due to the first two processes enhances the evaporation of water vapor into the troposphere, which indirectly amplifies surface warming via the latent heat release within the troposphere and increases the tropospheric absolute humidity that, in turn, increases downward IR emission to the surface. Based on one-dimensional model calculations, the third process is most significant in the feedback process (Ramanathan, 1981). Overall, the one-dimensional models show a surface temperature increase of about 2–3°C in the doubling of  $\text{CO}_2$  concentration experiments.

## 8.4.2 Ozone and Other Greenhouse Gases

### 8.4.2.1 OZONE

As presented in Section 3.2.2, ozone is produced primarily in the middle and upper stratosphere by three-body collisions involving molecular oxygen,  $\text{O}_2$ , its atomic form,  $\text{O}$ , and a third body. Atomic oxygen is produced by the photolysis of  $\text{O}_2$  due to the absorption of solar fluxes with wavelengths shorter than 2423 Å. The destruction of  $\text{O}_3$  is mainly due to the catalytic effects of various free radical species, including nitrogen oxides, chlorine oxides, and hydrogen oxides. The excited atomic oxygen in the  $^1\text{D}$  state, produced by the photodissociation of ozone from solar wavelengths shorter than 3100 Å, is essential for the production of these radicals. Ozone absorbs solar radiation in the UV Hartley and Huggins bands and in the visible Chappuis band, as discussed in Section 3.2.1. The majority of the heating at altitudes above ~45 km is due to absorption in the Hartley band, while the heating below ~30 km is due to absorption in the Chappuis band. In the infrared,  $\text{O}_3$  exhibits a number of vibrational–rotational bands. The 9.6  $\mu\text{m}$  band is most important because of its location in the window region.

The total column ozone concentrations have been decreasing over much of the globe at a rate of about 4–5% per decade at midlatitude in both hemispheres, according to ground-based and satellite observations. As indicated in Section 3.2.2, a deep

ozone hole has developed over Antarctica since the mid-1970s, with a decrease of as much as 50% or more during austral spring. This ozone hole is caused by heterogeneous chemical reactions between chlorine species derived from CFCs and polar stratospheric ice clouds. In addition, the average stratospheric ozone depletion over the past decade appears to be associated with the injection of sulfur dioxide from the Mt. Pinatubo volcanic eruption in 1991. A reduction in stratospheric  $O_3$  could lower the temperature in the region in which it occurs because of the reduction of UV absorption. At the same time, however, two competing effects on tropospheric and surface temperatures are produced. First, more solar UV and visible fluxes could reach the troposphere and surface, leading to a warming effect. On the other hand, the greenhouse effect, due to the trapping of IR fluxes by  $O_3$ , could be reduced and, in turn, cooling could result. The competition of these two effects determines whether the troposphere is warmed or cooled due to the decrease in  $O_3$ .

Based on one-dimensional climate models, a reduction in the concentration of  $O_3$  would lead to a decrease in atmospheric and surface temperatures. Temperature perturbations due to other radiative forcings, such as a doubling of  $CO_2$ , may lead to changes in the reaction rates involving ozone. This in turn affects the ozone concentration. Increases in the  $CO_2$  concentration reduce stratospheric temperatures, resulting in an increase in the total ozone due to a slowing down of the ozone loss reaction rate. The uncertainty involved in these chemical reaction rates, however, is very large.

Contrary to stratospheric ozone, tropospheric ozone, about 10% of the total column ozone, has increased in the Northern Hemisphere over the past three decades. This increase has been closely associated with gaseous exchanges between the surface and the atmosphere, regional gaseous emissions, and aerosol and cloud processes. For example, anthropogenic sources of hydrocarbons, methane, nitrous oxide, and carbon monoxide enhance the formation of tropospheric ozone. Also, cumulus convection and precipitation, as well as heterogeneous chemical processes occurring within clouds, have a profound effect on tropospheric chemistry involving ozone. In the upper troposphere, the injection of nitric oxide from aircraft can produce excess ozone. The greenhouse effect of the increased tropospheric ozone, associated with its IR emission at the  $9.6\ \mu\text{m}$  band, appears to be rather important (see Fig. 8.12).

#### 8.4.2.2 METHANE

As described in Section 4.2.1, methane exhibits an absorption band at  $\sim 1400\ \text{cm}^{-1}$  ( $7.6\ \mu\text{m}$ ) and is a greenhouse gas. Atmospheric  $CH_4$  has been increasing since the beginning of the 19th century. The current levels of methane are about 1.7–1.8 ppmv and are the highest that have been observed, including in the ice-core records that go back to 1850. The primary natural source of  $CH_4$  appears to be microbial decay of organic matter under anoxic conditions in wetlands. Anthropogenic sources include rice production, termites, bacterial decay in landfills, leakages from the use of fossil fuels and natural gas, and biomass burning, the sum of which may be twice as great as that from natural sources. The atmospheric concentration of  $CH_4$  is controlled by its reaction with hydroxyl radicals in the troposphere via the reaction  $CH_4 + OH \rightarrow H_2O + CH_3$ . This reaction is largely the result of water vapor in the troposphere. The  $CH_4$  growth rate has declined in recent years, probably in part because of the increase



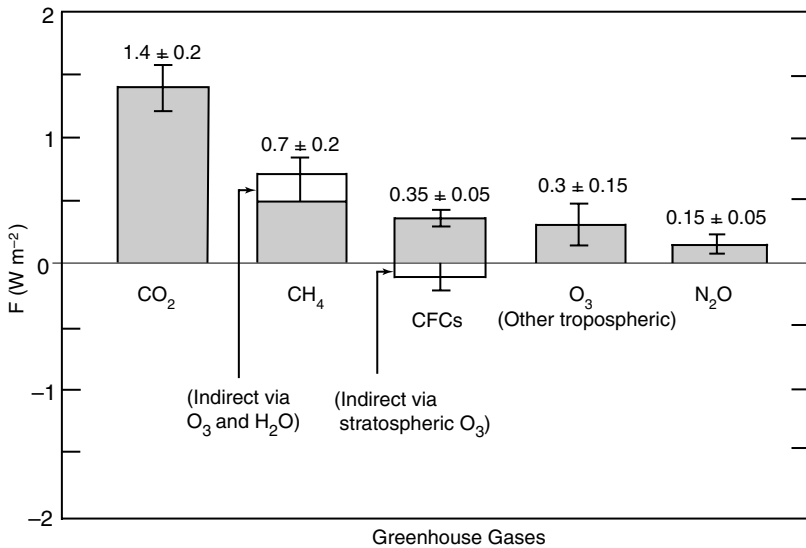


**Figure 8.12** Estimated climatic radiative forcings between 1850 and 2000 produced by CO<sub>2</sub>, CH<sub>4</sub>, CFCs, O<sub>3</sub>, and N<sub>2</sub>O. Indirect effects associated with CH<sub>4</sub> and CFCs, as well as uncertainties, are also displayed (data taken from Hansen *et al.*, 2000).

in chemical emissions such as CO that affect the production of OH, the primary sink for CH<sub>4</sub>.

Based on one-dimensional climate models, a doubling of CH<sub>4</sub> from 1.7 to 3.4 ppmv would lead to an increase in the surface temperature of ~0.2–0.4°C (Wang *et al.*, 1986). Moreover, changes in the CH<sub>4</sub> concentration may affect the global O<sub>3</sub> distribution through reactions with OH and other trace gases. An increase in CH<sub>4</sub> may lead to an increase in O<sub>3</sub> and H<sub>2</sub>O via the net reaction  $\text{CH}_4 + 4\text{O}_2 \rightarrow \text{CH}_2\text{O} + \text{H}_2\text{O} + 2\text{O}_3$ , if enough NO is present (Crutzen, 1983). The process is a positive feedback to the radiative forcing involving CH<sub>4</sub>.

#### 8.4.2.3 NITROUS OXIDE

N<sub>2</sub>O exhibits complex IR absorption bands located at 7.9 μm that overlap with the CH<sub>4</sub> bands. The mixing ratio of N<sub>2</sub>O is ~0.3 ppmv and it has a long atmospheric lifetime of ~120 years. The principal atmospheric source of N<sub>2</sub>O is denitrification in natural and agricultural biomass. The oceans are also a significant source of N<sub>2</sub>O. Measurements indicate a global increase in the N<sub>2</sub>O concentration at a rate of ~0.2% per year, attributable to the increase in fossil fuel combustion and fertilizer denitrification. Based on a one-dimensional radiative–convective model, the surface temperature is estimated to increase by ~0.3 to 0.4°C as a result of a doubling of N<sub>2</sub>O from 0.3 to 0.6 ppmv (Wang *et al.*, 1986). Dissociation of N<sub>2</sub>O by excited oxygen atoms, O(<sup>1</sup>D), is the major source of nitrogen oxides (NO<sub>x</sub> = NO, NO<sub>2</sub>) [see Eqs. (3.2.13)–(3.2.14)]. NO<sub>x</sub> are important in determining the distribution of both tropospheric and stratospheric O<sub>3</sub>. At ~25 km, the net effect of NO<sub>x</sub> additions to the stratosphere will be to

lower the  $O_3$  concentration. However, below  $\sim 25$  km in the stratosphere,  $NO_x$  protect ozone from destruction (Crutzen, 1983).

#### 8.4.2.4 HALOCARBONS

As discussed in Section 4.2.1, chlorofluorocarbons (CFCs) are important greenhouse gases because of their absorption in the  $10\ \mu\text{m}$  window region. CFCs comprise a family of compounds containing chlorine and fluorine in various combinations. Their sources are generally manufactured. Most of them are chemically inert and have long atmospheric lifetimes on the order of 100 years. The most prevalent CFCs are CFC-11 ( $CFCl_3$ ) and CFC-12 ( $CF_2Cl_2$ ). Chlorine can be released in the form of  $Cl_x$ , via, e.g.,  $CFCl_3 + h\nu \rightarrow CFCl_2 + Cl$ , which can erode the ozone layer via the catalytic destruction reactions described in Eqs. (3.2.13)–(3.2.14). The growth rate of atmospheric CFCs produced by refrigerants and spray-can propellants noted in the 1970s, particularly CFC-11 and CFC-12, has been reduced as a result of production restrictions imposed by the Montreal Protocol and its Amendments (IPCC, 1996). Most CFCs will be phased out if production agreements are followed.

The direct climatic effects of CFCs and other bromocarbons are exerted through their absorption of IR radiation in the atmospheric  $10\ \mu\text{m}$  window (Ramanathan *et al.*, 1987). The indirect effects are associated with the destruction of ozone by the chlorine and bromine released through photodissociation. There is an overall negative feedback due to this indirect radiative forcing, as noted in Subsection 8.4.2.1.

Finally, we note that carbon monoxide does not exhibit a significant IR absorption band. However, it is a climatically important gas because of its chemical reactions involving  $O_3$ ,  $CO_2$ , and  $CH_4$  in the troposphere. The anthropogenic component of CO production is associated with transportation, industrial fossil fuel combustion, deforestation, and biomass burning, as well as modification of  $CH_4$  source via the principal reaction  $CO + OH \rightarrow CO_2 + H$ . This reaction leads to the reduction of OH concentrations, which, in turn, affects the lifetimes of a number of other gases, principally  $CH_4$  and  $SO_2$ .

Figure 8.12 summarizes the radiative forcings of the principal greenhouse gases, including direct and indirect effects, as estimated by Hansen *et al.* (2000). Direct radiative forcing is defined as the gain or loss of radiative flux in the earth–atmosphere system produced by the addition or reduction of a specific greenhouse gas in the system. Indirect radiative forcing is that generated by the increase or decrease of one greenhouse gas (e.g.,  $O_3$ ) caused by the addition of another greenhouse gas (e.g.,  $CH_4$ ). Climatic radiative forcing by  $CO_2$  is the largest, with a value of about  $1.4\ \text{W m}^{-2}$ , produced by the increase from the preindustrial concentration of about 278 ppmv to the current level of about 365 ppmv. Forcing by  $CH_4$ , including the indirect effects via  $O_3$  and  $H_2O$ , is half as large as that of  $CO_2$ . The total forcing by all non- $CO_2$  greenhouse gases combined is comparable to that of  $CO_2$ .

#### 8.4.3 Radiation Feedback Consideration

In Section 8.4.1, we discussed various feedbacks involving water vapor that are associated with greenhouse perturbations. The  $H_2O$  concentration varies substantially

with space and time. In the troposphere it is determined by the local hydrological cycle of evaporation, condensation, and precipitation, and by large-scale transport processes. From the analysis of measured  $\text{H}_2\text{O}$  concentrations across the globe, the mean annual relative humidity, RH, as a function of height, is fairly constant, i.e.,

$$\text{RH}(z) = \frac{q(z)}{q_s(z)} \cong \text{const}, \quad (8.4.1)$$

where  $q$  is the specific humidity and  $q_s$  is its saturation value. The saturation of specific humidity can be expressed in terms of the saturation vapor pressure as follows:

$$q_s = \frac{\varepsilon e_s}{p}, \quad (8.4.2)$$

where the ratio of the molecular weight of water vapor to that of dry air,  $\varepsilon$ , is 0.622, and  $p$  is the air pressure. Based on the conservation of the Gibbs function during phase changes, the differential changes of the saturation vapor pressure with respect to temperature are governed by the Clausius–Clapeyron equation in the form

$$\frac{de_s}{dT} = \frac{L}{R_v} \frac{e_s}{T^2}, \quad \text{or} \quad d \ln e_s = \left( \frac{L}{R_v T} \right) d \ln T, \quad (8.4.3)$$

where  $L$  is the latent heat involving vapor and water, and  $R_v$  is the gas constant for water vapor. By integration and empirical fitting, we have

$$e_s(\text{mb}) = 6.11 \exp \left[ \frac{a(T - T_o)}{T - b} \right], \quad (8.4.4)$$

where  $T_o = 273.16$  K;  $a = 21.874$  and  $b = 7.66$  if  $T \leq 273.16$  K; and  $a = 17.269$  and  $b = 35.86$  if  $T > 273.16$  K.

As a result of the increasing greenhouse gases discussed above, both surface and tropospheric temperatures increase. It follows that the amount of tropospheric water vapor in saturated air increases. Consequently, since the relative humidity in the troposphere is fairly constant, the amount of absolute water vapor increases there and traps more IR flux emitted from the surface and lower atmosphere through rotational and vibrational line spectra. This leads to a further increase in the surface temperature, a positive feedback mentioned in Section 8.4.1. The degree and extent of this positive feedback must be determined from appropriate climate models.

One final note is in order regarding the surface temperature,  $T_s$ , and emitted IR flux at the top of the atmosphere,  $F_{ir}(z_\infty)$ . Although their relationship is complex from the perspective of radiative transfer and convection in the atmosphere, to the extent that the temperature profiles have more or less the same shape at all latitudes, and that the IR fluxes are dependent on temperature at all levels, we may, to a good approximation, relate these two in a linear form as follows:

$$F_{ir}(z_\infty) \cong a + bT_s, \quad (8.4.5)$$

where the empirical coefficients  $a \cong 216 \text{ W m}^{-2}$  and  $b = 1.58 \text{ W m}^{-2} \text{ C}^{-1}$  are determined from the analysis of climatological records of zonal surface temperature,

cloud cover, and satellite-observed IR fluxes (see Section 8.5.2 for further discussion). If we use the climatological mean annual surface temperature of  $15^{\circ}\text{C}$ , we obtain an IR flux of  $239.7 \text{ W m}^{-2}$ . This value is about the same as  $Q(1 - r)$ , if we use a solar constant of  $1366 \text{ W m}^{-2}$  (i.e.,  $Q \cong 342 \text{ W m}^{-2}$ ) and a global albedo of 30%. Thus, Eq. (8.4.5) satisfies the requirement of radiative equilibrium at TOA. It also accounts for the convective nature of the lower atmosphere, since the surface temperature in this equation represents the value corresponding to radiative–convective equilibrium.

From Eq. (8.4.5), we may study the sensitivity of surface temperature with respect to IR flux. By differentiation, we have

$$\frac{\Delta T_s}{\Delta F_{ir}} = \frac{1}{b} \cong 0.63^{\circ}\text{C}/(\text{W m}^{-2}). \quad (8.4.6)$$

Radiative forcing calculations for the doubling of the  $\text{CO}_2$  concentration from 300 to 600 ppmv reveal an increase in  $F_{ir}$  of about  $4 \text{ W m}^{-2}$ , which translates to an increase in the surface temperature of about  $2.52^{\circ}\text{C}$ .

#### 8.4.4 Aerosols and Radiation

In Section 5.1, we discussed in some detail the size, shape, and type of atmospheric aerosols produced by both natural and anthropogenic processes. Aerosol particles in the atmosphere can affect the radiation balance of the earth–atmosphere system by reflecting sunlight back into space, by absorbing sunlight, and by absorbing and emitting IR radiation. Aerosols are usually considered to be important for their influence on solar radiation in which the significance of scattering relative to absorption is determined by the aerosols’ chemical composition and particle size distribution and shape. However, if the size of aerosol particles is comparable to the thermal infrared wavelength, particularly in the  $10 \mu\text{m}$  window region, they can function to trap the infrared radiation and produce the greenhouse effect. All the recent radiative forcing studies involving aerosols essentially focus on their impact on solar radiation, referred to as the *direct effect*. In Section 5.4, we presented extinction coefficients, single-scattering albedos, asymmetry factors, and phase functions for representative aerosol particles. Aerosols can also act as condensation and/or ice nuclei, which can modify the optical properties, amount, and evolution of clouds, referred to as the *indirect effect*. Climatic perturbations caused by this effect are largely unknown at this point and are a subject of contemporary research and development.

For climatic forcing investigations, aerosols are classified according to their location in the troposphere and the stratosphere. Stratospheric aerosols are usually associated with volcanic eruptions. Volcanic dust and particles formed via photochemical reactions involving sulfur dioxide are generally smaller than  $1 \mu\text{m}$  with small absorption in the visible. Consequently, their effects are primarily associated with the reflection of sunlight leading to cooling of the surface. The radiative effects of aerosols on the temperature of a planet depend not only on their optical depth, visible absorptance, and average size, but also on the variation of these properties with time. Aerosol particles resulting from volcanic activity can reach the stratosphere, where

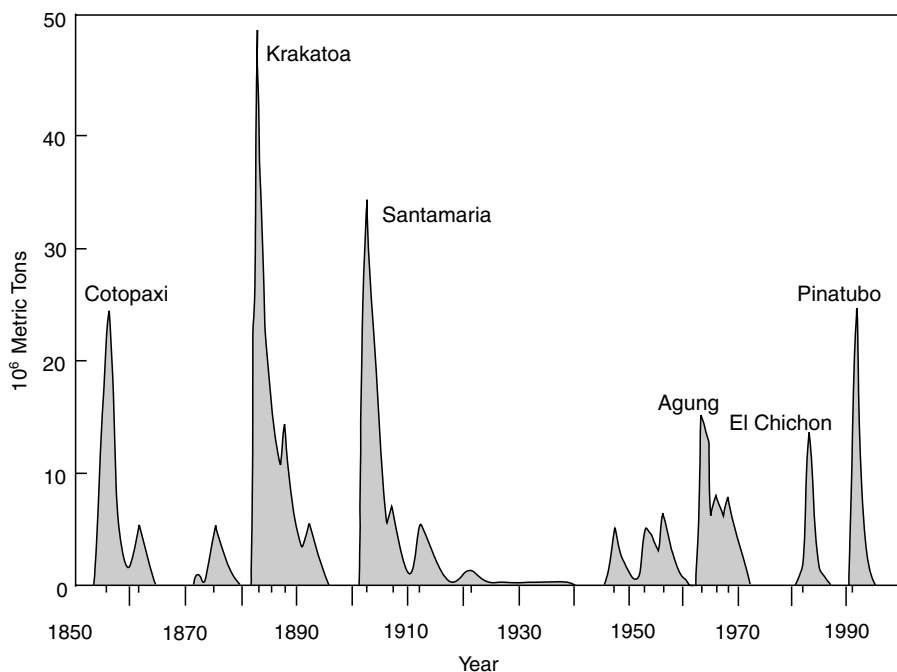


**Figure 8.13** Estimated chronology of annual average global aerosol loading by volcanic activity from 1850 to 2000. Major volcanic episodes are indicated in the diagram (data taken from *Study of Man's Impact on Climate*, 1971; Sato *et al.*, 1993).

they are transported by general circulation around the globe over many months or years and can cause anomalous weather.

Figure 8.13 displays the chronological series of major volcanic eruptions and the estimated annual average global aerosol loading dating back to 1850. The period from 1850 to 1920 was characterized by frequent eruptions of climatic importance. From 1920 to about 1960 was a period of reduced aerosol loading. Since 1960, volcanic aerosol loading has increased. The most recent episode of Mt. Pinatubo's volcanic eruption in 1991 initiated weather disturbances on a major global scale for about a year. The solar occultation technique (see Section 7.2.3) has been employed to infer the extinction properties for Mt. Pinatubo aerosols in the stratosphere. Sato *et al.* (1993) estimated the visible optical depth of volcanic aerosols and showed that the global mean value associated with the Mt. Pinatubo eruption is about 0.1, which could produce a negative radiative forcing of about  $-3$  to  $-4 \text{ W m}^{-2}$ . Volcanic activity could be important in interpreting some of the interdecadal variation in surface temperature.

Tropospheric aerosols are produced by both natural and anthropogenic processes. Tropospheric aerosols undergo chemical and physical transformation, particularly in clouds, and are removed primarily by precipitation. They have typical residence times of a few days. As a result of their short lifetime, aerosols in the lower troposphere are distributed inhomogeneously with a maximum concentration close to their source

regions, such as deserts, and industrial and biomass combustion areas. Most aerosols with anthropogenic sources are found in the lower troposphere, below about 2 km. Radiative forcing by anthropogenic aerosols has been recognized as an important contributor to climate change. Anthropogenic sulfate aerosols have been shown to have a direct negative forcing because of their solar reflecting properties. Carbonaceous aerosols are also mainly anthropogenic and are composed of two components: black carbon and organic carbon. Organic carbon from anthropogenic activities is similar to sulfate aerosols in terms of its scattering properties. However, black carbon absorbs significant solar radiation and increases the amount of radiation absorbed by the atmosphere. The presence of black carbon in aerosols may lead to a net heating of the atmosphere. Because of the regional character of sulfate and carbonaceous aerosols, a global model is required to investigate their overall radiative and climatic impact. This subject will be further elaborated upon in Section 8.6.3.

As presented here, the possible response of the global mean temperature field to an increase in aerosol concentrations is far more difficult to estimate than in the cases of changes in  $\text{CO}_2$  concentration and the solar constant for the following reasons. First, the optical properties of various aerosol species in terms of the real and imaginary parts of the refractive index, with respect to wavelength, have not been quantified completely. Second, unlike the increase of  $\text{CO}_2$ , which appears to be uniform around the globe, increases in atmospheric aerosols are likely to be regional. Third, there are questions concerning particle shape and particle size distribution as a function of altitude.

Despite all of these uncertainties, one-dimensional radiative-convective climate models have been used to clarify our understanding of how the perturbation caused by a specific aerosol might influence the radiation field of the earth-atmosphere system and its temperature structure. Charlock and Sellers (1980) have carried out a comprehensive study of the effects of aerosols on temperature perturbation using a one-dimensional climate model. Aerosol optical depth and single-scattering albedo in the visible are used as the two basic parameters in the perturbation studies. The former parameter is an indicator of the attenuation power of aerosols, while the latter represents their relative strength of scattering and absorption. For aerosols with weak absorption, surface temperature decreases as the optical depth increases because of the domination of backscattering. For aerosols with strong absorption, however, warming could occur as the optical depth increases.

Hansen *et al.* (1978) investigated temperature perturbation due to the increase of volcanic dust caused by the explosive eruption of Mount Agung in Indonesia in 1963 based on a one-dimensional climate model. Results showed that after the Agung eruption, average tropospheric temperatures decreased by a few tenths of a degree within a time scale on the order of about 1 year, in agreement with those observed. This cooling effect is caused by the highly reflective properties of the sulfuric acid composition in volcanic aerosols, which block out solar radiation. As a consequence, their addition tends to decrease the amount of solar flux absorbed by the earth-atmosphere system. Hansen *et al.* (1992) conducted a similar simulation involving the eruption of Mt. Pinatubo in 1991 and showed surface cooling for about a year. The potential global atmospheric and climatic consequences of nuclear war

have also been investigated using the one-dimensional models that were developed to study the effects of volcanic eruption (Turco *et al.*, 1983). Significant hemispherical attenuation of solar radiation and subfreezing land temperatures may result from the fine dust particles produced by high-yield nuclear surface bursts and the smoke from city and forest fires ignited by airbursts, a concept referred to as *nuclear winter theory*.

Perhaps the most significant and uncertain role that aerosols play in climate is through their interactions with clouds, the indirect effect. Some aerosols are effective cloud condensation nuclei, which can affect the droplet size distribution and, hence, the radiative properties of clouds and precipitation processes. In addition, the incursion of stratospheric aerosols into the upper troposphere is also a potential source of alteration in the radiative properties of cirrus clouds. Reducing the uncertainty introduced by the indirect aerosol effects on radiative forcing is an important task in climate studies that requires the successful combination of satellite observations and chemical transport modeling.

#### 8.4.5 Cloud Radiative Forcing

Numerical experiments using one-dimensional climate models have been carried out to aid in the understanding of the role clouds play in climate. The effects of high, middle, and low clouds on the equilibrium temperature assuming 100% cloud cover are shown in Fig. 8.14. Nonblack high clouds often produce a warming effect in the troposphere and low stratosphere due to the combined effects of the transmission of solar fluxes and emission of IR fluxes from the clouds. Middle and low clouds produce a significant cooling in the atmosphere and at the surface due to significant reflection by the clouds. The degree of the warming and cooling that results depends on the radiative properties and positions of the clouds used in the model calculations.

In the calculations, representative low and middle clouds (assumed to be black) have solar albedos of 76.9 and 82.5%, respectively, while high clouds have a solar albedo of 10.5% with a nonblack emissivity of 47.5%. Because optically thin high clouds are largely composed of ice crystals, whereas optically thick middle and low clouds primarily contain water droplets, it appears appropriate to suggest that ice clouds are greenhouse elements and that the presence of water clouds would exert a significant solar albedo effect. Clouds thus exert two competing effects on the radiation field of the earth–atmosphere system. On the one hand, they reflect a significant portion of the incoming solar flux, and on the other, they trap the outgoing thermal IR fluxes emitted from the atmosphere below the clouds and from the surface. The competition between the solar albedo and IR greenhouse effects determines whether the surface will undergo cooling or warming.

##### 8.4.5.1 CLOUD POSITION AND COVER

The first issue concerning the role of clouds in greenhouse perturbations is the possible variation in cloud position and cover. If a formation of high clouds were to rise higher in the atmosphere, there would be a positive feedback because of

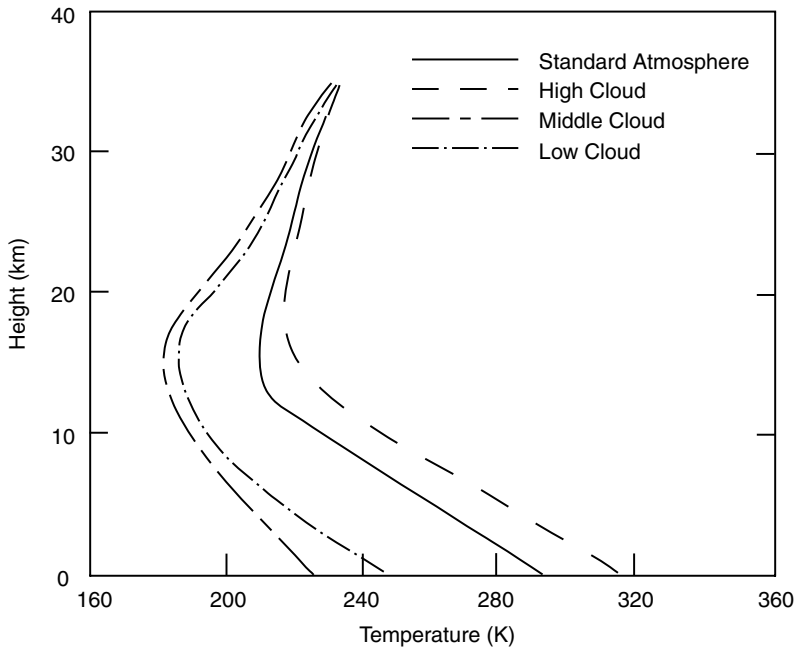


**Figure 8.14** Effects of high, middle, and low clouds on atmospheric temperatures in a radiative-convective model. The solid curve is the temperature profile of the standard atmosphere (data taken from Liou and Ou, 1983).

the enhanced downward IR flux. A positive feedback would also be evident if high cloud cover increased because of greenhouse perturbations. The reverse would be true if middle and low cloud covers increased as a result of greenhouse warming. The prediction of cloud cover and position based on physical principles is a difficult task and its success, even with comprehensive climate models, is limited at this point. This difficulty is also associated with our limited ability to determine cloud cover and cloud position from observations. Because of the uncertainties and limitations of the remote sensing of clouds from satellite radiometers, at this point we do not have sufficient cloud data to correlate with the greenhouse warming that has occurred so far. Section 8.6.2 provides further discussion of this subject.

#### 8.4.5.2 CLOUD MICROPHYSICS

The second factor that determines the role clouds play in global climate and greenhouse warming is related to cloud microphysics in terms of their liquid/ice water content and particle size. Some evidence exists, based on aircraft observations, that an increase in temperature leads to an increase in cloud liquid water content (LWC) (Feigelson, 1981; Matveev, 1984). The temperature dependence of ice water content (IWC) is also evident from aircraft measurements of midlatitude cirrus clouds (Heymsfield and Platt, 1984). Shown in Fig. 8.15 is LWC/IWC as a function of



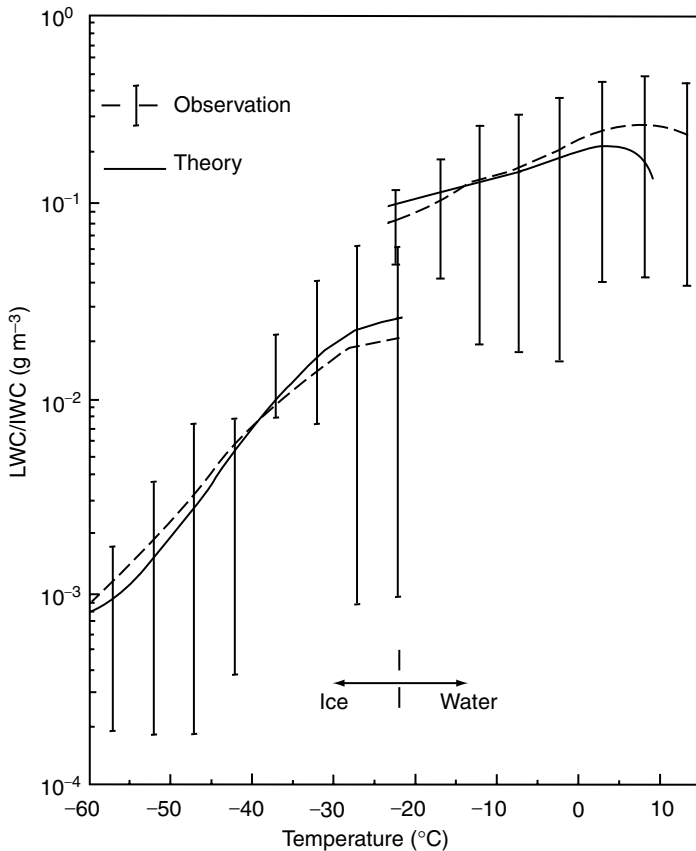


**Figure 8.15** Observed and model computed liquid water content (LWC) and ice water content (IWC) as functions of temperature. The observed LWC and IWC data are based on statistical averages of aircraft measurements presented by Matveev (1984) and Heymsfield and Platt (1984), respectively. Theoretical results are derived from diffusion and accretion models.

temperature from 10°C to -60°C, a range covering the terrestrial atmosphere. Although observed values show large standard deviations, Fig. 8.15 nevertheless reveals the temperature-dependent trend in terms of the mean value, as denoted by the dashed lines. Theoretical results based on diffusion and accretion processes are also illustrated in the diagram for comparison purposes. Based on both the fundamental cloud physics principle and available observations, then, it is clear that as temperature increases, the LWC/IWC of clouds increases as well. On the basis of aircraft microphysics measurements, Heymsfield and Platt (1984) illustrated that there is a distinct correlation between ice-crystal size distribution and temperature. Ice crystals are smaller (larger) at colder (warmer) temperatures. In particular, the colder cloud top primarily contains pristine ice crystals, whereas the warmer cloud bottom is composed of larger irregular ice particles (see Fig. 5.3).

One-dimensional model studies show that if the temperature increases in the region of low clouds, which are composed entirely of water droplets, these clouds will reflect more solar radiation because of greater LWC (the solar albedo effect), leading to a negative feedback (Charlock, 1982; Somerville and Remer, 1984). For high cirrus clouds containing primarily nonspherical ice crystals, a one-dimensional radiative–convective model study illustrates, however, that the balance of solar albedo versus greenhouse effects depends not only on the IWC, but also on the ice crystal size (Ou and Liou, 1995).

The radiative properties of clouds are functions of both the vertical water content and the size spectrum of cloud particles. Because cloud particles scatter an amount of light in proportion to their cross-sectional area, we may define a physical parameter, referred to as the mean effective radius,  $a_e$ , in the case of spherical water droplets, or the mean effective size,  $D_e$ , in the case of nonspherical ice crystals [Eqs. (7.3.13a) and (7.3.15a)]. From the analysis presented in Section 7.3.5, the visible optical depth is then given by [Eqs. (7.3.13d) and (7.3.15c)]

$$\begin{aligned}\tau(\text{water}) &\cong \frac{3}{2\rho_l} \text{LWP}/a_e, \\ \tau(\text{ice}) &\cong \text{IWP}(c + b/D_e),\end{aligned}\tag{8.4.7}$$

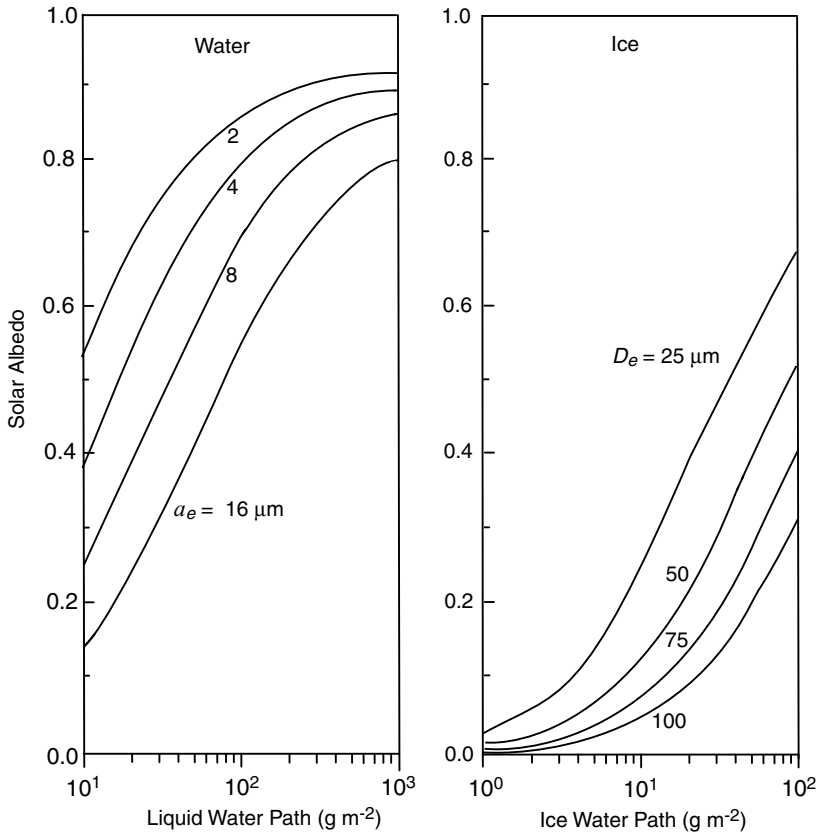
where  $\text{LWP}(\text{IWP}) = \text{LWC}(\text{IWC}) \cdot \Delta z$ , with  $\Delta z$  the cloud thickness. Thus, the optical depth of a cloud is a function of both the LWP (IWP) and mean effective radius (size). For the same LWP or IWP, clouds containing smaller particles would have larger optical depths.

Figure 8.16 shows the cloud albedo covering the solar spectrum (0.2–5  $\mu\text{m}$ ) as a function of LWP/IWP and  $a_e/D_e$  computed from a multiple scattering program (Liou *et al.*, 1998) involving representative spherical water droplets for water clouds and representative hexagonal ice crystals for ice clouds. For a given  $a_e/D_e$ , cloud albedo increases with increasing LWP/IWP. But for a given LWP/IWP, a cloud with a smaller  $a_e/D_e$  reflects more solar radiation because of its larger effective optical depth as noted above. The relationship between cloud albedo and  $a_e/D_e$  is fundamental to the discussion of the indirect aerosol effect in cloud and climate studies.

#### 8.4.5.3 AEROSOLS/CLOUDS AND PRECIPITATION

Cloud cover and LWC are potentially related to precipitation, which is produced by the autoconversion of cloud droplets, where the time constant is proportional to the droplet size distribution. Variations in cloud particle size would affect cloud albedo, but variations in precipitation would affect the washout of cloud condensation nuclei (CCN), a type of aerosol particle, and thus could alter the formation of the cloud particle size spectrum.

Both theory and experiments indicate that the cloud droplet concentration is approximately proportional to the level of CCN, and that the size of the droplets decreases as the CCN in clouds increase. Over land, numerous observations have indicated that pollution increases the number of CCN leading to more small cloud droplets per unit



**Figure 8.16** Broadband solar albedo of water and ice clouds as a function of the liquid water path (LWP)/ice water path (IWP) and the mean effective water droplet radius ( $a_e$ )/ice crystal size ( $D_e$ ). The range of these values covers representative water and ice cloud conditions.

volume (Twomey *et al.*, 1984). This effect has also been observed from the ship stack effluents that modify the radiative properties of shallow stratus clouds over the oceans (Coakley *et al.*, 1987).

The major source of CCN over the oceans is non-sea-salt sulfate, which is produced from the emission of dimethylsulfide (DMS) by marine organisms. The highest rate of DMS emission into the atmosphere is associated with the warmest, most saline, and most intensely illuminated regions of the oceans (Charlson *et al.*, 1987). An increase in the surface temperature associated with greenhouse warming could cause an increase in DMS emission and, hence, in CCN. The consequence of smaller cloud droplets as a result of the additional production of CCN could lead to brighter clouds, an indirect solar albedo effect that is the functional opposite of greenhouse warming.

A one-dimensional cloud-precipitation-climate model has been developed by Liou and Ou (1989) to investigate the potential link between the perturbed cloud particle size distribution produced by greenhouse effects and climate perturbations. If the

perturbed mean cloud particle radii produced by greenhouse effects or air pollution are smaller than the climatological mean value, precipitation could decrease, leading to increases in cloud LWC. Thus, the solar albedo effect would outweigh the infrared greenhouse effect. A reduction of the mean droplet radius by  $0.5\ \mu\text{m}$  could cool the atmosphere to such a degree as to offset the warming produced by  $\text{CO}_2$  doubling. Leaitch *et al.* (1992) observed a reduction in droplet radii of about  $1\ \mu\text{m}$  in eastern North America as a result of anthropogenic pollution.

A number of model studies have shown that more precipitation could be triggered by the warmer temperature fields produced by greenhouse warming. Precipitation is considered to be the primary mechanism for the removal of atmospheric aerosols, including CCN. Thus, the increase in precipitation could cause a reduction in the number of CCN. The low concentration of efficient CCN could, in turn, lead to larger cloud droplets and a reduction of the cloud albedo. It follows that this could provide a possible mechanism for a positive feedback to greenhouse warming. The potential positive feedback associated with particle size in cloud-climate feedback problems was first noted by Liou and Ou (1989) and Albrecht (1989).

The role of clouds in climate and climatic perturbations due to external radiative forcing is indeed intricate and multidimensional. The results derived from one-dimensional models shed some light on the potential interaction and feedback involving cloud height, cloud LWC, and cloud particle size associated with temperature increases produced by greenhouse warming. However, one-dimensional models do not account for horizontal variations in cloud parameters. In view of the fact that clouds are three-dimensional in nature, their role in climate and global climate change must be resolved from models that can simulate both vertical and horizontal cloud structure and composition based on fundamental physical principles. Further discussion of the role of clouds and radiation in climate is presented in Section 8.6.2.

## 8.5 Radiation in Energy Balance Climate Models

In the previous section dealing with the earth's radiation budget, we noted that, on average, there is a radiation excess in the tropical region and a radiation deficit in the middle and high latitudes (Fig. 8.2). Significant temperature and water vapor gradients also occur in the atmosphere near the surface. Thus, there must be poleward as well as upward energy transfers in order to produce an overall energy balance. Energy exchanges at TOA are solely due to radiative processes. However, within the earth-atmosphere system, these exchanges involve a number of mechanisms of which radiative energy transfer is only one component.

### 8.5.1 Energy Budget of the Atmosphere and the Surface

#### 8.5.1.1 ATMOSPHERE AND OCEANS

Based on the energy conservation principle, the zonal mean rate of energy storage per unit area in the atmosphere must be the residual of the net surface flux, the net

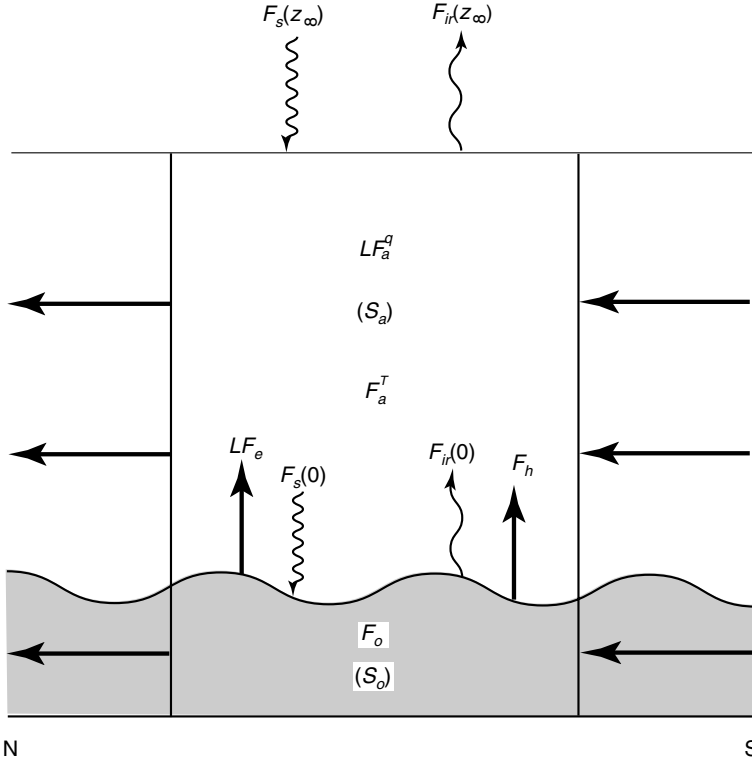


**Figure 8.17** Energy components of the earth and the atmosphere, where  $F_s(z_\infty)$  and  $F_{ir}(z_\infty)$  denote the absorbed solar flux and the emitted IR flux at TOA;  $F_s(0)$  and  $F_{ir}(0)$  are the absorbed solar flux and the emitted IR flux at the surface;  $LF_a^q$  and  $F_a^T$  are the divergence of meridional transports of latent and sensible heat;  $F_o$  is the divergence of oceanic transports of sensible heat;  $LF_e$  and  $F_h$  are the vertical fluxes of latent and sensible heat, respectively; and  $S_a$  and  $S_o$  are the zonal mean rate of energy storage per unit area for the atmosphere and the oceans, respectively.

TOA radiative flux  $F(z_\infty)$ , and the divergence of atmospheric transport of heat  $F_a$ , given by

$$S_a = [F_v(0) + F(0)] - F_a - F(z_\infty), \quad (8.5.1)$$

where  $F_v(0)$  denotes the surface vertical flux associated with the transport of sensible ( $F_h$ ) and latent heat ( $LF_e$ ) fluxes [see Eq. (8.5.5)]. The atmospheric transport term also consists of two terms involving sensible ( $F_a^T$ ) and latent heat ( $LF_a^q$ ) components. Equation (8.5.1) is the basic energy balance equation for an atmospheric column in which the total heat storage rate is balanced by the surface input minus the sum of the divergence of the poleward transport of heat and the net radiative flux at TOA, as displayed in Fig. 8.17. The net radiative flux is the difference between the absorbed solar flux  $F_s$  and the emitted IR flux  $F_{ir}$ .

At the surface, the energy balance is governed by the rate of energy storage, the net surface flux, and the divergence of the transport of sensible heat below the earth's surface. The heat capacity of the continental surface is generally very small, as in the cases of snow and ice. Thus, on a large scale, the principal heat exchange must occur between the atmosphere and the oceans. Analogous to Eq. (8.5.1) for atmospheric storage, the zonal mean rate of energy storage per unit area for the oceans may be expressed by

$$S_o = -[F_v(0) + F(0)] - F_o, \quad (8.5.2)$$

where the first term represents the net surface flux between the radiative and turbulent fluxes and  $F_o$  is the divergence of the oceanic transport of sensible heat. The zonal mean rate of energy storage per unit area in the atmosphere varies with the seasons from 10 to 20 W m<sup>-2</sup>, but the annual mean value is about zero. For the oceans, seasonal variations can be as large as 100 W m<sup>-2</sup>.

The divergence of the atmospheric transport of sensible and latent heat is shown in Fig. 8.18a. Positive and negative values represent the divergence and convergence of heat, respectively. The atmospheric latent heat component has a minimum between about 10°N and 10°S because of excess precipitation in the tropical convective zone. Minima between about 40° and 60° in both hemispheres are a result of the surplus precipitation produced by cyclonic storm activity. Maxima patterns are evident in the subtropics between about 20° and 30° in both hemispheres, where evaporation rates are highest. In the northern subtropics evaporation is less pronounced because of the presence of large desert areas. The atmospheric sensible heat component shows a large maximum in the tropics associated with higher temperatures and Hadley circulation. Small maxima at 40°N and S are related to the transport of heat by eddies and mean meridional circulation. On an annual basis, about 20 W m<sup>-2</sup> of sensible and latent heat is lost between 40°S and 40°N, while about 50 to 70 W m<sup>-2</sup> is gained poleward of 60°. In the middle and high latitudes, sensible and latent heat is largely transported by transient eddies. The mean circulation contribution to heat transport is most pronounced in the tropics. For annual mean conditions, the divergence of the oceanic transport of sensible heat may be estimated from Eq. (8.5.1) as a residual, if the atmospheric heat storage, the atmospheric divergence of sensible and latent heat, and the net radiative flux at TOA are given. About 40 W m<sup>-2</sup> of heat is transported by ocean currents out of the tropics, and about 25 W m<sup>-2</sup> of heat is transported by ocean currents into latitudes poleward of 40°. Since there are no oceans south of about 70°S, the energy convergence of heat in the oceans should disappear there. Finally, the sum of the divergence of atmospheric and oceanic transports of heat must be balanced by the net radiative flux at TOA on an annual basis (see also Fig. 8.2).

To obtain the total horizontal flux (energy/time) for the entire atmosphere for each component displayed in Fig. 8.18a, we may perform an integration of the horizontal flux  $F_h$  over the latitudinal cross section to obtain

$$f_a = 2\pi a_e \cos \varphi \int_0^{z_\infty} F_h dz, \quad (8.5.3a)$$

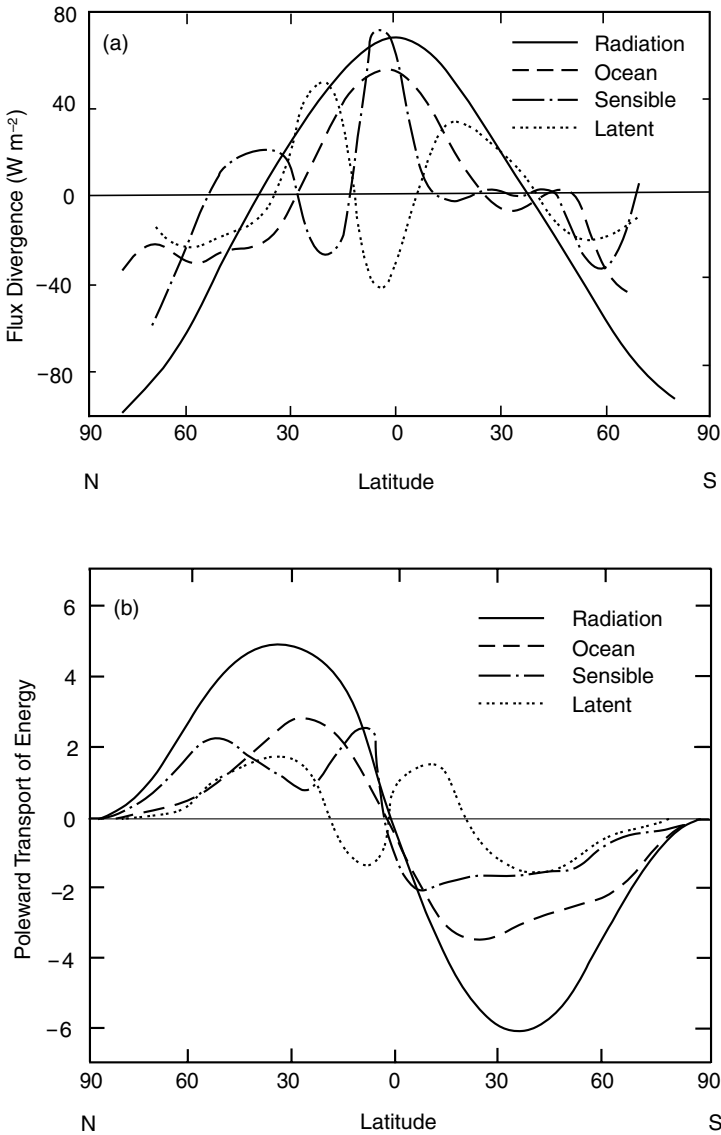


**Figure 8.18** (a) Divergence of atmospheric transports of sensible and latent heat, and oceanic transports of sensible heat. Also shown is the net radiative flux density at TOA. (b) Meridional profiles of the poleward transports of sensible and latent heat in the atmosphere, and of sensible heat in the oceans. Also shown is the net radiative flux. All the terms are in units of  $10^{15}$  W (data taken from Oort and Peixóto, 1983).

where  $a_e$  is the radius of the earth and  $\varphi$  is the latitude. Figure 8.18b shows the meridional profiles of the poleward transports of sensible and latent heat in the atmosphere, the poleward transport of sensible heat in the oceans, and the net radiative flux (energy/time) at TOA. The oceanic transports dominate in low latitudes with maximum poleward transports of about  $3 \times 10^{15}$  W near  $25^\circ\text{N}$  and about  $-3.5 \times 10^{15}$  W near  $20^\circ\text{S}$ . Latent heat is transported both toward the equator and toward the poles from about  $20^\circ\text{N}$  and S, where the evaporation maxima are located. The transports of sensible heat in the atmosphere show double maxima at about  $10^\circ$  and  $50^\circ$  in both hemispheres with values of about  $2 \times 10^{15}$  W. In lower latitudes between  $20^\circ\text{N}$  and  $20^\circ\text{S}$ , the atmospheric transports of sensible and latent heat largely cancel each other out. As a result, the total atmospheric transport of energy is more important in the middle and high latitudes.

#### 8.5.1.2 SURFACE ENERGY BUDGET

The net surface flux defined in Eq. (8.5.1) consists of the vertical flux and the net radiative flux, which can be divided into its solar and IR components. A large fraction of the solar flux at TOA is transmitted through the clear atmosphere, as is evident in Fig. 3.9. In cloudy conditions, the solar flux available at the surface is largely dependent on the solar zenith angle and cloud optical depth, which is a function of cloud liquid/ice water content and particle size distribution, as illustrated in Fig. 3.19. In reference to Eq. (8.2.30), let the absorbed portion of the solar flux be denoted by

$$F_s(0) = F_s^\downarrow(0)(1 - r_s). \quad (8.5.3b)$$

The net IR flux at the surface is the difference between the upward IR flux emitted by the surface and the downward IR flux from the atmosphere reaching the surface  $F_{ir}^\downarrow(0)$ . We may then let the net emitted IR flux be denoted by

$$F_{ir}(0) = \varepsilon_s \sigma T_s^4 - \varepsilon_s F_{ir}^\downarrow(0). \quad (8.5.4)$$

The vertical transport of energy from the surface to the atmosphere consists of the flux of sensible heat from the surface  $F_h$  and the evaporative water loss from the surface  $F_e$ . Thus, we write

$$F_v(0) = LF_e + F_h, \quad (8.5.5)$$

where  $L$  is the coefficient for the latent heat of evaporation.

On the basis of the energy conservation principle, the net flux of energy absorbed by the surface must equal the rate at which the surface is storing energy  $S_s$ , so that

$$\begin{aligned} S_s &= F_s(0) - F_{ir}(0) - F_v(0) \\ &= F_s^\downarrow(0)(1 - r_s) - \varepsilon_s \sigma T_s^4 + \varepsilon_s F_{ir}^\downarrow(0) - LF_e - F_h. \end{aligned} \quad (8.5.6)$$

Over the oceans, we have  $S_s = S_o + F_o$ , from Eq. (8.5.2). Over land and on a microscopic scale,  $S_s$  may be expressed in terms of the rate of heat conduction into the underlying surface. Equation (8.5.6) represents the basic surface energy equation.



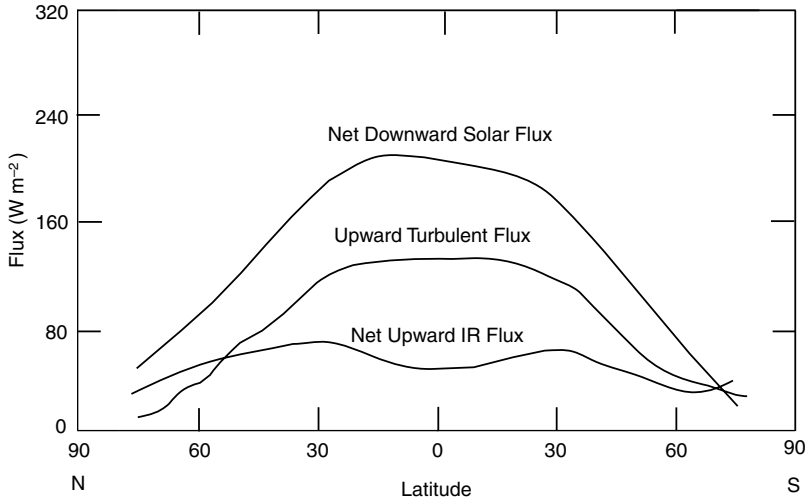


**Figure 8.19** Latitudinal distributions of estimated mean annual net solar flux, net IR flux, and total turbulent flux at the earth's surface (data taken from Ou *et al.*, 1989; Budyko, 1982; Sellers, 1965).

Local variations such as the melting of snow and ice have not been considered here. The assumption that  $S_s = 0$  has been frequently used in weather prediction and climate models because of its simplicity. This assumption is approximately correct for land surfaces, averaged over 24 hours, but would lead to large errors in determining surface temperature over a diurnal cycle. If  $S_s = 0$ , surface temperature can be directly computed from Eq. (8.5.6), provided that all the radiative and turbulent fluxes are known.

The surface albedo is dependent on the type of surface, as well as on the solar zenith angle and the wavelength. For water surfaces, the albedo generally ranges from 6 to 9%. The albedo varies significantly over land surfaces with values ranging from 10 to 40%. The albedos of snow and ice are usually greater than about 40%. The dependence of vegetation albedo on solar wavelength is significant (see Fig. 7.7). The thermal IR emissivities of water and land surfaces are normally between 90 and 95%. It is usually assumed that the earth's surfaces are approximately black in infrared radiative transfer calculations. Exceptions include snow and some sand surfaces whose emissivities are wavelength dependent and could be less than 90%. The transport of sensible heat and water vapor from surfaces is governed by turbulent motion and is generally expressed by the vertical gradients of temperature and specific humidity near the surface based on the mixing length theory (Brutsaert, 1982).

Latitudinal distributions of annual net solar and IR fluxes and the total turbulent flux at the earth's surface are displayed in Fig. 8.19. The annual net surface solar flux decreases poleward, resulting in a slight hemispheric asymmetry. Latitudinal distributions of annual net surface IR flux show double maxima at about  $35^\circ$  in both hemispheres; these maxima are associated with subtropical highs. The minimum

pattern in the tropics is due to the large downward IR fluxes produced by the extensive cloud cover in the ITCZ. This pattern is similar to the dip that occurs in the emitted IR flux at TOA. Estimates of the vertical turbulent fluxes of sensible and latent heat can be made by using available climatological data, as shown in Fig. 8.19. The surface turbulent flux decreases from about 100–150 W m<sup>-2</sup> in the tropics to near zero at the poles. There is a large amount of uncertainty in the estimate of vertical flux in the tropics. A large fraction of the vertical transport takes place through cumulus convection, which occurs in only about 3–4% of the total tropical area. For this reason, it is very difficult to quantify vertical transport based on data obtained from a limited number of observational points. On an annual basis, the sum of the turbulent flux and the net IR flux at the surface is approximately equal to the solar flux absorbed by the surface.

### 8.5.2 Radiative Forcing in Energy Balance Climate Models

The zonal mean rates of energy storage per unit area in the atmosphere and the oceans may be related to the local time rate of change of surface temperature, as a first approximation, in the form

$$S_a + S_o = c(\varphi) \frac{\partial T}{\partial t}, \quad (8.5.7)$$

where the surface temperature is denoted by  $T$  in this section,  $c$  is referred to as the *thermal inertia coefficient*, and  $\varphi$  is the latitude. On eliminating the net surface flux from Eqs. (8.5.1) and (8.5.2) and letting the total atmospheric and oceanic transports of energy be

$$R = F_a + F_o, \quad (8.5.8)$$

we have

$$-c(x) \frac{\partial T(t, x)}{\partial t} = -[F_s(t, x) - F_{ir}(t, x)] + R(t, x), \quad (8.5.9)$$

where  $x = \sin \varphi$ . This is the basic equation for the one-dimensional energy balance climate model. To seek a solution for surface temperature, it is necessary to relate both the infrared and horizontal fluxes to surface temperature and to express the absorbed solar flux as a function of surface albedo.

We may approach the determination of the equilibrium surface temperature using the steady-state condition to obtain

$$F_s(x) = F_{ir}(x) + R(x). \quad (8.5.10)$$

In an infinitesimal latitude belt under equilibrium, the absorbed solar flux must be balanced by the emitted infrared flux and the net horizontal flux divergence, including sensible and latent heat transports by atmospheric motions and sensible heat transports by ocean currents (see Fig. 8.18). In the following, we present two approaches for the evaluation of surface temperature associated with solar constant perturbations.

### 8.5.2.1 LINEAR HEATING APPROACH

On the basis of the monthly mean values of radiation flux density at the top of the atmosphere for 260 stations, Budyko (1969) developed an empirical formula relating the outgoing infrared flux density, the surface temperature, and the fractional cloud cover in the form

$$F_{ir}(x) = a_1 + b_1 T(x) - [a_2 + b_2 T(x)]\eta, \quad (8.5.11)$$

where, for simplicity, the surface temperature  $T_s$  is set as  $T$ , as noted above,  $\eta$  is the fractional cloud cover, and  $a_1$ ,  $b_1$ ,  $a_2$ , and  $b_2$  are empirical constants. The influence of the deviation of cloudiness from its mean global value on the temperature is normally neglected because of the intricate relation of clouds with the radiation field and surface albedo. With a fractional cloud cover  $\eta$  of 0.5, Eq. (8.5.11) may be rewritten in the form

$$F_{ir}(x) = a + bT(x), \quad (8.5.12)$$

where the coefficients  $a$  and  $b$  are defined in Eq. (8.4.5). As pointed out in Section 8.4.3, the physical explanation of the linear relation between the outgoing infrared flux and the surface temperature is that, since the temperature profiles have more or less the same shape at all latitudes, infrared cooling, which depends on the temperature at all levels, may be expressed in terms of the surface temperature.

The incoming solar flux density may be expressed by

$$F_s(x) = Qs(x)[1 - r(x)] = Qs(x)A(x), \quad (8.5.13)$$

where  $Q = S/4$ ,  $S$  is the solar constant,  $r$  is the planetary albedo, which is allowed to vary in terms of temperature,  $A$  is the solar flux absorbed by the earth-atmosphere system, and  $s(x)$  is the normalized mean annual distribution of insolation at each latitude.  $Qs(x)$  can be obtained from the values presented in Fig. 2.8.

Moreover, to relate the surface temperature distribution and the horizontal heat transfer in the atmosphere and hydrosphere, Budyko derived a simple linear equation by comparing the observed mean latitudinal values of  $R(x)$  with the difference of the annual mean temperature at a given latitude and the global mean temperature  $\bar{T}$ , given by

$$R(x) = c[T(x) - \bar{T}], \quad (8.5.14)$$

with the empirical constant  $c \cong 3.75 \text{ W m}^{-2} \text{ C}^{-1}$ .

Substituting Eqs. (8.5.12)–(8.5.13) into Eq. (8.5.10) leads to

$$Qs(x)A(x) - [a + bT(x)] = c[T(x) - \bar{T}]. \quad (8.5.15a)$$

The surface temperature is then given by

$$T(x) = \frac{Qs(x)A(x) - a + c\bar{T}}{c + b}. \quad (8.5.15b)$$

Furthermore, over a climatological time scale, the earth–atmosphere system as a whole should be in radiative equilibrium so that

$$Q\bar{A} - (a + b\bar{T}) = 0, \quad (8.5.16)$$

where the global surface temperature, global absorptivity, and global albedo are defined by

$$\bar{T} = \int_0^1 T(x) dx, \quad \bar{A} = 1 - \bar{r} = \int_0^1 s(x)A(x) dx. \quad (8.5.17a)$$

Consequently,

$$\bar{T} = (Q\bar{A} - a)/b. \quad (8.5.17b)$$

At this point, the latitudinally dependent surface temperature may be computed as a function of  $x$  for given  $s(x)$  and  $A(x)$ . The planetary albedo is usually defined by a simple step function depending on whether or not an ice sheet exists. By letting  $x_i$  represent the sine of latitude  $\varphi_i$  of the ice line, the absorptivity or albedo can be expressed by (Budyko, 1969; Sellers, 1969)

$$A(x, x_i) = 1 - r(x, x_i) = \begin{cases} A_1, & x > x_i \\ A_2, & x < x_i. \end{cases} \quad (8.5.18)$$

Exercise 8.5 requires computation of the temperature as a function of  $x$ .

To study the model's sensitivity to solar constant perturbations, a linear analysis of the global surface temperature, solar constant, and global albedo may be carried out by setting  $\bar{T} = \bar{T}_0 + \Delta\bar{T}$ ,  $Q = Q_0 + \Delta Q$ , and  $\bar{r} = \bar{r}_0 + \Delta\bar{r}$ , where  $\bar{T}_0$ ,  $Q_0$ , and  $\bar{r}_0$  denote the mean values for the present climate condition. It follows that

$$\begin{aligned} T(x) = \frac{1}{c+b} & \left\{ Q_0 s(x) [1 - r(x)] \left( 1 + \frac{\Delta Q}{Q_0} \right) - a + c\bar{T}_0 \right. \\ & \left. + \frac{cQ_0}{b} \left[ \frac{\Delta Q}{Q_0} (1 - \bar{r}_0 - \Delta\bar{r}) - \Delta\bar{r} \right] \right\}. \end{aligned} \quad (8.5.19)$$

Thus, the effects of a change in the solar constant on the earth's mean annual surface temperature can be investigated in a manner that includes the coupling effect of the changing global albedo, an indication of the change in a glaciated area. In his original work, Budyko expressed  $\Delta\bar{r}$  in terms of an empirical function in the form  $0.3l(x, \bar{x}_i)s^*(x_i)$ , where  $\bar{x}_i (= 0.95)$  represents the present ice-line position,  $l$  is the ratio of the change in the ice-covered area to the total area of the northern hemisphere, and  $s^*$  is the ratio of the mean solar flux in the zone of the additional ice area to the mean solar flux for the entire hemisphere.

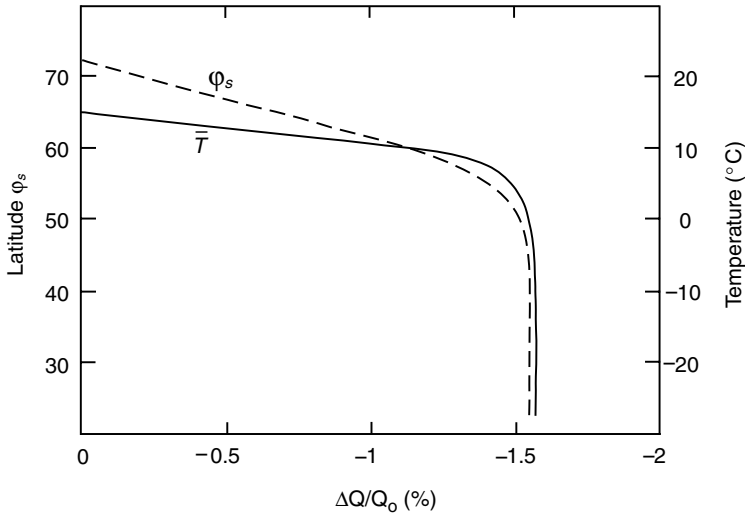


**Figure 8.20** Dependence of the global surface temperature and the latitude of glaciation on changes in the solar constant (data taken from Budyko, 1969). If this change is reduced by about 1.6%, the ice line reaches a latitude of about 50°N and advances southward to the equator without any further reduction in the solar constant. This is referred to as Budyko’s theory of the runaway ice-covered earth, due to the ice–albedo feedback. Additional theoretical calculations show that a substantial decrease in the solar constant on the order of 10% is required to cause an ice-covered earth.

Using Eq. (8.5.19), calculations can be carried out to investigate the position of the ice line for different values of  $\Delta Q/Q_0$ . Shown in Fig. 8.20 are the latitude  $\phi_s$ , corresponding to the ice-line position, and the global temperature  $\bar{T}$  as functions of  $\Delta Q/Q_0$ . In these calculations, the mean value for the solar constant used was  $1353 \text{ W m}^{-2}$ , and the global albedo was set at 0.33. Based on climatological data, the ice-line temperature  $T(x_i)$  was assumed to be  $-10^{\circ}\text{C}$ . The step functions for absorptivity were  $A_1 = 0.38$ ,  $A_2 = 0.68$ , and  $A_{12} = 0.5$  at the ice line. With a 1% decrease in the incoming solar flux, the global surface temperature is reduced by about  $5^{\circ}\text{C}$ . Further, a 1.5% decrease in the incoming solar flux reduces the global surface temperature by about  $9^{\circ}\text{C}$ . The response to these decreases in temperature is a southward advance of glaciation by about  $18^{\circ}$  of latitude, corresponding to the advance of quarternary glaciation. Based on these calculations, when  $\Delta Q/Q_0$  is reduced by about 1.6%, the ice line reaches a latitude of about 50°N, at which point the global surface temperature decreases to several tens of degrees below zero. As a result, the ice sheet begins to advance continuously southward to the equator with no further reduction in the solar flux required. Note that with a constant global mean albedo (i.e.,  $\Delta\bar{\alpha} = 0$ ), a 1% decrease in  $\Delta Q/Q_0$  lowers the global surface temperature by only 1.2–1.5°C. The significance of the ice–albedo coupling effect is quite apparent. The preceding process describes Budyko’s theory of the runaway ice-covered earth, which is based on the ice–albedo feedback. A decrease in the solar constant produces surface cooling, which leads to an increase in the ice-covered area. In

turn, the surface albedo increases, resulting in a reduction in the absorption of solar flux.

### 8.5.2.2 DIFFUSION APPROACH

A more rigorous approach to parameterizing horizontal heat transport can be constructed by utilizing the diffusion concept in a large-scale sense. From Eq. (8.5.8), we have

$$R = LF_a^q + F_a^T + F_o = F_s - F_{ir}. \quad (8.5.20)$$

The three large-scale transport terms may be expressed by a linear function of surface temperature differences in terms of a second-order equation in  $\Delta T$ .

The second-order equation in  $\Delta T$  for horizontal heat transport is, in essence, the diffusion approximation (Held and Suarez, 1974; North, 1975; Ghil, 1976). A thermal diffusion form for horizontal heat transport,  $-D\nabla^2 T$ , was adopted with  $D$  being an empirical coefficient to be determined by fitting the present climate. Thus, all the transport processes are parameterized with a single coefficient, analogous to an eddy diffusion approach to dispersion by macroturbulence in the entire geofluid system. Using the spherical coordinates for the Laplace operator [see Eq. (5.2.29)] in the context of a one-dimensional latitudinal variation, we have

$$-D\nabla^2 T = \frac{-D}{a_e^2 \sin \theta} \frac{d}{d\theta} \left( \sin \theta \frac{dT}{d\theta} \right) = \frac{-D}{a_e^2} \frac{d}{dx} (1 - x^2) \frac{dT}{dx}, \quad (8.5.21)$$

where the polar angle  $\theta = 90^\circ - \varphi$  and  $a_e$  is the radius of the earth. Letting  $D' = D/a_e^2$ , we find from Eq. (8.5.10) that

$$D' \frac{d}{dx} (1 - x^2) \frac{dT}{dx} = F_{ir}(x) - Qs(x)A(x, x_i). \quad (8.5.22)$$

Since  $F_{ir}$  and  $T$  are linearly related through Eq. (8.5.12), we may rewrite Eq. (8.5.22) in the form

$$\left[ \frac{d}{dx} (1 - x^2) \frac{d}{dx} - \frac{1}{D''} \right] F(x) = \frac{Q}{D''} s(x) A(x, x_i), \quad (8.5.23)$$

with  $D'' = D'/b$ , and we let  $F_{ir} = F$  for the convenience of presentation. We must now specify the ice-sheet edge  $x_i$ . It is generally assumed that if  $T(x) < T_i$ , ice will be present, whereas if  $T(x) > T_i$ , there will be no ice. In terms of infrared flux, we may set  $F(x_i) = F_i$ . As noted previously, the ice-line temperature  $T_i$  is normally assumed to be  $-10^\circ\text{C}$ .

For a mean annual model with symmetric hemispheres, the boundary condition must be that there is no heat flux transport at the poles or across the equator, i.e.,  $\nabla F(x)$  or  $\nabla T(x) = 0$  at  $x = 1$  and  $0$ , respectively. Thus,

$$(1 - x^2)^{1/2} \frac{d}{dx} F(x) \Big|_{x=0} = (1 - x^2)^{1/2} \frac{d}{dx} F(x) \Big|_{x=1} = 0. \quad (8.5.24)$$

To obtain a solution we may expand  $F(x)$  in terms of the Legendre polynomials in the form

$$F(x) = \sum_{n=\text{even}} F_n P_n(x), \quad (8.5.25)$$

where only even terms are used because  $F(x)$  is an even function of  $x$  in the mean annual case, i.e., symmetric between two hemispheres, and  $F_n$  represent the unknown coefficients to be determined. Since the Legendre polynomials are the eigenfunctions of the spherical diffusion equation, defined in Eq. (5.2.42) (for  $\ell = 0$ ), we have

$$\frac{d}{dx}(1-x^2)\frac{d}{dx}P_n(x) = -n(n+1)P_n(x). \quad (8.5.26)$$

Moreover,  $(1-x^2)^{1/2}dP_n(x)/dx = 0$  for  $x = 0$ , and 1 when  $n = \text{even}$ . It follows that the imposed boundary conditions described in Eq. (8.5.24) are satisfied by the expansion.

Substituting Eq. (8.5.25) into Eq. (8.5.23) and utilizing the orthogonal property of  $P_n$  (see Appendix E), we find

$$F_n = Q H_n(x_i) / [1 + n(n+1)D''], \quad (8.5.27a)$$

where

$$H_n(x_i) = (2n+1) \int_0^1 s(x) A(x, x_i) P_n(x) dx, \quad (8.5.27b)$$

which can be evaluated from the known values for  $s(x)$  and  $A(x, x_i)$ . The final step in completing the solution is to determine the diffusion transport coefficient  $D''$ . This can be done empirically by varying  $D''$  in Eq. (8.5.27a) to satisfy the present climate conditions, i.e.,  $\bar{x}_i = 0.95$ ,  $F(\bar{x}_i) = F_i$ , and  $Q = Q(\bar{x}_i) = Q_0$ . The solution can then be used to investigate the ice-line position as a function of  $Q$ . Using Eqs. (8.5.25) and (8.5.27a) and letting  $x = x_i$ , we obtain

$$Q(x_i) = F_i \left[ \sum_{n=\text{even}} \frac{H_n(x_i) P_n(x_i)}{1 + n(n+1)D''} \right]^{-1}. \quad (8.5.28)$$

The normalized mean annual distribution of insolation  $s(x)$  can be fitted by Legendre polynomial expansions. With a degree of accuracy of about 2%, it is given by

$$s(x) = \sum_{n=\text{even}} s_n P_n(x) \approx 1 + s_2 P_2(x), \quad (8.5.29)$$

where  $s_2 = 0.482$ . Based on observed data, the absorptivity of ice-free latitudes may also be fitted by Legendre polynomial expansions in the form

$$A_2(x, x_s) = d_0 + d_2 P_2(x), \quad x < x_s, \quad (8.5.30)$$

with  $d_0 = 0.697$  and  $d_2 = -0.0779$ . The absorptivity over ice or snow with 50% cloud cover is assumed to be 0.38 as defined previously.

The results derived from the preceding diffusion model show the multiple branch nature of the solution. A southward advance of glaciation requires a decrease in the solar constant of about 8 to 9% (North, 1975). After the ice line reaches  $\sim 45\text{--}50^\circ\text{N}$ , its southward advance continues even though the incoming solar flux increases. This result is basically in agreement with Budyko's theory, although the decrease in the solar constant that is needed to produce an ice-covered earth is substantially greater. Finally, it is noted that the diffusion models with nonlinear coefficients, such that  $D$  is proportional to  $dT/dx$ , produce virtually the same results and conclusions (Held and Suarez, 1974; North *et al.*, 1981).

The simple climate models just described are not in reasonable agreement with the nearly isothermal surface temperatures observed within  $30^\circ$  of the equator, as argued by Lindzen and Farrell (1977). To introduce tropical transport, referred to as Hadley cell transport, into simple climate models, they introduced an empirical adjustment to include a heat-flux term. This heat flux approached zero for latitudes greater than a prescribed latitude  $\varphi_h$  ( $\sim 25^\circ\text{N}$ ). For Budyko's linear heating model,  $Q_s(x)A(x, x_i)$  was replaced by its average over the region  $0 \leq \varphi \leq \varphi_h$ . Lindzen and Farrell's model showed that at  $25^\circ$  latitude, identified as the Hadley stability ledge, a reduction in the solar constant did not significantly alter the ice-line position. It was not until the solar constant reduction reached about 15 to 20% that the glaciation advanced continuously southward. From  $25^\circ$  to about  $60^\circ$ , identified as the moderately strong stability region, a southward advance of glaciation was related to the decrease of the solar constant. This model illustrated that the reduction in the solar constant necessary for an ice-covered earth is much greater than Budyko's predicted value of 1.6%.

### 8.5.3 Solar Insolation Perturbation

A number of external factors have been proposed as the major causes of the earth's climatic variations during the Pleistocene period, about 600,000 years ago. This period is the first epoch of the Quaternary period in the Cenozoic era, characterized by the spreading and recession of continental ice sheets and by the appearance of the modern human. Variations in the output of the sun, seasonal and latitudinal distributions of incoming solar radiation due to the earth's orbital changes, the volcanic dust content of the atmosphere, and the distribution of carbon dioxide between the atmosphere and the oceans have all been hypothesized to have caused the fluctuations of the great ice sheets that were characteristic of this period. The orbital theory of climate change originally described by Milankovitch (1941) appears to receive considerable support based on climatological and geological records. In Section 2.2, we detailed the variation in solar insolation as a function of the earth's orbital parameters: eccentricity, oblique angle, and the longitude of the perihelion (precession).

Based on measurements of the oxygen isotopic composition of planktonic foraminifera from deep-sea sediment cores taken in the southern Indian Ocean, Hays *et al.* (1976) have reconstructed the climatic record of the earth up to  $\sim 500,000$  years ago. Summer sea-surface temperatures at the core site have been estimated based on statistical analyses of radiolarian assemblages. Spectral analyses of paleoclimatic



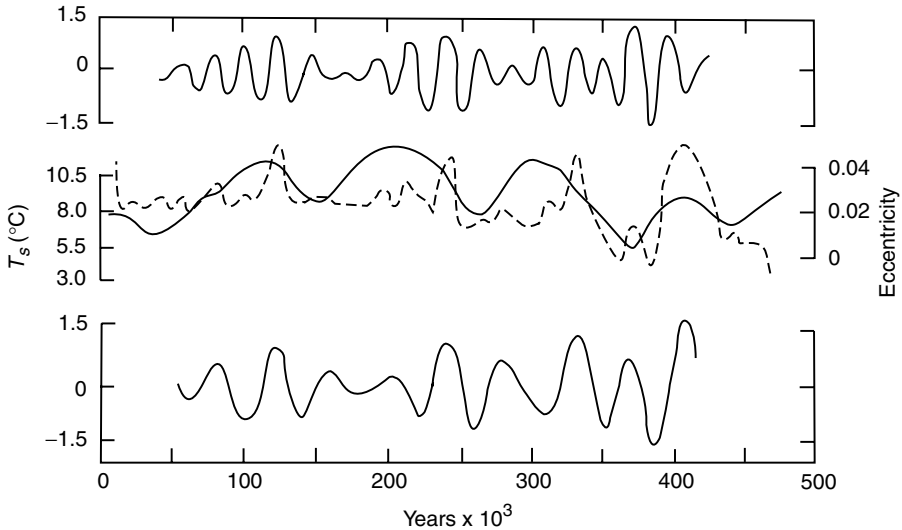


**Figure 8.21** Variation in eccentricity and surface temperature over the past 500,000 years. Dashed line in the center shows variations in the estimated sea surface temperature  $T_s$ . Solid line denotes the orbital eccentricity. Upper and lower curves are the 23,000- and 40,000-year frequency components extracted from  $T_s$  based on a statistical filter method (data taken from Hays *et al.*, 1976).

time series indicate significant peaks in the frequencies at which the earth's orbital parameters are known to vary. These observations are of fundamental importance to our understanding of climatic sensitivity. Figure 8.21 shows that the principal periods of climatic variation ( $\sim 100,000$ ,  $42,000$ , and  $23,000$  years) correspond to periods of orbital changes in eccentricity ( $\sim 105,000$  years), obliquity ( $\sim 41,000$  years) and precession ( $\sim 23,000$  and  $19,000$  years).

Down-core variations in  $\delta^{18}\text{O}$  reflect changes in oceanic isotopic composition, which are considered to be caused primarily by the waxing and waning of the great Pleistocene ice sheets. Measurements of the ratio of  $^{18}\text{O}$  and  $^{16}\text{O}$  have been reported with respect to an international standard as  $\delta^{18}\text{O}$  in parts per thousand. Employing observations of  $\delta^{18}\text{O}$  in five deep-sea cores, Imbrie *et al.* (1984) have developed a geological time series for the past 780,000 years to evaluate the orbital theory of the Pleistocene ice ages and found that the orbital and isotopic signals are strikingly coherent in the 41,000- and 22,000-year components.

One-dimensional energy balance climate models have been used in an attempt to explain glacial cycles in terms of solar insolation changes associated with the earth's orbit. The fractional changes of mean annual global insolation are approximately given by  $\Delta e^2/2$ , as defined in Eq. (2.2.26). Since the eccentricity is less than about 0.07, the resulting changes in solar insolation are less than  $\sim 0.2\%$ , which corresponds to a change of about  $0.4^\circ\text{C}$  in the global mean surface temperature based on a one-dimensional energy balance model (North *et al.*, 1981). This change in surface temperature is an order of magnitude smaller than the changes reported by Hays *et al.*

(1976), cited earlier. It has been speculated that the glacial maximum of 18,000 years ago was due to a variation in the declination of the sun from about  $22.2^\circ$  to its present value of  $23.45^\circ$ . This change resulted in less insolation at the poles and more at the equator. Based on the annual energy balance model, this obliquity change causes only a  $1\text{--}2^\circ$  equatorward shift in the ice line, much smaller than the approximately  $15^\circ$  shift reconstructed by the CLIMAP Project Members (1976).

The small responses of the annual energy-balance climate model to orbital parameters have led to the suggestion that seasonal variations must be incorporated in the model to produce more accurate orbital solar forcings. Suarez and Held (1979) have developed a seasonal energy balance model to investigate orbital forcings. Significant discrepancies, however, exist between the model's present climate and the actual record. Moreover, the response of the surface temperature to orbital parameters in the model is fairly linear and cannot be used to explain the strong surface-temperature variations that are present in the spectral analyses of the paleoclimatic record over the last 100,000 years. Although physical factors such as oceanic heat transports, variations in cloudiness, and atmospheric transports of sensible and latent heat could be accounted for more comprehensively in one- or two-dimensional energy-balance climate models, it is not evident that such simplified models, with their inherent limitations, would be physically adequate to successfully reproduce the paleoclimatic record. However, through the use of global climate models, some success has been achieved in understanding how past glacial climates were maintained and in estimating the relative significance of the known feedback mechanisms involving the changes in ice sheets, land albedo, and atmospheric  $\text{CO}_2$  in forcing the temperature changes that existed 18,000 years ago (Broccoli and Manabe, 1987). Simulations of paleoclimate records require an efficient physically based global model that couples the atmosphere and the oceans, as well as a computer that is capable of carrying out long-term calculations.

## 8.6 Radiation in Global Climate Models

### 8.6.1 An Introduction to General Circulation Modeling

Radiative processes directly influence the dynamics and thermodynamics of the atmosphere through the generation of radiative heating/cooling rates, as well as through net radiative fluxes available at the surface. In Fig. 8.2 we showed the radiation balance at the top of the atmosphere in terms of the zonally averaged patterns for the absorbed solar and emitted infrared fluxes observed from satellites. As illustrated in Fig. 8.2, there is a gain of radiative energy between  $40^\circ\text{N}$  and  $40^\circ\text{S}$ , whereas there are losses in the polar regions. This pattern is largely caused by the sharp decrease in insolation during the winter season and the high surface albedo in the polar regions. In addition, we note that the outgoing infrared flux is only slightly latitudinally dependent, owing to the larger amount of atmospheric water vapor and the higher and colder clouds in the tropics.

This pattern of radiative energy excess and deficit generates the equator-to-pole temperature gradient and, subsequently, produces a growing store of zonal mean available potential energy. In the equatorial region, warm air expands upward and creates a poleward pressure gradient force at the upper altitudes, where air flows poleward from the equator. In the upper levels, air cools and sinks in the subtropical high-pressure belts located at about  $30^\circ$  and returns to the equator at the surface. Kinetic energy is generated as a result of the work done by the horizontal pressure gradient force. This thermally driven circulation between the equator and subtropics is referred to as the *Hadley cell*. As a result of the earth's rotation, air flowing toward the equator at the surface is deflected to the west and creates easterly trade winds. In the upper level of the Hadley cell, the Coriolis deflection of poleward-moving air generates westerly winds.

Similar thermally driven circulation is found in the polar regions. Cold air shrinks downward, producing an equator-directed pressure gradient force and motion in the lower altitudes. The sinking motion over the poles results in airflow in the upper level toward the pole and into the low-pressure belts located at about  $60^\circ$ . Thus, a Hadley circulation develops between the poles and the subpolar low-pressure regions. Here, the effect of the Coriolis force is the same; easterly winds are produced at the surface, while westerly winds are generated aloft. In the Hadley circulation, the atmosphere may be regarded as an engine that absorbs net heat from a high-temperature reservoir and releases this heat to a low-temperature reservoir. The temperature differences generate the available potential energy, which in turn is partly converted to kinetic energy to overcome the effect of friction.

Poleward zonal thermal winds at the upper altitudes become unstable in the middle latitudes, an effect referred to as *baroclinic instability* (Charney, 1947). A reverse circulation is generated in which warm air sinks in the subtropical highs and cold air rises in the subpolar lows in such a manner that westerly winds prevail at all levels. The meridional circulation in this region cannot be explained by the direct heating and cooling effects, as in the Hadley circulation, and cannot generate kinetic energy. The maintenance of westerlies in the middle latitudes is explained by the continuous transfer of angular momentum from the tropics, influenced by large-scale wave disturbances. The baroclinic waves transport heat poleward and intensify until heat transport is balanced by the radiation deficit in the polar regions.

The general circulation of the atmosphere described above is governed by a set of physical and mathematical equations defining the horizontal velocity fields, the first law of thermodynamics, the requirement of air-flow continuity, the large-scale hydrostatic balance, and the thermodynamic state. This system of equations consists of six unknowns: the two horizontal velocity components, the large-scale vertical velocity, density, pressure, and temperature. Additional equations can be introduced to include moisture variation based on the conservation of water vapor, and liquid and ice water content. This system of equations constitutes the so-called *general circulation model* (GCM).

To describe a GCM, representation in the vertical direction must be introduced. There are several alternative ways of treating the vertical coordinate in numerical

models. Because of the hydrostatic nature of large-scale motion, the height coordinate can be converted to the pressure coordinate to simplify the continuity equation and the density variation that occurs in other equations. However, the pressure coordinate encounters difficulties over a mountain, since a particular constant-pressure surface may intersect this mountain at certain times but not others. For this reason, the  $\sigma$ -coordinate system, introduced by Phillips (1957), has been used to remove the difficulty in the representation of lower-boundary conditions. The term  $\sigma = p/p_s$ , where  $p_s$  is the surface pressure;  $\sigma = 0$  when  $p = 0$ ; and  $\sigma = 1$  when  $p = p_s$ . The surface pressure in the  $\sigma$ -coordinate follows the terrain height at a given point in time and hence becomes a variable. While the  $\sigma$ -coordinate removes the problem in the representation of the lower-boundary conditions, it generates another problem in the computation of the pressure gradient force term, which is a small quantity but splits into two terms with large values. Numerical methods have been developed to circumvent this problem by interpolating between  $\sigma$  and  $p$  coordinates. Since the observed data are normally available in the  $p$ -coordinate, numerical interpolations are also required for the data corresponding to the initial field. For verification purposes, transformation of the predicted variables in the  $\sigma$ -coordinate from the model to the  $p$ -coordinate is required.

Appropriate numerical methods and initial conditions are required to solve the velocity components, temperature, humidity variables, and a term referred to as the *geopotential height*, the product of the height and gravitational acceleration, as functions of time and space, defined in spherical coordinates, based on a set of nonlinear partial differential equations. The evolution of the atmospheric flow patterns may be determined by integrating the prediction equations beginning at some initial time. Because of the nature of the nonlinearity in these partial and ordinary differential equations, analytic solutions are not practical, and numerical methods for their solution must be used. In the design of numerical methods, appropriate time and spatial differencing schemes are required to ensure computational stability. In the finite-difference approach, any dependent variable is approximated in terms of its values at discrete points in space and time (Arakawa, 1966). An alternative approach is the spectral method, which represents the flow field in space as a finite series of smooth and orthogonal functions. The prediction equations are then expressed in terms of the expansion coefficients, which are dependent on time.

An initial condition consisting of three-dimensional distributions of dependent variables is required to perform the numerical integration of a prediction model. Initial conditions for weather prediction are based on global observations at a specific time from which interpolations of the atmospheric variables are performed to model grid points by means of the objective analysis. Because of the initial imbalance of pressure and wind fields due to the presence of gravity waves, the initial data must be adjusted by numerical methods in order to eliminate meteorological noise. The prediction of large-scale geopotential height fields for a time period of about 5 days is largely influenced by the initial conditions and the data initialization procedure. Observational uncertainty in the initial state grows during model prediction because of the random turbulent nature of atmospheric motion. There is an inherent time limit

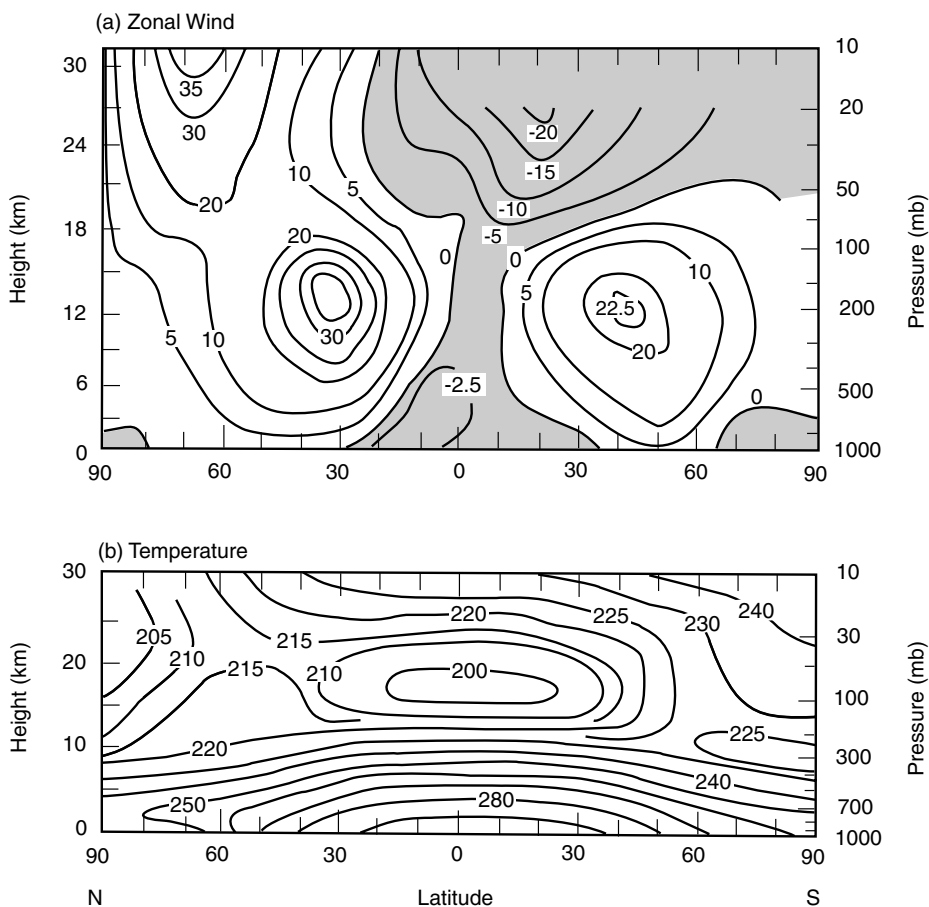


**Figure 8.22** Observed (a) zonal mean wind ( $\text{m s}^{-1}$ ) and (b) temperature (K) in height (pressure)–latitude cross section for December, January, and February. Negative regions of winds are shaded (data taken from Newell *et al.*, 1974).

of about a few weeks for predictability of the atmospheric state by means of a numerical integration of atmospheric models (Lorenz, 1969). This predictability limit is associated with the limited ability of atmospheric models to predict the day-to-day evolution of the atmosphere in a deterministic sense. It is feasible, however, for models to predict the statistical properties of the atmosphere. Models may be “tuned” to the mean or equilibrium state of the atmosphere, that is, the present climate, in terms of general circulation, temperature, radiative balance, cloud, and other pertinent patterns, and are referred to as *climate models*. Figure 8.22 displays the zonal mean wind and temperature for climatological winter conditions. Climatological radiation budgets were presented in Section 8.2.2, while cloud-cover climatology was illustrated in Fig. 7.21.

Through the process of tuning the model, all the relevant coefficients and/or computational schemes are adjusted to present climate conditions. When climate is perturbed by external forcings, such as the increase of greenhouse gases, model coefficients (e.g., drag coefficient) and computation schemes (e.g., cloud-cover formation) may no longer be representative of the perturbed climate. Thus, it is critically important to understand the physical processes involved in the model and to incorporate physical feedbacks into the model.

The oceans cover about 70% of the earth's surface. Through their fluid motion and high heat capacity, as well as their ecosystems, the oceans play an essential role in shaping the earth's climate and its variability. Wind stress at the ocean surface drives the large-scale circulation in the upper levels of the oceans. Evaporation from the ocean surface provides the water vapor needed for cloud formation and the resulting latent heat release. Ocean circulation redistributes heat and fresh water around the globe. The oceans store heat and absorb solar visible radiation at the surface, contributing substantially to the variability of climate on many time scales. The ocean thermohaline circulation also allows water from the surface to be carried into the deep ocean and may sequester heat away from the atmosphere for periods of thousands of years. The oceans absorb  $\text{CO}_2$  and other trace gases as well as aerosol particles and exchange them with the atmosphere, thereby altering ocean circulation and climate variability. It is clear that the modeling of climate and climate change must include an adequate description of oceanic processes and the coupling between the oceans and the atmosphere.

Figure 8.23 presents a schematic description of the principal components of the physical and mathematical definitions and feedbacks of a GCM for climate studies, including the contribution from the oceans, with reference to the transfer of solar and IR radiation in the atmosphere and their exchange with the earth's surface. In the following, we present the relative significance of radiative processes in global climate models, particularly those concerning the roles of clouds and aerosols.

### 8.6.2 Cloud Radiative Forcing in Global Climate Models

In Sections 8.2.3 and 8.4.5, we pointed out the importance of clouds in climate from the perspective of the radiation budget of the earth-atmosphere system as well as their role in greenhouse warming perturbations. The estimates of warming due to doubled  $\text{CO}_2$  produced by a number of numerical simulations of GCMs have shown surface temperature increases from about 1.3 to 5.4 K. Much of the difference in results has been attributed to the representation of clouds in the models. Early GCMs that were used for predicting climate change included fixed cloud covers estimated from climatology. Variations in clouds that may be forced by a climate perturbation and any feedback due to these cloud variabilities cannot be simulated in a fixed cloud experiment. Moreover, the variability of the stimulated present climate condition and the effect of the diurnal cycle may also be affected in this type of experiment. Interactive cloud parameterizations developed for climate models involve the direct use of relative humidity for the formation of cloud cover and the incorporation of a prognostic cloud water variable. The latter scheme allows the interaction and feedback

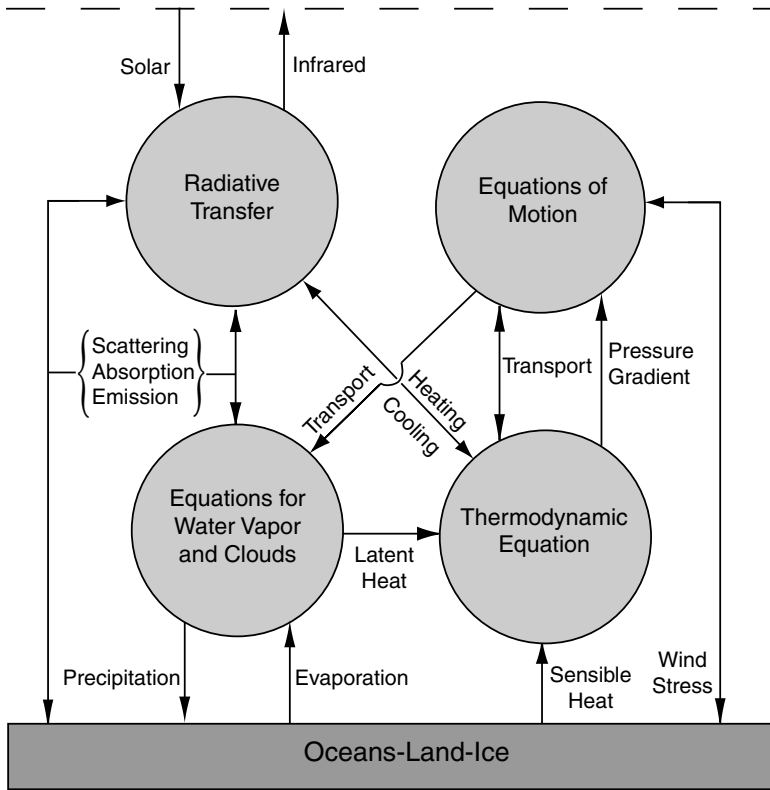


**Figure 8.23** Principal components of the physical and mathematical definitions and interactions of a general circulation model (GCM) for climate simulations, particularly in reference to radiative transfer in the earth-atmosphere system. See also Fig. 8.17.

of the radiative properties of clouds to be made dependent on the predicted cloud water path, a more physically based approach to understanding the role of clouds and radiation in climate and climate change. In the following, we present representative cloud simulations in GCMs with a particular emphasis on cloud radiative forcing.

#### 8.6.2.1 INTERNAL RADIATIVE FORCING

Clouds are produced by upward motion and the hydrological cycle and are highly interactive with the dynamic system. Atmospheric and surface temperatures as well as humidity are affected by the presence of clouds. As illustrated in Section 8.2.3, cloud radiative forcing information has been extracted from ERB data. The degree of cloud radiative forcing is determined by internal interactions and feedbacks and represents a measure of the instantaneous impact of clouds on radiative fluxes and heating rates. Thus, cloud radiative forcing is a useful diagnostic parameter for climate models.

The cloud radiative forcing discussed previously is in reference to the radiative fluxes at TOA. It is important, however, to recognize that, in principle, there are an

infinite number of cloud profiles in the atmosphere that can give a consistent ERB, and that the general circulation of the atmosphere is not directly related to the ERB but to radiative heating within the atmosphere. A realistic definition and understanding of cloud radiative forcing must begin with a consideration of radiative heating fields. Analogous to the definitions of ERB cloud radiative forcing, cloud radiative forcing with respect to internal solar and IR radiative heating can be defined as follows:

$$\dot{C}_{s,ir} = \left( \frac{\partial T}{\partial t} \right)_{s,ir} - \left( \frac{\partial T}{\partial t} \right)_{s,ir}^{cl}. \quad (8.6.1)$$

The presence of clouds produces strong IR cooling at cloud tops and significant heating at cloud bases, while the intensity of these cooling/heating configurations is dependent on the position and optical depth of the clouds (Section 4.7).

Internal cloud radiative forcing can be best understood from a zonally averaged profile. Figure 8.24 shows the latitudinal distribution of zonal mean cloud radiative forcing computed from the difference between atmospheric (including clouds) and clear-sky heating rates for a perpetual January simulation based on a climate model (Randall *et al.*, 1989). Zonally averaged solar radiative forcing is rather small: a  $0.4 \text{ K day}^{-1}$  warming in the upper tropical troposphere and weak negative values at low levels in the tropics and the Northern Hemisphere, in association with a reduction of gaseous absorption in the shadows of upper-level clouds. On the other hand, IR radiative forcing shows pronounced features, including a strong cooling associated with low-level cloud tops in the midlatitudes, a maximum warming of about  $2 \text{ K day}^{-1}$  at the 7 km level in the tropics, and a maximum cooling aloft of about  $1 \text{ K day}^{-1}$  at 16 km. The latter two features constitute a radiative dipole pattern that signifies the existence of optically thick convective anvil clouds. Anvils destabilize the upper troposphere because of cloud-top cooling, while warming in the middle troposphere tends to suppress shallow convection. The cloud-induced radiative destabilization of deep convection suggests that cloud IR radiative forcing has a positive feedback to the processes that generate high clouds. Owing to the domination of IR radiative cooling, the pattern of cloud net radiative forcing resembles that of the IR component.

#### 8.6.2.2 GREENHOUSE WARMING AND CLOUD COVER FEEDBACK

Global cloud cover has been routinely mapped from satellite visible and IR radiometers. In particular, the ISCCP program has produced useful cloud climatology for climate studies (Section 7.4.5). No discernible changes in global cloud cover have been reported during the past 20 years. Cloud cover can exert a large influence on climate, as shown by the results of one-dimensional radiative–convective models. The presence of clouds reduces the solar flux available to the earth and the atmosphere for absorption, known as the solar albedo effect, but at the same time it enhances the trapping of the outgoing IR fluxes, the greenhouse effect. Cloud-cover sensitivity experiments using global climate models have been performed by numerous researchers to understand the impact of clouds on the greenhouse warming produced by the increase of carbon dioxide. As an example, we show cloud-cover feedback processes in a climate model based on comprehensive numerical experiments carried out by



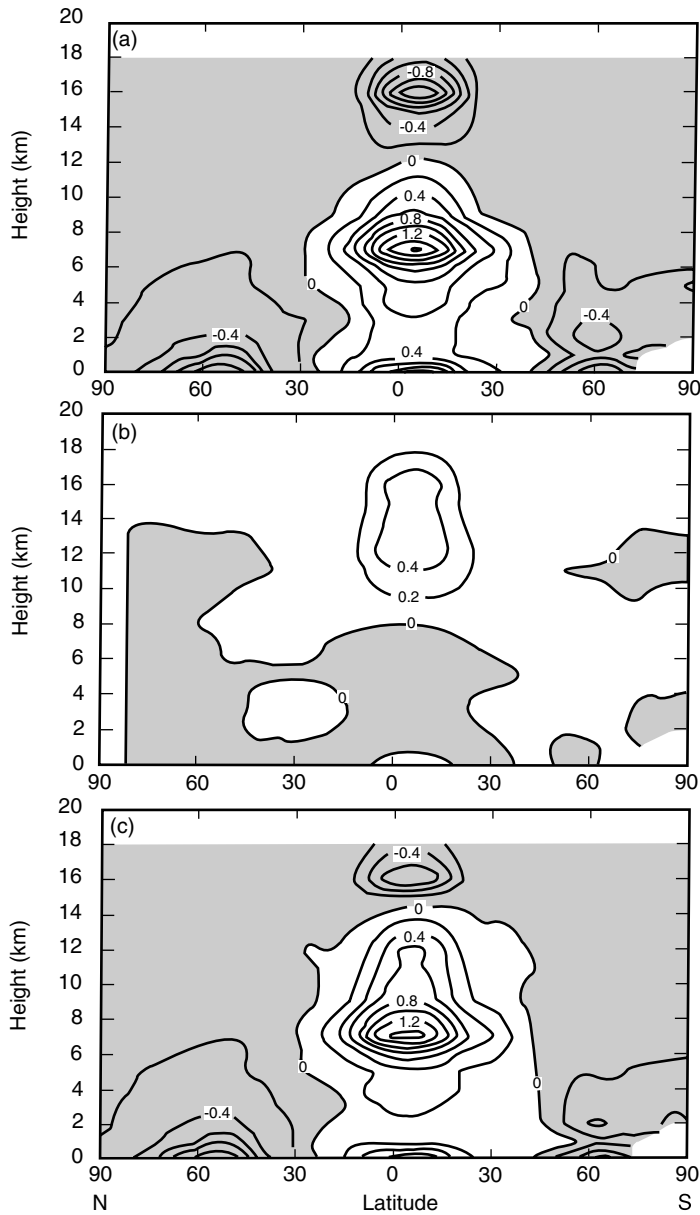


**Figure 8.24** Latitudinal distribution of the zonal mean cross section for (a) cloud longwave (IR) radiative forcing; (b) cloud shortwave (solar) radiative forcing; and (c) cloud net radiative forcing. The results are obtained from the perpetual January control simulation; the contour interval is  $0.2 \text{ K day}^{-1}$  (data taken from Randall *et al.*, 1989).

Wetherald and Manabe (1988). In order to facilitate the interpretation and analysis of the results from numerical experiments, a simple scheme for the computation of cloud cover was used in these experiments. At each grid point, clouds were placed in the layer where the relative humidity exceeded 99%; otherwise, no clouds were predicted. This simple scheme gives a global integral of total cloud amount approximately equal to 50%. Clouds may occur in a single (thin) layer or in multiple contiguous vertical layers (thick). The radiative properties of these clouds were prescribed. Two experiments were carried out: one prescribed the cloud cover, while the other predicted the distribution of cloud cover. The latter experiment incorporated the interaction between cloud cover and radiative transfer in the atmosphere in a simple way.

In response to the increase in  $\text{CO}_2$  concentration, cloud cover increases around the tropopause but decreases in the upper troposphere as shown in Fig. 8.25. The increase of high-level clouds reduces the outgoing IR flux from the top of the model atmosphere. At most latitudes a substantial reduction in cloud cover in the upper troposphere increases the available solar flux in the lower atmosphere and hence reduces the solar albedo effect. The change in the distribution of high clouds also increases the heating associated with the absorption of solar flux. The latitudinal profiles of the cloud-induced changes in the outgoing IR fluxes show a positive feedback to the increase in  $\text{CO}_2$  concentration. The increase in the net incoming solar flux coupled with the reduction of the outgoing IR flux, due to the change in cloud cover, leads to a significant positive feedback to greenhouse warming.

The cloud-cover feedback associated with radiative forcing depends on the performance of a model with respect to the formation of clouds, which, in turn, is a function of such factors as the vertical layer, numerical method, parameterization of moist convection and cloud formation, and the radiative properties of clouds. A cloud-cover feedback study can, therefore, be viewed as a study of the possible mechanisms involved in a model setting rather than a quantitative assessment of the influence of cloud cover on the sensitivity of climate. To reduce a large amount of the uncertainty in the estimate of climate sensitivity, improvements must be made in the treatment of cloud feedback processes in climate models. A model must be capable of reproducing the horizontal distributions of cloud cover and radiative fluxes that have been derived from satellite observations, such as the results from ISCCP and ERB. Moreover, as demonstrated from one-dimensional climate models, cloud LWC and mean effective particle size, two parameters that are dependent on temperature and other relevant variables, have significant feedbacks to greenhouse perturbations, a subject of discussion in the following subsection.

#### 8.6.2.3 GREENHOUSE WARMING AND CLOUD LIQUID/ICE WATER CONTENT FEEDBACK

Effects of the representation of clouds determined from different parameterization schemes on climate and climate perturbations have been investigated by Senior and Mitchell (1993), utilizing a low-resolution version of a GCM. This model included a prognostic cloud water variable and incorporated interactive cloud optical properties. The model also incorporated parameterization approaches for the production of

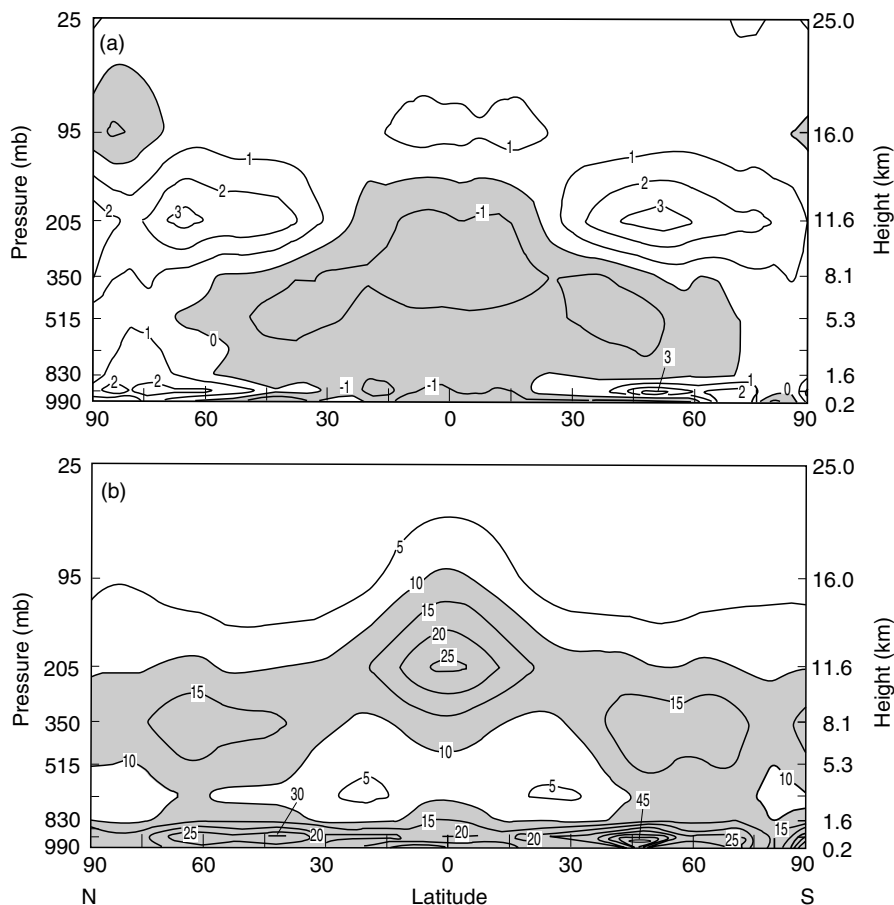


**Figure 8.25** Height-latitude cross section for (a) CO<sub>2</sub>-induced change of zonal mean cloud amount (%); and (b) zonal mean cloud amount (%) obtained from a GCM experiment (data taken from Wetherald and Manabe, 1988).

precipitation from water and ice clouds in which the empirical coefficients in the parameterization equations were taken from microphysics measurements (Heymsfield and Donner, 1990). In addition, cloud radiative properties as a function of liquid/ice water path were expressed in terms of reflectivity, transmissivity, and absorptivity using the values presented by Liou and Wittman (1979). Effects of cloud particle size, which was not a prognostic variable in the model, on the cloud radiative properties were not accounted for, however.

The sensitivity of cloud representations in the model to a doubling of atmospheric CO<sub>2</sub> was investigated over perpetual summer (June, July, August) and winter (December, January, February) conditions for a 10-year period after reaching equilibrium. Figure 8.26 shows the height-latitude cross section of equilibrium changes

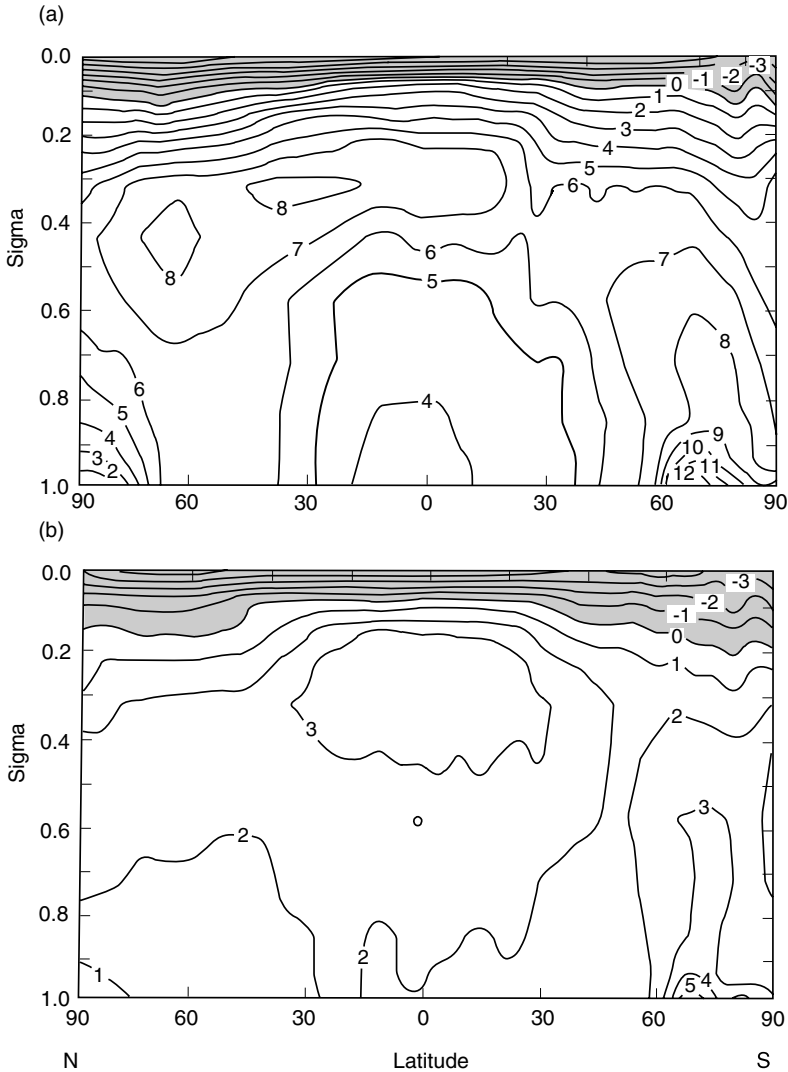


**Figure 8.26** Height ( $\sigma$ -coordinate)–latitude cross section of equilibrium temperature changes in a 10-year summer simulation of doubling CO<sub>2</sub>. Contours in every 1 K and reductions are shaded. (a) Cloud parametrization using an RH method; and (b) an interactive cloud water prognostic equation and radiative transfer feedback (data taken from Senior and Mitchell, 1993).

of temperature based on two cloud formation schemes. One employed the prognostic cloud formation coupled with the interactive radiative properties described above. The other used the relative humidity (RH) scheme in which the fractional amount of layer clouds is predicted from a quadratic dependence on RH. Cloud amount increased from zero at an assigned threshold level to full cover at saturation. Similar to the

experiment performed by Wetherald and Manabe (1988) described in the preceding subsection, the global mean total cloud cover was around 50%, while the radiative properties of high, middle, and low clouds determined from the RH scheme were fixed. The two experiments produced a large warming in the upper tropical troposphere, an amplification of the surface warming in high latitudes in winter, and a substantial stratospheric cooling of up to 5°C, in agreement with most model simulations incorporating enhanced CO<sub>2</sub>. However, the prognostic cloud formation model with interactive cloud optical properties differed from the RH scheme in both the magnitude and distribution of the warming. The maximum warming of the upper troposphere was reduced from 8 K in the RH model to 3 K in the interactive cloud formation scheme. There was also a large reduction in the lower-level midlatitude warming from over 6 K to 2 K between the two cloud schemes. The pattern was similar in the summer simulation. The global mean annual change in surface temperature was reduced from 5.4 K in the RH model to 1.9 K in the interactive cloud formation scheme. When the interactive cloud formation was included, the resultant reduction in warming was due to a negative feedback produced from the change in cloud thermodynamic phase from ice to water and the associated prevalence of the solar albedo effect.

#### 8.6.2.4 CLOUD PARTICLE SIZE FEEDBACK

Studies of the effects of possible changes in cloud particle size associated with air pollution and/or global warming using global climate models are still at an embryonic stage. In Eq. (8.4.7), we showed that cloud particle size directly affects cloud optical depth and hence, cloud albedo. Modeling of the formation of water-droplet and ice-crystal size spectra and the associated precipitation process based on physical principles is an involved and intricate computational task, considered to be a luxury for global climate models under present computer power limitations. However, parameterization approaches have been used to incorporate cloud particle size in climate models based on an assumed aerosol size distribution and large-scale variables. Uncertainty in the radiative forcing produced by the aerosol-cloud indirect effect estimated from climate models is so large that the confidence level in these estimates has been noted to be extremely low (IPCC, 1996; Hansen *et al.*, 2000). Reduction of this uncertainty requires a long-term global observational program for simultaneous measurements of aerosol and cloud particle sizes, coupled with independent validation.

### 8.6.3 Direct Radiative Forcing: Aerosols and Contrails

The subject of cloud radiative forcing is concerned with the effects of clouds on the radiation field of the earth-atmosphere system indirectly induced by external forcings such as the increase in anthropogenic greenhouse gases and/or particulates, which has been referred to as the indirect effect. However, two particle types of anthropogenic origin can directly exert a radiative forcing effect in climate systems through their scattering and absorption processes: aerosols generated in the planetary boundary layer and contrails produced in the upper troposphere and lower stratosphere.

### 8.6.3.1 AEROSOLS

In Section 8.4.4, we discussed the interaction of aerosols with solar radiation and pointed out that the radiative forcing produced by anthropogenic tropospheric aerosols has been recognized as a significant contributor to climate change. Two types of aerosols have been identified to be of specific importance in climate studies: sulfate and carbonaceous aerosols. The latter aerosols result from biomass burning as well as from fossil fuel production.

A number of GCM experiments have been conducted to investigate the impact of sulfate and carbonaceous aerosols on climate radiative forcing. For this purpose, a GCM must be coupled with an atmospheric chemical transport model, which is used to compute aerosol concentration in a separate manner. The computation of aerosol concentration for radiative transfer requires its inventory from available observations as an initial condition, including the estimation of carbonaceous aerosols produced from biomass burning, black and organic carbons generated from fossil fuel emissions, and sulfur emission. The radiative properties of aerosols are a function of their size distribution and refractive index, which is determined by their chemical composition. The chemical state and size of an aerosol are also dependent on RH. To model the RH dependence, the fundamental Köhler equation associated with diffusion growth can be used, but a size distribution must be assumed.

In the following, we present a GCM experiment conducted by Penner *et al.* (1998) to illustrate the relative significance of various aerosol types in the context of climate radiative forcing. In the experiment, these authors assumed that sulfate was present as  $(\text{NH}_4)_2\text{SO}_4$  in sulfate aerosols, that smoke particles were made up of a variety of water-soluble salts and other elements, that biomass aerosols behaved similarly to an aerosol having 30% of  $(\text{NH}_4)_2\text{SO}_4$  by mass, and that black and organic carbon particles were hydrophobic. Having determined the size distribution and chemical composition as a function of RH, single-scattering and absorption calculations for the aforementioned aerosol types assumed to be spherical in shape can then be carried out by using the Lorenz–Mie theory detailed in Section 5.2. A chemical transport model was employed to calculate aerosol concentrations every 6 hours. The results were then incorporated into the GCM to compute the radiative forcings at both TOA and the surface, defined as the difference between the net solar flux with and without the contributions by anthropogenic aerosols. In the course of model integration, the cloud distribution remained unchanged in both experiments, implying that the indirect forcing via cloud formation was not accounted for.

Figure 8.27 illustrates the global annual average radiative forcing at TOA for various aerosol types determined from the coupled GCM and chemical transport model. For the aerosols produced from biomass burning, two negative forcing values are presented because of the assumed size distributions. Negative forcing implies that more solar flux is reflected back to space, thereby reducing the absorption by aerosols in the earth–atmosphere system. The computed annual average forcings produced by fossil fuel black carbon (BC) alone and a combination of fossil/urban BC and organic carbon (OC) are  $0.2$  and  $0.16 \text{ W m}^{-2}$ , respectively. These forcings are primarily associated with emissions in North America, Europe, and Asia. The positive forcings

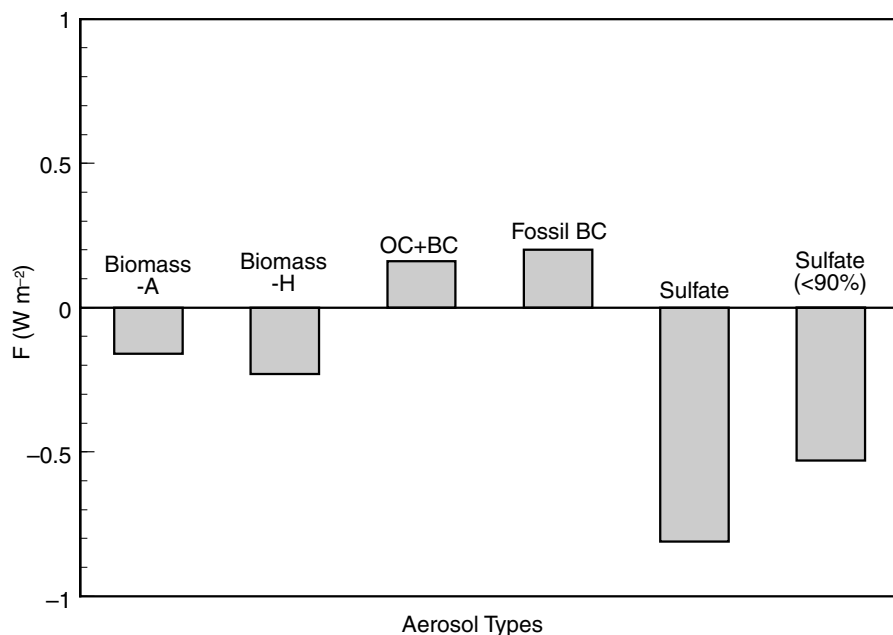


**Figure 8.27** Global average radiative forcing at TOA for various aerosol types estimated from a GCM coupled with a chemical transport model. Biomass-A and -H denote the use of different assumed size distributions, OC denotes organic carbon, BC denotes black carbon, and sulfate (<90%) represents the case where the particle size and optical properties remain fixed at  $\text{RH} = 90\%$  if  $\text{RH} > 90\%$  (data taken from Penner *et al.*, 1998).

are produced by the domination of absorption due to BC. In the case of sulfate, a larger negative forcing of  $-0.81 \text{ W m}^{-2}$  is shown because of the negligible absorption of  $(\text{NH}_4)_2\text{SO}_4$  and water in the solar spectrum. When the RH dependence was capped at 90%, the forcing decreased by 50% because of the aerosol size effect.

On the basis of the preceding discussion, it is clear that direct climate forcing by anthropogenic aerosols in the troposphere is subject to a large degree of uncertainty in view of the numerous assumptions involved in the calculation of the spectral single-scattering and absorption properties of various aerosol types, as well as the treatment of aerosol transport, which is regional in character. At present, we do not know the precise sign of the current trend of aerosol forcing because such information would require knowledge of the trends of different aerosol compositions. Direct aerosol forcing largely depends on the aerosol's single-scattering albedo, and hence, on the amount of absorbing constituents. Indirect aerosol forcing depends on the effectiveness of aerosols in forming cloud particles and the consequence of cloud and precipitation processes, a subject of great complexity and uncertainty. In summary, climate forcing by anthropogenic aerosols may present the largest source of uncertainty about future climate change, the solution of which must rely on accurate long-term global observations of aerosol size and composition with appropriate validation.

### 8.6.3.2 CONTRAILS

The upper level ice crystal clouds produced by jet aircraft are known as contrails, or condensation trails as noted by Appleman (1953). Contrails are visible line clouds resulting from water vapor emissions that form behind aircraft flying in sufficiently cold air. It has been suggested that water droplets can form on the soot and sulfuric acid particles emitted from aircraft and/or background particles, and can then freeze to become ice particles. Persistent contrails often develop into more extensive contrail cirrus, particularly in ice-supersaturated air masses, in which the ice supersaturation is generally too small to allow cirrus clouds to form naturally. Contrails may enhance the extension of the natural cirrus cover in adjacent areas where RH is too low for the spontaneous nucleation of ice crystals, an indirect effect that has not been quantified at this point. Contrails can affect the atmospheric moisture budget by scavenging large cloud particles from the upper troposphere and by seeding clouds at lower altitudes.

In an analysis of cirrus cloud cover in Salt Lake City based on surface observations, Liou *et al.* (1990c) found that a substantial increase in cirrus clouds occurred in about 1965, coinciding with a sharp increase in domestic jet fuel consumption in the mid-1960s. Increased cirrus cloudiness has also been detected in climate data from stations in the midwestern and northwestern United States that are located beneath the major upper-tropospheric flight paths. A comprehensive analysis of jet aircraft contrails over the United States and Europe using satellite infrared imagery has been carried out (see, e.g., Minnis *et al.*, 1998; IPCC, 1999). Figure 8.28 displays a high-resolution IR image from NOAA 14, showing a variety of contrails in forms of spreading, diffusion, and thinning, associated with patchy cirrus.

The growing concern over the impact of increasing jet aircraft activities on the environment and climate led the Intergovernmental Panel on Climate Change to produce a report on the subject of aviation and global atmosphere (IPCC, 1999). Discussions of the issues related to contrails, cirrus clouds, and climate radiative forcing are detailed in Chapter 3 of the report. It has been estimated that aircraft line-shaped contrails cover about 0.1% of the earth's surface on an annually averaged basis, but with much higher values in local regions. Projections of contrail cover have also been made based on the rate of growth in aviation fuel consumption.

Radiative forcing of contrails depends not only on their cover, but also on their ice-crystal size distribution and shape. The ice-crystal images collected by the optical probe and replicator system from aircraft platforms during a number of field experiments show that contrails predominantly consist of bullet rosettes, columns, and plates with sizes ranging from about 1  $\mu\text{m}$  to about 100  $\mu\text{m}$ . The solar albedo and thermal emission of contrails computed from radiative transfer models reveal their significant dependence on both mean effective ice-crystal size and shape. Despite a large degree of uncertainty regarding the cover and ice-crystal size and shape of contrails, estimations of their globally and annually averaged radiative forcing have been made (IPCC, 1999). For subsonic aircraft emissions in 1992, a positive radiative forcing of  $0.02 \text{ W m}^{-2}$  with an uncertainty of more than a factor of 2 was estimated. It is much smaller than those produced by tropospheric aerosols. Nevertheless, the future projection of air traffic shows that the direct climatic effects of contrails could



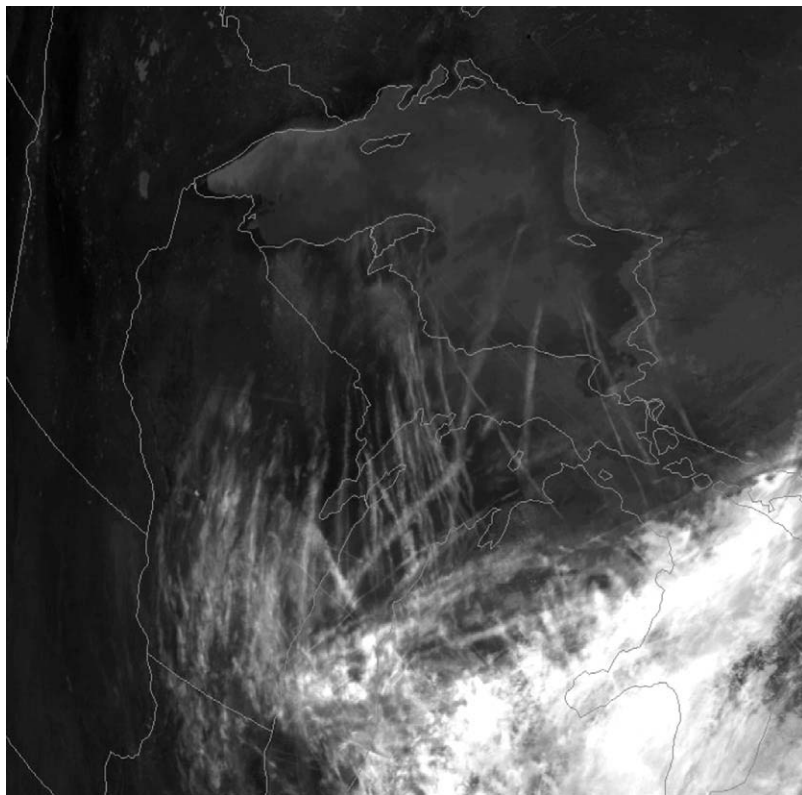


**Figure 8.28** High-resolution thermal infrared image over the Great Lakes area of the United States from the NOAA-14 satellite at 2050 UTC October 2000, showing a number of north–south oriented contrails associated with patchy cirrus (courtesy of Patrick Minnis of the NASA Langley Research Center).

be on the same order as some tropospheric aerosol types. Moreover, it is noted that contrails have a significant regional character.

Perhaps the most significant contrail impact on climate is through their indirect effect on cirrus cloud formation. To reduce substantial uncertainties in contrail-cirrus radiative forcing estimations, a long-term observation program is needed to separate the cirrus clouds that are generated through contrails and other substances emitted from aircraft from those that occur naturally. The radiative and climatic impact of cirrus clouds have been articulated in a number of review articles (Liou, 1986; Sassen, 1997; and IPCC, 1999). The subject of the remote sensing of cirrus clouds from satellites was presented in Section 7.3.5.

#### 8.6.4 Radiation in El Niño–Southern Oscillation

The importance of clouds and their radiative properties in shaping climate and very long-term climate trends, such as those due to increasing greenhouse gases and

aerosols, has long been well known. However, their impact on interannual to decadal time-scale variability is not as generally recognized. In the following, we present an example of the impact of clouds and their radiative effects on a simulation of the El Niño–Southern Oscillation (ENSO) based on a global climate model coupling the atmosphere and the oceans developed at the University of California, Los Angeles (UCLA).

El Niño is a climatic feature associated with the interannual oceanic warming of the eastern tropical Pacific off the coasts of Peru and Ecuador. In 1982–83, El Niño was linked to the disastrous droughts on the continents of southeastern Asia and Australia, unusual weather patterns over North and South America, and the weakening of monsoons over India. The Southern Oscillation involves a seesaw effect in the surface pressure across the tropical Pacific Ocean. Bjerknes (1969) discovered that continual Southern Oscillation is both the cause and the consequence of continually changing sea surface temperature (SST) patterns and that El Niño, associated with warm SSTs of the eastern tropical Pacific, is but one phase of a cycle. Analogous to the seasonal cycle representing an oscillation between winter and summer, the Southern Oscillation is a fluctuation between El Niño and a complementary state referred to as La Niña. While the seasonal cycle is forced by the variability of solar insolation associated with the earth's obliquity, the Southern Oscillation corresponds to a natural mode of interannual oscillation of the coupled ocean and atmosphere between the El Niño and La Niña states associated with SST anomalies. It is clear that the successful simulation and prediction of ENSO requires a global climate model that incorporates dynamic and physical couplings of the atmosphere and the oceans.

The UCLA coupled atmosphere–ocean general circulation model that was used to study the effect of clouds and their radiative properties on SST simulations consisted of an atmospheric GCM (AGCM) and an oceanic GCM (OGCM) that were coupled in the following way. The surface wind stress and heat flux were calculated hourly by the AGCM and its daily averages were transferred to the OGCM. At the same time, the SST was calculated hourly by the OGCM and its value at the time of coupling was passed to the AGCM. The AGCM had a horizontal resolution of  $4^\circ$  latitude by  $5^\circ$  longitude and 15 layers in the vertical. The OGCM domain was from  $30^\circ\text{S}$  to  $50^\circ\text{N}$  and from  $130^\circ\text{E}$  to  $70^\circ\text{W}$  with 27 vertical layers, had a constant depth at 4150 m, and covered a longitudinal resolution of  $1^\circ$  with varying latitudinal resolution. Figure 8.29a displays the climatological SST patterns simulated by the UCLA coupled model with the incorporation of the formation of stratus clouds over the Peruvian coast areas and of a larger high cloud emissivity (Yu and Mechoso, 1999). The interannual SST variabilities in terms of the amplitude, frequency, and the associated atmospheric and oceanic structures closely resemble those of the observed ENSO episodes. However, without the inclusion of proper representations of stratus clouds and high-cloud emissivity, the simulated SSTs are much lower (Fig. 8.29b) than those displayed in Fig. 8.29a, and their variabilities are about four times weaker. The inclusion of appropriate high-cloud emissivity produces a warmer upper troposphere, leading to a reduction of the temperature gradient below high clouds and the subsequent reduction of cumulus activity and surface evaporation in the tropical Pacific region. The introduction of

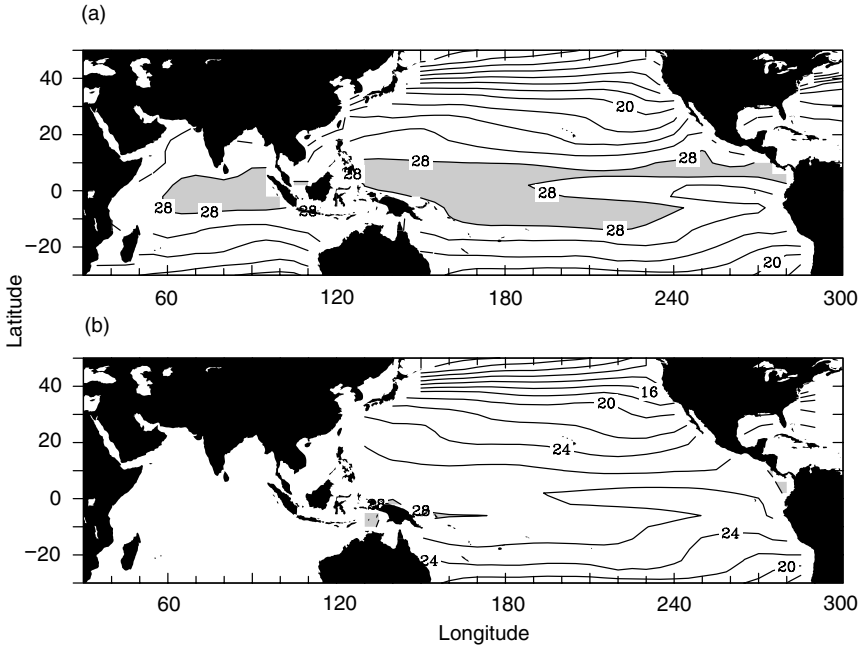


**Figure 8.29** Climatological SST ( $^{\circ}\text{C}$ ) patterns simulated by the UCLA coupled atmosphere–ocean general circulation model: (a) a version with a suitable incorporation of high-cloud emissivity and the formation of low-level Peruvian stratus clouds, and (b) an earlier version without a specific inclusion of these two cloud effects. The shaded area in (a) shows the SST higher than  $28^{\circ}\text{C}$  including the Indian ocean (data provided by Jin-Yi Yu of the University of California, Los Angeles).

the low-level Peruvian stratus clouds decreases the amount of solar flux reaching the surface and, hence, the surface temperature locally, allowing a better simulation of the SST pattern in the central equatorial Pacific.

In light of the foregoing discussion, it appears evident that the interaction and feedback of clouds and their radiative properties are important physical processes governing the interannual SST variability. Further numerical experiments employing internally consistent and physically based cloud formation and radiative transfer parameterizations are required to explore the issues concerning the role of cloud and radiation processes in the context of interannual and decadal time-scale variabilities, particularly when these variabilities are coupled with greenhouse warming.

## Exercises

8.1 Assume that the atmosphere acts as a single isothermal layer with a temperature  $T_a$  that transmits solar radiation but absorbs all thermal infrared radiation. Show that the global surface temperature  $T = (2T_a)^{1/4}$ . Let the global albedo be 30%, and the solar constant be  $1366 \text{ W m}^{-2}$ . What is the global surface temperature?

- 8.2 The mean global surface temperature is only about 15°C. The mean global absorptivity of solar radiation by the atmosphere is about 0.2. Use the global albedo and solar constant given in Exercise 8.1 and compute the mean global emissivity and temperature of the atmosphere. Repeat the calculation if the solar constant decreases by 1%.
- 8.3 Let the global reflectivities of the atmosphere and the surface be  $\bar{r}$  and  $r_s$ , respectively. Consider the multiple reflection between the surface and the atmosphere and show that the global albedo of the earth–atmosphere system is given by

$$\bar{r} + (1 - \bar{A} - \bar{r})^2 r_s / (1 - r_s \bar{r}).$$

- 8.4 In Eq. (8.4.5), express the IR flux based on the Stefan–Boltzmann law and use a constant emissivity for the earth–atmosphere system. What would be the sensitivity of surface temperature to this IR flux and why is this sensitivity much smaller than that presented in Eq. (8.4.6)?
- 8.5 (a) The normalized mean annual distribution of insolation is approximately given by Eq. (8.5.29), and the albedo is given by the step function

$$r(x, x_i) = \begin{cases} 0.62, & x > 0.95 \\ 0.32, & x < 0.95. \end{cases}$$

Compute and plot the latitudinal surface temperature as a function of  $x$  from Eq. (8.5.15b).

- (b) Also compute the temperature at the ice line assuming an albedo of 0.5. Show that the solution of the ice-line position  $x_i$  is quadratic. Plot  $x_i$  as a function of  $Q/Q_0$  from 0.97 to 1.2.
- 8.6 (a) Derive Eq. (8.5.19) by means of a linear perturbation analysis.
- (b) Show that the area covering the earth poleward of latitude  $\varphi$  is given by  $2\pi a_e^2(1 - x)$ , where  $a_e$  is the radius.
- (c) Let  $\Delta\bar{r} = 0.3s^*(x)\ell(x, \bar{x}_i)$ , where  $\ell$  is the ratio of the change in the ice-covered area to the total area of the Northern Hemisphere, and

$$s^*(x) = \int_{x_i}^{0.95} s(x) dx.$$

Show that the solution of  $x_i$  is given by a fourth-order polynomial equation. Compute and plot  $x_i$  as a function of  $\Delta Q/Q_0$ .

- 8.7 From Eq. (8.5.27a), we find

$$F_0 = QH_0(x_i), \quad F_2 = QH_2(x_i)/(6D'' + 1).$$

Based on the two-mode approximation, we also have from Eq. (8.5.25)

$$F(x) = F_0 + F_2 P_2(x).$$

By fitting the present climate conditions, i.e.,  $\bar{x}_i = 0.95$ ,  $4Q_0 = 1366 \text{ W m}^{-2}$ , find the empirical coefficient  $D''$ .

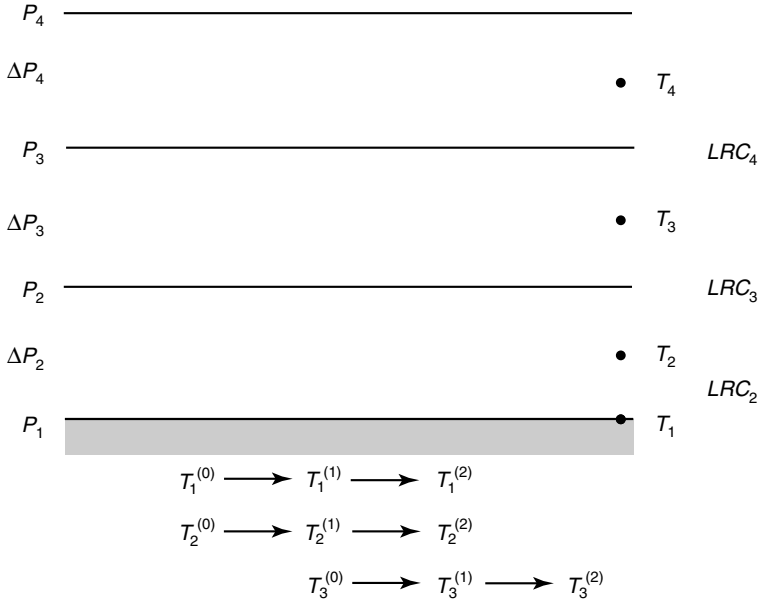


**Figure 8.30** Graphic representation of the temperature iteration in the convective adjustment scheme. The superscript ( $n$ ) ( $n = 0, 1, 2, \dots$ ) denotes the iterative step. The subscripts 1 and (2, 3, ...) denote the surface and atmospheric layers, respectively. The term  $LRC_k$  ( $k = 2, 3, \dots$ ) represents the critical temperature difference.

8.8 Based on Eqs. (8.3.19)–(8.3.21) and in reference to Fig. 8.30, we may construct an iterative procedure for the computation of a temperature profile by employing the following convective adjustment scheme:

- (a) First, compute  $T_k^{(0)}$ , the temperature for each atmospheric layer, for  $k = 2, 3, 4, \dots, N$  by using

$$T_k^{(0)} = T_k^\chi + \left( \frac{\partial T}{\partial t} \right)^\chi \Delta t, \quad (8.E.1)$$

where the superscript ( $n$ ) ( $n = 0, 1, 2, \dots$ ) denotes the iterative step during the  $\chi$ th time step, and  $T_k$  is the temperature at the  $k$ th layer. The subscript  $k = 1$  denotes the surface, and  $k = N$  is the top level. The meanings of superscript ( $n$ ) and subscript  $k$  are graphically displayed in Fig. 8.30.

- (b) Second, calculate the radiative equilibrium temperature for the surface ( $k = 1$ ) by using

$$T_1^{(0)} = \left( \frac{F_{s,1} + F_{ir,1}^\chi}{\sigma} \right)^{1/4}, \quad (8.E.2)$$

where  $F_{s,1}$  and  $F_{ir,1}^\chi$  are the net solar flux and downward longwave flux at the surface, respectively, and  $\sigma$  is the Stefan–Boltzmann constant. To a

good approximation, the net solar flux in the atmosphere may be computed independently of the temperature.

- (c) Third, compute the critical temperature difference for each layer as follows:

$$\text{LRC}_k = (z_k - z_{k-1})\gamma_c, \quad (8.E.3)$$

where  $z_k$  is the altitude of the  $k$ th level and  $\gamma_c$  is the critical lapse rate.

- (d) Fourth, calculate  $T_1^{(1)}$  and  $T_2^{(1)}$  such that they satisfy the energy balance:

$$\frac{C_p}{g} \Delta p_2 (T_2^{(1)} - T_2^{(0)}) = \sigma \Delta t [(T_1^{(0)})^4 - (T_1^{(1)})^4], \quad (8.E.4a)$$

$$T_2^{(1)} = T_1^{(1)} - \text{LRC}_2, \quad (8.E.4b)$$

where  $\Delta p_2 = p_1 - p_2$ . The term on the right-hand side of Eq. (8.E.4a) represents the net upward radiative flux. After eliminating  $T_1^{(1)}$  in Eqs. (8.E.4a) and (8.E.4b),  $T_2^{(1)}$  can be solved from the following equations employing an iterative procedure (e.g., Newton's method) as follows:

$$\sigma \Delta t (T_2^{(1)} + \text{LRC}_2)^4 + \frac{C_p}{g} \Delta p_2 T_2^{(1)} - \frac{C_p}{g} \Delta p_2 T_2^{(0)} - \sigma \Delta t (T_1^{(0)})^4 = 0. \quad (8.E.5)$$

- (e) Fifth, if  $T_2^{(1)} - T_3^{(0)} > \text{LRC}_3$ , that is, if the layer is unstable,  $T_1^{(2)}$ ,  $T_2^{(2)}$ , and  $T_3^{(1)}$  can be simultaneously computed so that they satisfy the following relationships:

$$\frac{C_p}{g} [\Delta p_2 (T_2^{(2)} - T_2^{(1)}) + \Delta p_3 (T_3^{(1)} - T_3^{(0)})] = \sigma \Delta t [(T_1^{(1)})^4 - (T_1^{(2)})^4], \quad (8.E.6a)$$

$$T_3^{(1)} = T_2^{(2)} - \text{LRC}_3, \quad (8.E.6b)$$

$$T_1^{(2)} = T_2^{(2)} + \text{LRC}_2, \quad (8.E.6c)$$

where  $\Delta p_3 = p_2 - p_3$ . These equations can also be solved by an iterative method. If  $T_2^{(1)} - T_3^{(0)} \leq \text{LRC}_3$ , the layer is stable. We can then determine  $T_2^{(2)}$  and  $T_3^{(1)}$  by setting

$$T_2^{(2)} = T_2^{(1)}, \quad T_3^{(1)} = T_3^{(0)}. \quad (8.E.7)$$

- (f) Sixth, for levels  $k = 3, 4, 5, \dots, N$ , it is necessary to find  $T_{k+1}^{(1)}$  and  $T_k^{(2)}$ . If  $T_k^{(1)} - T_{k+1}^{(0)} > \text{LRC}_{k+1}$ , we may use

$$\frac{C_p}{g} [\Delta p_{k+1} (T_{k+1}^{(1)} - T_{k+1}^{(0)}) + \Delta p_k (T_k^{(2)} - T_k^{(1)})] = 0, \quad (8.E.8a)$$

and

$$T_k^{(2)} - T_{k+1}^{(1)} = \text{LRC}_{k+1}, \quad k \geq 3. \quad (8.E.8b)$$

**Table 8.1**  
Radiative Heating Rate, Temperature, and Air Density Profiles

| Height (km) | Temperature (K) | Solar (K day <sup>-1</sup> ) | IR (K day <sup>-1</sup> ) | Air density (g m <sup>-3</sup> ) |
|-------------|-----------------|------------------------------|---------------------------|----------------------------------|
| 0.2         | 303.7           | 0.74                         | -2.07                     | $1.20 \times 10^3$               |
| 0.7         | 295.3           | 0.43                         | -1.10                     | $1.13 \times 10^3$               |
| 1.1         | 287.3           | 0.42                         | -0.77                     | $1.09 \times 10^3$               |
| 1.6         | 278.8           | 1.04                         | -3.09                     | $1.05 \times 10^3$               |
| 2.4         | 269.8           | 0.92                         | -2.29                     | $0.95 \times 10^3$               |
| 3.5         | 259.2           | 0.93                         | -1.95                     | $8.6 \times 10^2$                |
| 4.8         | 246.9           | 0.69                         | -1.52                     | $7.4 \times 10^2$                |
| 6.3         | 234.3           | 0.50                         | -1.41                     | $6.3 \times 10^2$                |
| 8.1         | 224.4           | 0.31                         | -0.89                     | $5.0 \times 10^2$                |
| 10.4        | 222.9           | 0.21                         | -0.01                     | $3.8 \times 10^2$                |
| 13.9        | 216.4           | 0.23                         | -0.30                     | $2.3 \times 10^2$                |
| 19.8        | 219.4           | 0.80                         | -0.85                     | $8.9 \times 10^1$                |
| 27.3        | 227.1           | 1.49                         | -1.29                     | $2.9 \times 10^1$                |
| 35.2        | 234.1           | 3.41                         | -4.52                     | $8.5 \times 10^0$                |
| 43.2        | 255.3           | 9.41                         | -10.15                    | $3.0 \times 10^0$                |
| 52.1        | 268.5           | 10.84                        | -7.89                     | $1.0 \times 10^0$                |
| 61.0        | 239.8           | 3.26                         | -4.62                     | $0.9 \times 10^0$                |

Substituting Eq. (8.E.8b) into Eq. (8.E.8a) and solving for  $T_k^{(2)}$  leads to

$$T_k^{(2)} = \frac{\Delta p_{k+1}(T_{k+1}^{(0)} + \text{LRC}_{k+1}) + \Delta p_k T_k^{(1)}}{\Delta p_k + \Delta p_{k+1}}. \quad (8.E.8c)$$

$T_{k+1}^{(1)}$  can then be solved by substituting  $T_k^{(2)}$  back into Eq. (8.E.8b). If  $T_k^{(1)} - T_{k+1}^{(0)} < \text{LRC}_{k+1}$ , we set

$$T_k^{(2)} = T_k^{(1)}, \quad T_{k+1}^{(1)} = T_{k+1}^{(0)}. \quad (8.E.9)$$

(g) Seventh, replace  $T_k^{(2)}$  by  $T_k^{(0)}$  for  $k = 1, 2, 3, \dots, N$ .

(h) Finally, repeat steps (d) through (g) until all layers of the supercritical lapse rate are eliminated.

Letting the critical lapse rate be  $6.5 \text{ K km}^{-1}$ , compute the temperature profile corresponding to the radiative heating profile listed in Table 8.1. In the calculations, let the net solar and IR fluxes at the surface be  $159.1$  and  $386.9 \text{ W m}^{-2}$ , respectively, and the surface air density be  $1.221 \times 10^3 \text{ g m}^{-3}$ .

### Suggested Reading

Budyko, M. I. (1982). *The Earth's Climate: Past and Future*. Academic Press, New York. Chapter 3 provides a discussion of the energy balance of the earth's surface and some results from energy balance models.

- Hartmann, D. L. (1994). *Global Physical Climatology*. Academic Press, New York. Chapters 10, 11, and 12 present concise discussions of climate models and natural and anthropogenic climate changes.
- IPCC (1996). *Climate Change 1995: The Science of Climate Change*. J. T. Houghton, L. G. Meira Filho, B. A. Callander, N. Harris, A. Kattenberg, and K. Maskell (eds.). Cambridge University Press, Cambridge, U.K. Chapter 2 gives a comprehensive discussion of radiative forcing due to various greenhouse gases and aerosols.
- Liou, K. N. (1992). *Radiation and Cloud Processes in the Atmosphere. Theory, Observation, and Modeling*. Oxford University Press, New York. Chapters 6 and 7 provide basic discussions of radiation budgets and climatic perturbations due to greenhouse gases, aerosols, and clouds.
- Peixóto, J. P., and Oort, A. H. (1992). *Physics of Climate*. American Institute of Physics, New York. Chapter 17 presents various types of climate models.
- Trenberth, K. E., ed. (1992). *Climate System Modeling*. Cambridge University Press, Cambridge, U.K. Chapters 1, 7, 10, and 20, authored by S. S. Schneider, R. D. Turco, J. T. Kiehl, and W. M. Washington, respectively, contain useful information pertaining to the role of radiation in climate and climate modeling.